UNIVERSITY OF NAPLES FEDERICO II

Department of Structure
for Engineering and Architecture

PH.D. PROGRAMME IN
MATERIALS ENGINEERING AND STRUCTURES
COORDINATOR PROF. GIUSEPPE MENSITIERI
XXVII CYCLE

ORSOLA COPPOLA

PH.D. THESIS

INNOVATIVE MATERIALS FOR SEISMIC PROTECTION OF NONSTRUCTURAL COMPONENTS

TUTORS: PROF. GENNARO MAGLIULO
PROF. ERNESTO DI MAIO

2015

A Michele,
perché la sua estrema fiducia nelle mie capacità
mi spinge a dare sempre il meglio,
cosicché possa non deluderlo mai.

Acknowledgements[1]

Quello dei ringraziamenti è sempre il momento più difficile, perché man mano che si cresce, che si affrontano esperienze nuove e che si raggiungono nuovi traguardi, cresce il numero di persone a cui dire grazie. Del resto, credo che non sarei quella che sono, se oggi dovessi dire grazie solo a me stessa.

Il dottorato rappresenta per me un importante traguardo, ma forse anche l'inizio di una nuova fase della mia vita in cui davvero devo imparare a contare solo su me stessa e sulle mie capacità. Se oggi ho la consapevolezza di "saper muovermi con le mie gambe" è perché sono circondata da tante persone meravigliose a cui va il mio grazie.

Grazie innanzitutto al mio tutor, il professore Gennaro Magliulo, che per primo ha creduto in me, permettendomi di svolgere interessanti attività nel settore dell'ingegneria sismica. La sua grande onestà e dedizione nel lavoro di ricerca e nella didattica rappresentano per me un modello imprescindibile di uomo e professionista.

Grazie ad Ernesto Di Maio, che mi ha insegnato tutto quanto attualmente conosco circa la meccanica di materiali innovativi, o per meglio dire a me ignoti! Il suo modo di fare allegro e disinvolto hanno spesso reso il lavoro di ricerca più piacevole e leggero.

Grazie a Marianna che da tutor di tesi specialistica mi ha trasmesso la passione per la ricerca ed è diventata una collega, un'amica ed un punto di riferimento.

Grazie a Crescenzo che con generosità, mi ha trasmesso parte della sua immensa conoscenza nell'ambito dei componenti non strutturali. Devo gran parte del mio lavoro e della mia crescita professione a lui, alla sua grande genialità e al suo talento per la ricerca e la didattica.

Grazie a Maddalena! Questo è un ringraziamento speciale, perché quando lei ha iniziato il suo percorso di dottorato, credevo di avere incontrato semplicemente una collega e invece ho scoperto in lei una persona straordinaria, un'amica su cui poter contare sempre. Tutti i momenti duri del mio percorso li ho superati grazie

[1] I have chosen to write these few pages in Italian because is the language of my feelings and my thoughts.

ai suoi consigli, al suo sorriso dolce e al suo sguardo affettuoso. In tutti i momenti allegri lei c'è sempre stata, a ridere e gioire insieme a me.

Grazie ai miei tesisti, Paola, Diletta e Giuseppe, che con il loro lavoro hanno contribuito in maniera sostanziale alla conclusione di questo lavoro di tesi. Ringrazio con particolare affetto Giuseppe per la sua grande dedizione al lavoro ed il grande aiuto nella fase finale della stesura della tesi.

Grazie ai miei compagni di stanza, Maria Chiara e Raffaele che mi hanno sempre regalato un sorriso, e a Fabio e Gigi: sebbene abbiamo condiviso la stanza per pochi mesi, sono diventati per me grandi amici anche al di fuori del Dist.

Grazie a Sandro, Federica, Donatella e Iolanda per l'affetto e la stima che mi mostrano ogni giorno.

Grazie ad Antonio, Ciro, Iolanda, Marco, Paolino e Stefano, i colleghi dell' "altra stanza" con cui ho condiviso l'ansia della consegna della tesi.

Grazie a Nicola Sorriso che a pochi giorni dalla scadenza, nei momenti di massima agitazione, si è seduto accanto a me ed ha trovato sempre una soluzione ai miei problemi.

I ringraziamenti finali vanno alle persone che amo di più al mondo. Grazie a mamma e papà, semplicemente per esserci, per avermi insegnato a lottare duramente per raggiungere un traguardo e per la grade fiducia che ripongono in me. Grazie a Chiara che, da sorella minore, mi reputa un esempio da seguire. Il dialogo ed il confronto con lei spesso mi hanno fatto crescere più di quanto lei stessa non sappia.

Grazie a Michele, a lui dedico questa tesi e la gioia di questo momento. Grazie perché mi ha fortemente motivato ad intraprendere il percorso del dottorato, sapendo che sarebbe stata la scelta giusta. Nei momenti di sconforto, che non sono mancati, il suo amore è stato ancora di salvezza insostituibile.

Grazie alle mie amiche di sempre, Elisa, Serena e Titta che, sono sicura, stanno condividendo la mia gioia.

Ringrazio infine la Siniat Internaional s.p.a e la Hypucem s.r.l che hanno contribuito in maniera sostanziale allo svolgimento di questo lavoro di tesi.

Napoli, marzo 2015

Orsola

Abstract

The role of nonstructural components during a seismic event represents a key issue in the modern performance-based seismic engineering. Nonstructural components are usually defined as secondary structures, since they are not designed to bear horizontal forces or vertical loads. Nevertheless, they must still have suitable features to ensure their integrity in the aftermath of an earthquake.

Indeed, the damage of nonstructural components can have significant consequences on the operability of strategic buildings, on the human life safety, but can also have a relevant economic impact related to the post-earthquakes retrofitting actions. The above mentioned motivations highlight that a rational seismic design is required for secondary structures.

The modern technical codes should provide appropriate analysis methods to define the seismic capacity of nonstructural components and establish design criteria aimed at protecting the secondary structure from the effects of the earthquakes.

The present work focuses on innovative solutions for nonstructural components, namely partition walls and cladding panels, both in residential and industrial buildings. Particular attention is given to the seismic performance assessment of plasterboard panels, nowadays widespread in the European area as internal partition systems. The seismic capacity of such components can be assessed by means of experimental tests or numerical models capable to simulate the real behavior of the analyzed systems. In this work, experimental test performed on high plasterboard partitions, i.e. with height equal to 5 meters, are presented. Ten specimens, representative of the most common plasterboard panels' typology, are subjected to quasi-static cyclic tests in order to evaluate their in-plane seismic behavior. The experimental results show ductile behavior of the tested partitions, which achieve very high inter-story drift at the collapse (usually larger than 1%). On the base of the tests outcomes, a reliable numerical model technique, able to predict the collapse inter-story drift ratio, is proposed and validated. The validated finite element model is then extended to several plasterboard partition typologies whose geometrical features do not allow the experimental assessment. Moreover, a parametric study is carried out in order to identify the influence of some geometrical

parameters on the definition of the inter-story collapse drift. To reduce the computational effort in the partitions FEM model definition and analysis, a computer tool, interfacing the SAP2000 finite element structural program and the Matlab platform, is developed. By inserting in the input file the main features of the plasterboard panel to assess, the tool automatically performs the analysis and evaluates the collapse drift.

The last part of the work focuses on an experimental test campaign aimed at the mechanical characterization of an innovative material, namely a hybrid cement-polyurethane foam. Compressive, tensile and shear test are carried out on the base of ASTM (American Society for Testing and Materials) standards for rigid cellular plastic materials. The lightweight and the high deformability features of the hybrid foam, joined to sound insulation, fire resistance and water vapor permeability make the material suitable for nonstructural components also in seismic zones.

Keywords: Nonstructural components, Seismic assessment, Plasterboard, Internal partitions, Inter-story drift, Finite element model, cement-polyurethane hybrid foam.

Table of contents

List of figures

List of tables

Chapter 1

INTRODUCTION

"Secondary structures, are those system and element housed or attached to the floors, roof, and walls of building or industrial facility that are not part of the main or intended loadbearing structural system for the building or industrial facility, but may also be subjected to large seismic forces and must depend on their own structural characteristic to resist these forces." (Villaverde, 1997). This definition provides an essential information about the rule of the nonstructural components that, despite their name, are not secondary in importance, especially after the occurrence of a ground motion.

Recent seismic event demonstrated that the collapse or the damage of such components could critically affect the performance of the whole structure. An example is provided by the San Salvatore hospital in L'Aquila, Italy, struck by the earthquake in 2009. In this case, the failure of the brick partitions, the collapse of suspended ceiling systems, besides the failure of equipment and the furniture overturn, caused the hospital useless, even though the main structure did not show significant structural damage (Price et al., 2012).

Also during the most recent Emilia earthquakes (2012), the collapse of many nonstructural components, such as internal partitions, ceilings and high-rack steel structures, mainly in industrial precast buildings, was recorded. The unsuitable performance of such nonstructural components caused many trouble to production activity. It has been roughly estimated that the induced economic damage, e.g. the loss due to the industrial production interruption, amounts to about 5 billion euros. In the same structural typology, the collapse of horizontal and vertical cladding panels was one of the most widespread damages. In this case, the lack of seismic

design in cladding panel-to-structural element connection devices, which allows accommodating the structure deformations during the seismic excitation, was the main cause of their collapse. Furthermore, the panel-to-structure interaction, not taken into account during the design process of these nonstructural components, causes additional lateral forces in the connection devices, resulting in their failure. The collapse of such heavy precast concrete panels, classified as secondary structures, caused a serious risk to people, escaping from the building during the earthquake (Magliulo et al., 2014).

1.1 Motivation

The framework presented above emphasizes the rule of the secondary structure during an earthquake. Three main issues can be recognized to motivate the present study, besides several previous works related both to the evaluation of the seismic capacity and the demand of nonstructural components.

Firstly, nonstructural components can cause injuries or deaths after an earthquake; for instance the 64% of the fatalities caused by 1995 Great Hanshin Earthquake was due to the compression (suffocation) of the human body (Ikuta and Miyano, 2011). Such a phenomenon could be caused by the damage to nonstructural components that may also obstruct the way out from the damaged building, as it happened during the Emilia Earthquake due to the collapse of precast cladding panels (Figure 1.1).

Figure 1.1 – Collapse of precast cladding panels in industrial buildings during the Emilia earthquakes (2012)

Also in case of collapse of ceiling systems, suspended light fixtures, parapets or signboards, the life safety is jeopardized. Furthermore, the overturn of heavy equipment, bookshelves, storage racks, as much as the rupture of pipes or containers with toxic materials can cause injury or death.

Moreover, nonstructural components generally exhibit damage for low seismic demand levels. In frequent, and less intense, earthquake, the secondary structures damage can cause the inoperability of several buildings. Damage to electronic equipment, servers and machinery may result in service interruption of strategic facilities, like hospitals or center of civil protection, essential to provide recovery and emergency service, aftermath the seismic event (Figure 1.2).

Figure 1.2 - Damages recorded in San Salvatore hospital brick partitions, after the L'Aquila earthquake in 2009

Finally, it should be noted that the cost related to nonstructural components represents the largest portion of a building construction. Taghavi and Miranda (2003) evidenced that structural cost typically represents a small portion of the total cost of a building construction, corresponding to 18% for offices 13% for hotels and 8% for hospitals (Figure 1.3). The cost connected to the loss or the damage of nonstructural components themselves or related to the loss of business income may exceed the cost of total replacement of the building housing the nonstructural components.

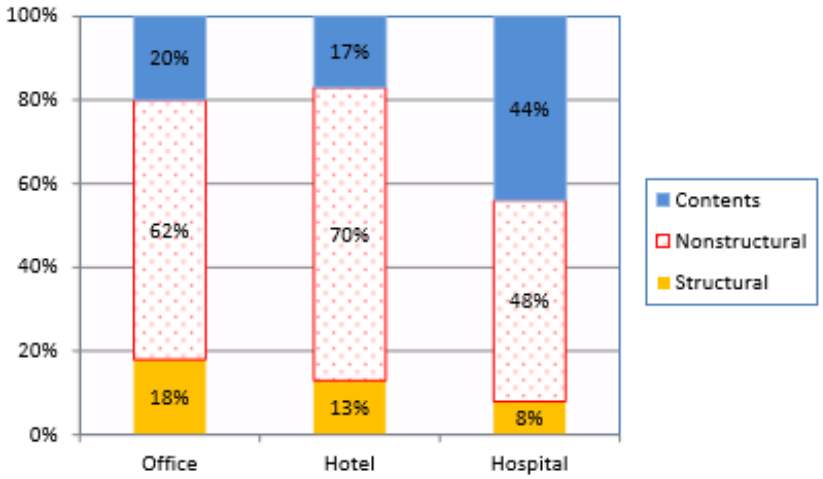

Figure 1.3 – Cost related to constructions of typical office, hotel and hospital buildings (after Taghavi and Miranda, 2003)

1.2 Objectives

The motivations outlined above highlight that the damage of nonstructural component may result in direct economic loss or downtime and therefore emphasizes that nonstructural component should be carefully designed in seismic areas, with particular attention to the performance assessment following earthquakes. In the last years, the selection of the suitable nonstructural system, capable of accommodating the deformations of the main structure during the earthquake without exhibiting significant damage and compromising the operability of the building, has represented a critical aspect. After all, the performance of nonstructural components, such as internal partitions and infill or cladding panels is recognized to be a key issue in the framework of Performance-Based Earthquake Engineering – PBEE – (Bertero and Bertero, 2002). This background provides the main purposes of this thesis, which are:

- improving the knowledge about the seismic in-plane behavior of innovative nonstructural components, i.e. plasterboard internal partitions;
- developing a reliable numerical model able to predict the in plane seismic behavior of such components;
- providing an automatic tool for the seismic assessment of plasterboard internal partitions;

– introducing innovative solutions of seismic protection of nonstructural internal partitions and infills.

The objectives here presented are achieved by studying the seismic performance of nonstructural component, such as plasterboard internal partition, by means of experimental tests on the most widespread configurations. The experimental results are therefore used to calibrate the proposed numerical model.

A new lightweight material is studied for nonstructural components applications by performing experimental test for mechanical characterization.

1.3 Organization and outlines

The common thread of this thesis is represented by the seismic protection of nonstructural component, whose importance is highlighted by the introduction and the motivations presented in the ***Chapter 1***. This chapter briefly introduces also the goals of the work and the adopted strategies to achieve them.

Firstly, the seismic in-plane behavior of plasterboard internal partitions is assessed in the ***Chapter 2***. The results of experimental quasi-static tests performed on high partitions are shown, in terms of recorded damage and achieved drift up to the partitions collapse. Details about the test setup and specimen configurations are also provided, besides of information regarding the test protocol and the specimens' instrumentations.

Then, in ***Chapter 3***, an original modeling technique for plasterboard partitions is proposed and validated**.** The validation is pursued by comparing the outcomes achieved by the nonlinear static analyses performed on the partitions' numerical model, with the results of the experimental tests.

The efficiency of the validated model allows to extend it to several plasterboard partition configurations, different from the tested ones, as shown in ***Chapter 4***. In this chapter, an automatic tool based on the presented numerical model, able to evaluate the inter-story drift required to induce the partition failure, is presented.

The ***Chapter 5*** deals with the mechanical characterization of a new lightweight material, namely a polyurethane – cement hybrid foam, recently introduced in the building construction field. The used experimental techniques are detailed and the resulting mechanical features of the hybrid foam are compared to those of others lightweight materials, generally used for nonstructural purpose.

The final remarks of the work herein presented are listed in ***Chapter 6***.

Chapter 2

EXPERIMENTAL TEST ON HIGH PLASTERBOARD PARTITIONS

Plasterboard internal partitions with steel studs are very common nonstructural components, since they are typically employed in several building typologies all over the world. Modern plasterboard partition systems are now widespread in the European area, mainly in industrial buildings. They are usually designed in order not to interfere with the hosting structure, up to moderate level of inter-story drifts (<0.5 %). Different experimental studies aiming at the evaluation of the seismic capacity of such components are available in literature. In Magliulo et al. (2012) and (2014) shaking table tests are performed to assess the seismic behavior of plasterboard partitions. In order to investigate a wide range of inter-story drift demand and seismic damage, the shakes are performed by using accelerograms at different intensity levels.

Also, in Retamales et al. (2013) a description of the experimental results of full-scale tests performed on several cold-formed steel-framed gypsum partitions is reported. The experimental data, including different partition wall configurations, in terms of wall dimensions, material type, testing protocol and boundary conditions, are used in order to create seismic fragility curves for such nonstructural partition walls.

The seismic performance of drywall partition is recently assessed in Tasligedik et al. (2015). The Authors developed a low damage solutions in order to obtain plasterboard partitions capable of reaching high levels of drift without loss of

serviceability. Quasi-static tests are performed under increasing drift amplitudes to investigate the solution feasibility.

In all the mentioned works, the seismic evaluation is typically expressed in terms of the Engineering Demand Parameter (EDP) that is required to reach a certain Damage State (DS). In the presented work, the inter-story drift is selected as the EDP in order to compare it to the design limits set by the European standards (CEN, 2005). In this chapter, the experimental test performed on plasterboard partitions components is illustrated. Particular attention is given to the description of the tested partition and the mounting procedure in order to justify the finite element modeling of the specimens, included in Chapter 3.

2.1 Setup and specimens configuration

The experimental campaign, conducted at the Laboratory of the Department of structure for engineering and architecture of the University of Naples Federico II, in cooperation with the Siniat International company, aimed at evaluating the seismic performance of tall (up to 14 m) plasterboard partitions. The study was carried out on 10 plasterboard internal partitions (Petrone et al., 2014), which are representative of the typical partitions used in industrial and commercial buildings in the European countries. The height of the partitions is chosen equal to 5 meters due to the physical limit of laboratory facilities.

The test system consists of a steel frame setup, the specimen, i.e. a plasterboard partition, a hydraulic actuator and a reaction wall (Figure 2.1).

Figure 2.1 - Global view of test setup

The steel test frame is conceived as a statically indeterminate scheme (Figure 2.2) in order to transfer the load provided by the hydraulic jack to the partition without absorbing lateral forces. Moreover, since the reaction wall cannot reach the height of the system, the actuator is placed at the middle height of the test setup. In this way, a given displacement produced by the actuator is doubled at the top of the setup, assuming a rigid behavior of the vertical column.

The test frame is composed of:

- no.1 vertical loading column : profile HEB 450, steel S355 and length of 4.785 m;
- no.2 lateral columns: tubular profile 180x180x10 mm, steel S355 and length of 4.785 m;
- no.1 top horizontal beam: profile HE 280, steel S355 and length 5.37 m;
- no.1 base beam : profile HE 280, steel S355 and length 5.37 m;

The different elements are connected by pin connections, according to the assumed mechanism. Further details on the setup definition are included in (Petrone et al., 2014).

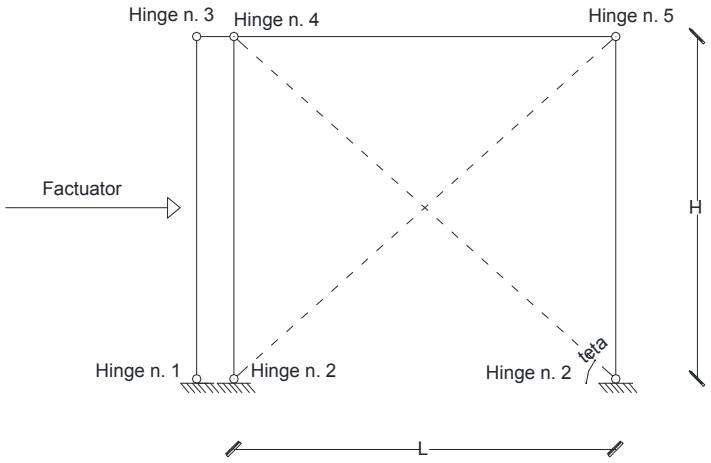

Figure 2.2 - Test static scheme

All the specimens, i.e. the plasterboard partitions, are 5.0 m high and 5.13 m wide and are constituted, according to the mounting sequence, by:

- two horizontal U guides made of 0.6 mm thick galvanized steel screwed, both at bottom and at top, in the wooden beams;

- two vertical U guides made of 0.6 mm thick galvanized steel screwed in the wooden beams;
- C-shaped studs made of 0.6 mm thick galvanized steel. They are placed in the horizontal guides without any mechanical connection (see Figure 2.3a);
- steel plates (Figure 2.3b), used only in some partitions (partition P-3 of Table 2.1), with a rectangular cross-section 100 mm x 0.6 mm, connected to the studs at different heights of the partition with a single screw;
- one or two layer of gypsum plasterboard for each side of the partition. The plasterboards are connected to the studs and to the steel plates by screws (see Figure 2.3c); they are assembled in rows so as to define one or more horizontal joints. The joints are sealed with paper and joint compound (Figure 2.3d).

In Table 2.1 the main features of the tested partitions are listed. The ten partitions differ from each other for:

- steel stud cross section dimensions;
- steel stud typology: simple or back-to-back;
- horizontal studs spacing;
- plasterboard typology;
- number of plasterboard layer for each side of the partition;
- horizontal and vertical spacing of the screws connecting the boards to studs.

The panels arrangement, function of the panel dimension, defines the positions of the horizontal and vertical joints that, as reported hereafter, play an important role in the in-plane behavior of the partitions. An example of panels arrangement is showed in Figure 2.4 for the internal layer, and in Figure 2.5 for the external one. Usually, the panel of the first and the second layer are staggered, so that the internal vertical joints do not correspond to the external ones.

In the last column of the table, the vertical spacing of the screws, connecting the board to the vertical studs, is shown. As reported, if a double layer of board is provided for each side of the partition, a different screws spacing is defined for internal and external panels.

Partitions from P-1 to P-4 are representative of typical plasterboard generally used for internal partition system; the partition P-5 can be considered innovative with respect the previous ones, since a gap between the specimen and the surrounding frame is provided, by silicone interposition.

Partition from P-6 to P-8 are characterized by two layer of staggered steel stud, as shown in Figure 2.6; while partitions P-9 and P-10 are conceived as antiseismic partition, since particular fuse system are introduced in order to concentrate the damage in the specimen corner, up to high inter-story drift, and simplify the panel retrofitting. More details are reported in Petrone et al. (2014)

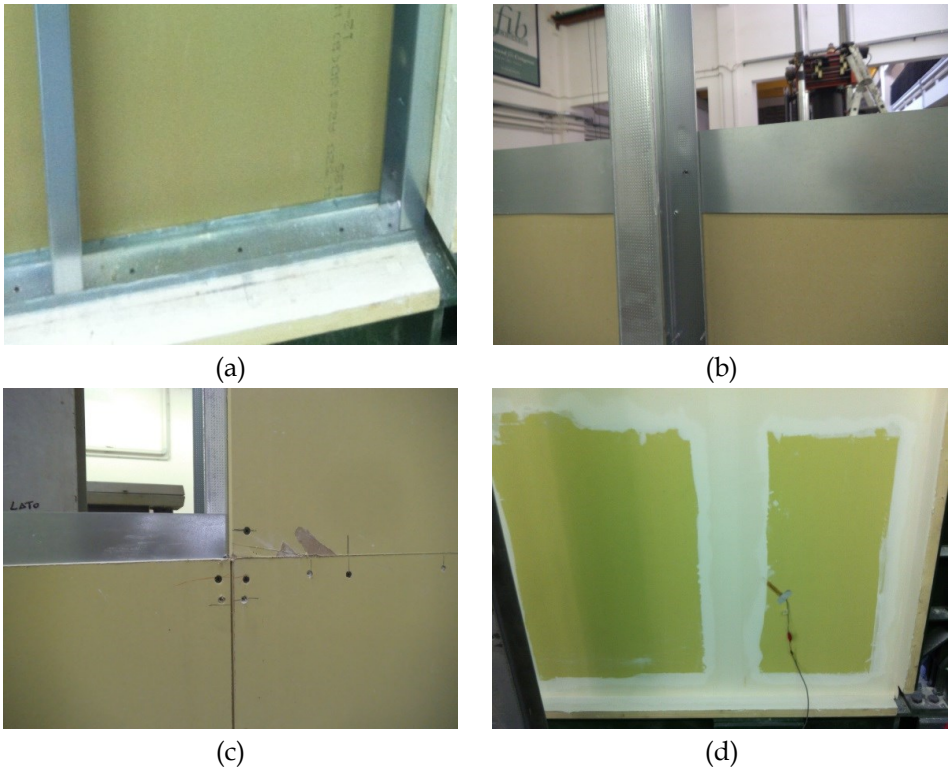

(a) (b)

(c) (d)

Figure 2.3 - Specimen mounting: (a) studs arranged in the horizontal guide, (b) steel plate connected to the stud, (c) panel screwed to the stud and steel plate, (d) paper and joint compound.

Code	Panel dimension		Number of layer	Stud typology	Stud dimension			Stud spacing	Screw spacing
	width	*thickness*			*web*	*flange*	*thickness*		
P-1	1.2 m	12.5 mm	2	back to back	150 mm	50 mm	0.6 mm	600 mm	600 mm internal layer 300 mm external layer
P-2	1.2 m	12.5 mm	2	simple	150 mm	50 mm	0.6 mm	600 mm	600 mm internal layer 300 mm external layer
P-3	0.9 m	18.0 mm	1	simple	100 mm	50 mm	0.6 mm	900 mm	250 mm
P-4	1.2 m	18.0 mm	2	back to back	100 mm	50 mm	0.6 mm	400 mm	600 mm internal layer 300 mm external layer
P-5	0.9 m	18.0 mm	1	simple	100 mm	50 mm	0.6 mm	900 mm	250 mm
P-6	1.2 m	18.0 mm	1	simple	150 mm	50 mm	0.6 mm	600 mm	300 mm
P-7	1.2 m	12.5 mm	2	simple	100 mm	50 mm	0.6 mm	600 mm	600 mm internal layer 300 mm external layer
P-8	1.2 m	18.0 mm	1	simple	100 mm	50 mm	0.6 mm	600 mm	250 mm
P-9	0.9 m	18.0 mm	1	simple	100 mm	75 mm	0.6 mm	900 mm	250 mm
P-10	0.9 m	18.0 mm	1	simple	100 mm	50 mm	0.6 mm	900 mm	250 mm

Table 2.1 – Main geometrical features of the tested partitions

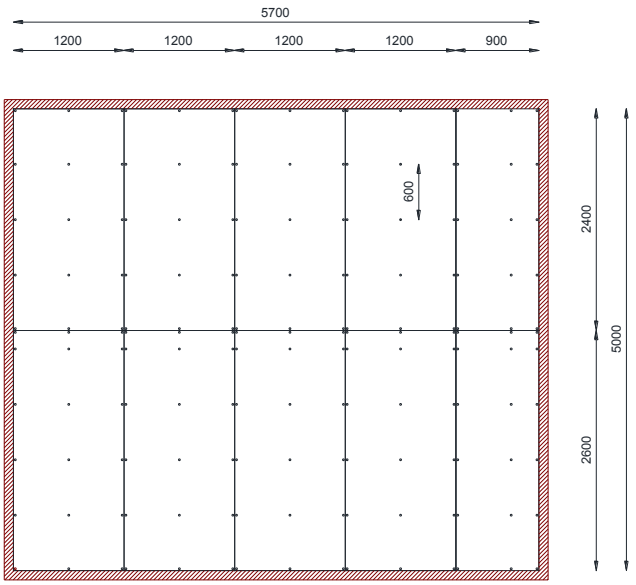

Figure 2.4 - Typical panel arrangement in the internal layer

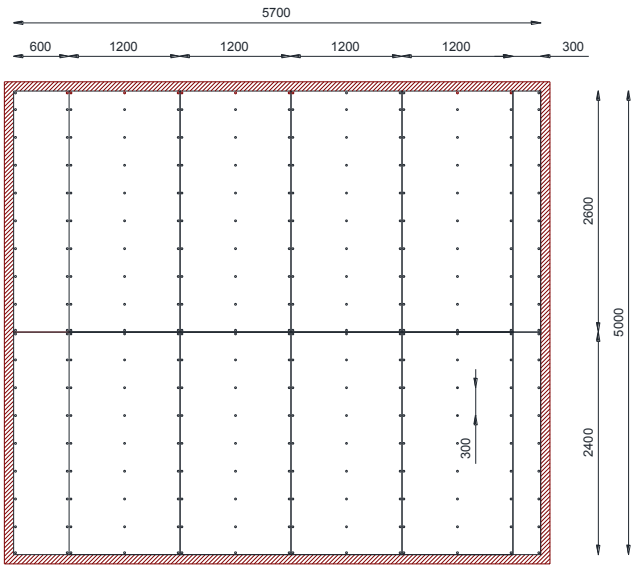

Figure 2.5 - Typical panel arrangement in the external layer

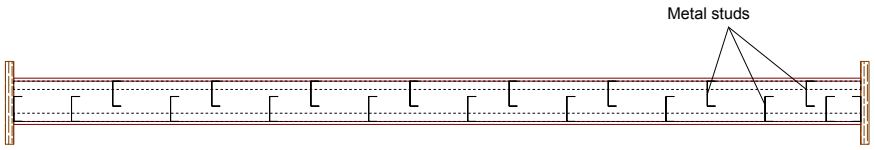

Figure 2.6 – Plane view of the tested partitions with double layer of staggered steel stud

2.2 Test protocol and instrumentation of the setup

Each partition is subject to quasi static cyclic test, performed in displacement control, according to the testing protocol provided by Federal Emergency Management Agency (FEMA) (2007). It provides a displacement control history loading, which amplitude increases in time, as shown in Figure 2.7.

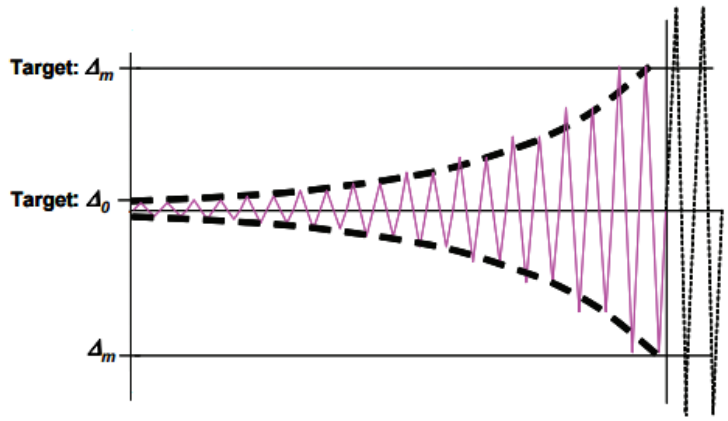

Figure 2.7 – Shape of history for displacement control test Federal Emergency Management Agency (FEMA), 2007

The emphasized parameters are:

- Δ_0= smallest targeted deformation amplitude of the loading history. At the lowest damage state at least six cycles must have been executed.
- Δ_m= maximum targeted deformation amplitude of the loading history. It is an estimated value of the imposed deformation at which the most severe damage level is expected to initiate.
- n = the number of steps (or increments) in the loading history, generally 10 or larger.
- a_i = the amplitude of the cycles, as they increase in magnitude, i.e., the first amplitude, a_1, is Δ_0 (or a value close to it), and the last planned amplitude, a_n, is Δ_m (or a value close to it).

The F.E.M.A. proposes a history loading as numeric succession on two successive steps a_i and a_{i+1} as:

$$a_{i+1} = c \cdot a_i \qquad (2.1)$$

The F.E.M.A. equation has been calibrated on a set of ground motions acceleration in ordinary conditions (not near fault) recorded in US area. The suggested value of the parameter c is 1.4.

For the tests on plasterboard partitions the objective is to adapt the same relationship on typical conditions of European ground motions. At this regard, a set of 14 European records has been considered to estimate a value of parameter conforming to European conditions. The earthquake features are reported in Table 2.2, the spectra corresponding to the acceleration records are shown in Figure 2.8.

Earthquake code	Eartquake name	Earthquake country	Date	PGA-x [m/s^2]	PGA-y [m/s^2]
000187	Northern and central Iran	Iran	16/09/1987	9.68	10.80
000196	Montenegro	Yugoslavia	15/04/1979	4.45	3.00
000199	Montenegro	Yugoslavia	15/04/1979	3.68	3.56
000230	Montenegro (aftershock)	Yugoslavia	24/05/1979	1.17	2.62
000291	Campano lucano	Italy	23/11/1986	1.53	1.72
005263	South Iceland	Iceland	17/06/2000	6.14	5.02
005334	South Iceland (aftershock)	Iceland	21/06/2000	4.12	7.07

Table 2.2 – Set of European ordinary ground motions considered in the input definition study

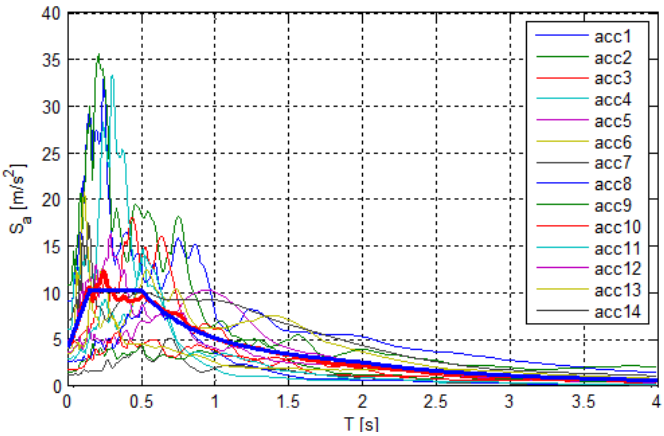

Figure 2.8 – Spectra of the records considered in the input definition study and EC8 spectrum

The study consisted in performing linear dynamic analyses on a simple degree of freedom (S.D.O.F) system in which the input was the set of European records. For every record, it was considered a S.D.O.F. characterized by 3 different value of the fundamental period T.

Based on the displacement response history of the different SDOF systems, a protocol history loading is calibrated. The relationship between two successive steps in terms of displacement amplitude is as follows, depending on two parameters, i.e. *c* and *b*:

$$\frac{a_{i+1}}{a_n} = \left(c \cdot \frac{a_i}{a_n} \right)^b \qquad (2.2)$$

The parameters are calibrated in order to minimize the scatter between the given relationship and the analysis data, yielding:

$$\frac{a_{i+1}}{a_n} = \left(1.80 \cdot \frac{a_i}{a_n}\right)^{1.47} \qquad (2.3)$$

Moreover, a relationship assuming b=1 is evaluated:

$$a_{i+1} = 1.39 \cdot a_i \qquad (2.4)$$

In spite of the minor standard deviation of the first relationship (2.3), it shows to be less adapt to emphasize the intermediate damage states with respect to the second relationship (2.4).

In fact, a typical test protocol designed on 15 cycles in amplitude of displacements shows that the amplitude has got a low increase in the first steps, while it exhibits a very sharp variation in the last cycles. Hence, in order to study intermediate damage states, the second formulation is adopted.

The next figure shows the load pattern of the test protocol in terms of drift ($\theta=\delta_{top}/H_{partition}$):

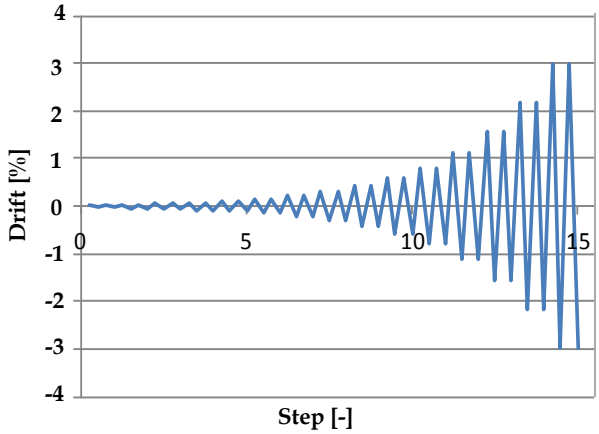

Figure 2.9 - History loading in terms of drift

Different measuring instruments are used in order to monitor the specimen behavior during the cyclic tests. The monitoring system provides the following instrumentation typologies:

- two displacement laser sensors, placed at half the height of the column and at the top of the same column, respectively, in order to monitor top in-plane displacement and verify the rigid movement of the vertical column;

- two wire potentiometers, placed in parallel with respect to the laser sensors (see Figure 2.10);
- two displacement transducers (LVDT - linear variable differential transformer) placed at the two edges of the top horizontal beam, the first one is placed on the left side ("0") and the second one on the right side ("N") as reported in Figure 2.10, which measure out-of-plane displacements, in order to validate the planarity of the motion;
- a series of strain gauges, divided between the steel studs and the plasterboards. Usually six strain gauges are located in the inner part of the specimen on the steel stud flanges, as shown in Figure 2.11; an equal number of strain gauges is placed in the external part (Figure 2.12), in order to evaluate the plasterboard local deformations.

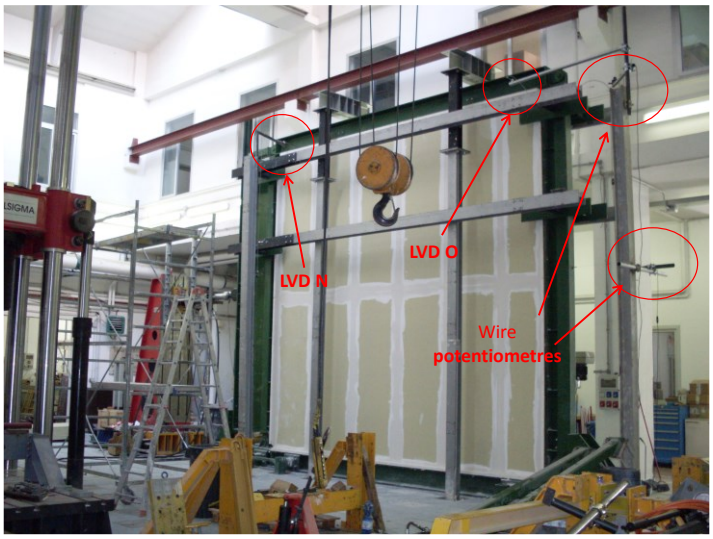

Figure 2.10 – Instrumentation aimed at evaluating the in plane (wire potentiometer) and out of plane (LVDT) displacements

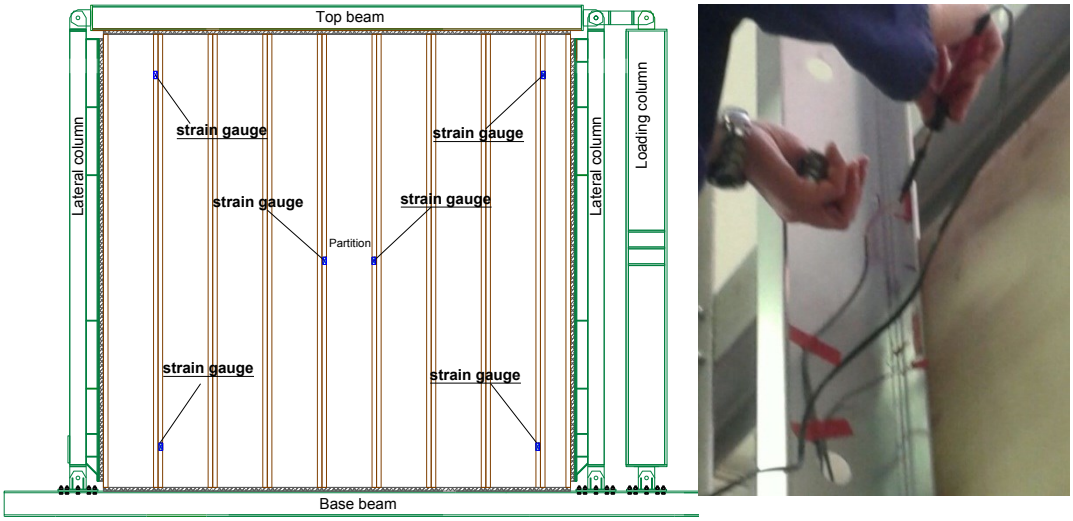

(a) (b)

Figure 2.11 – (a) Strain gauges disposition in the inner part of the specimen (metal studs flanges) and (b) particular of the strain gauge installation

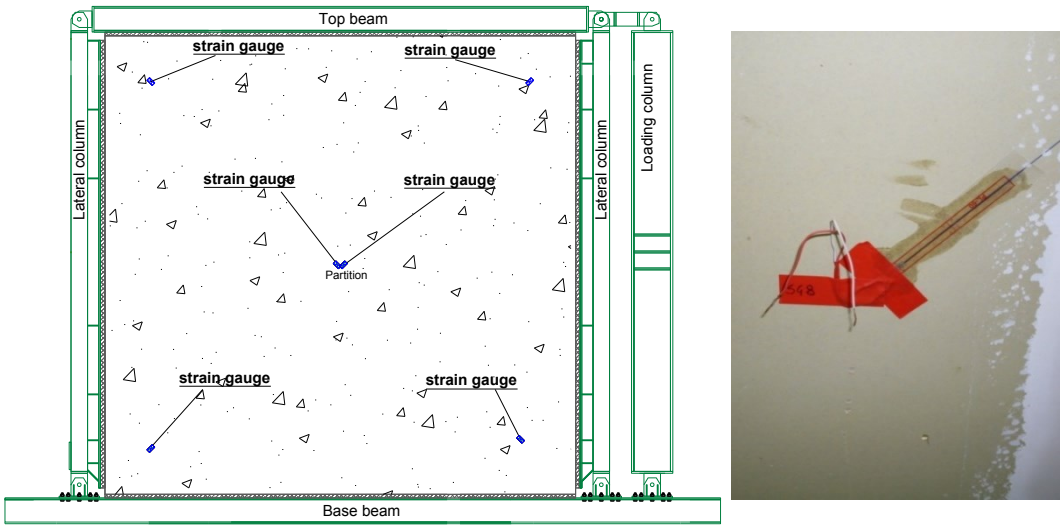

(a) (b)

Figure 2.12 – (a) Strain gauges disposition in the external part of the specimen (plasterboard panel) and (b) particular of the strain gauge installation

2.3 Experimental results

Although the test campaign refers to ten partition, as reported in the previous section (§2.1), in this section the experimental results related to the first four tested partition are presented. The results here presented are preliminary in order to make the numerical and experimental comparison and validate the numerical model, presented in the next chapter.

2.3.1 Partition P-1: 5.00 m high partition, with 600 mm spaced M150-50/6 back to back studs and a double layer of 12.5 mm thick panels

The relationship among the top force and the top displacement, resulting from the quasi static test conducted on the first partition, is shown in Figure 2.13.

The specimen presents a slightly not-symmetric behavior, since in the positive quarter, the force reaches its maximum value corresponding to a displacement equal to 24 mm, while in the negative quarter, the force reaches the maximum values for a displacement equal to 59 mm. In both quarter, it starts undergoing to inelastic deformations and loosing linearity under about 15 mm displacement, when plasterboards start to crack along the perimeter (Figure 2.14a). For a displacement equal to 105 mm the collapse, due to buckling of a partition portion (Figure 2.14b), occurs. For this displacement value, the buckling is clearly visible in the hysteresis of Figure 2.13, since a great strength reduction is recognizable.

The specimen presents overall a high initial stiffness and a high ductility: even if it starts exhibiting damage in correspondence of a low drift 0.36% (< 5%), it reaches the collapse at a very high drift level (2.08%).

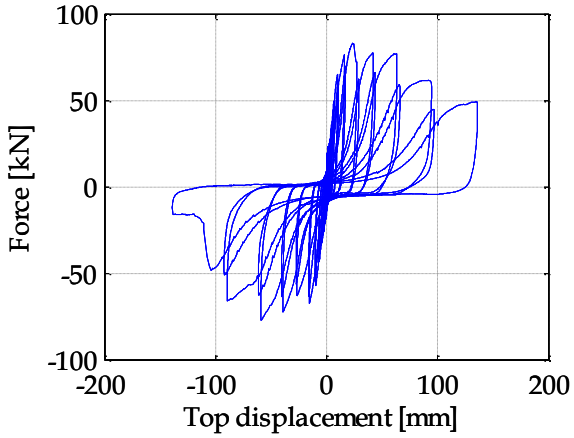

Figure 2.13 - Hysteretic curve exhibited by the partition P-1 under the selected test protocol

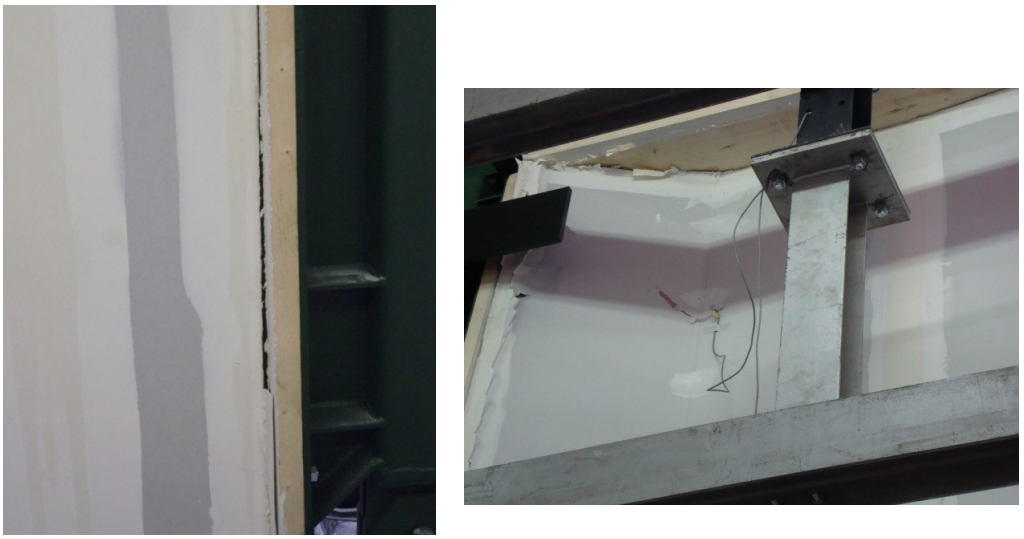

(a) (b)

Figure 2.14 - (a) Lateral panel – wooden column detachment and (b) buckling of a portion of the partition with consequent permanent dislocation of the horizontal guide

The Figure 2.15 and Figure 2.16 show the recordings in the strain gauges versus the time. The large amount of studs induces small deformations on the steel stud (sg1 – sg6 in Figure 2.15), below 0.4‰. The deformations recorded on the plasterboard panels (sg7 – sg12 in Figure 2.16) are larger than the ones recorded on the studs, i.e. up to 1‰. Moreover, the central plasterboard panels result less stressed with respect to the lateral ones.

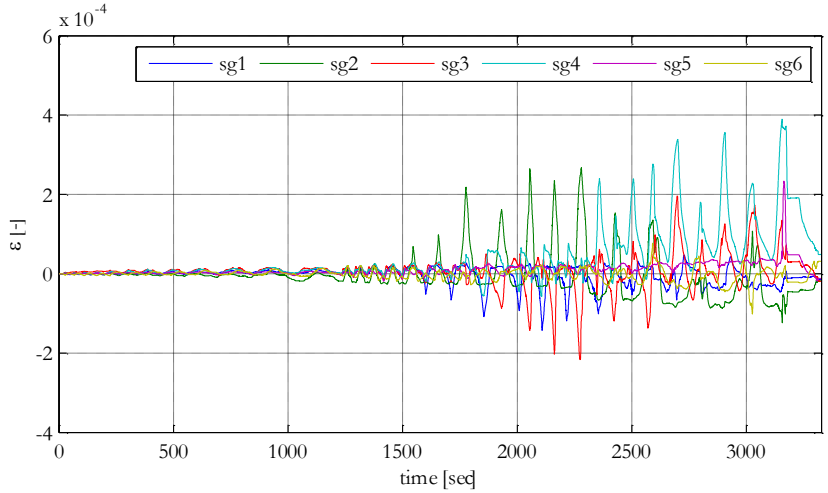

Figure 2.15 – Strain gauges recordings on the steel studs of partition P-1 during the test

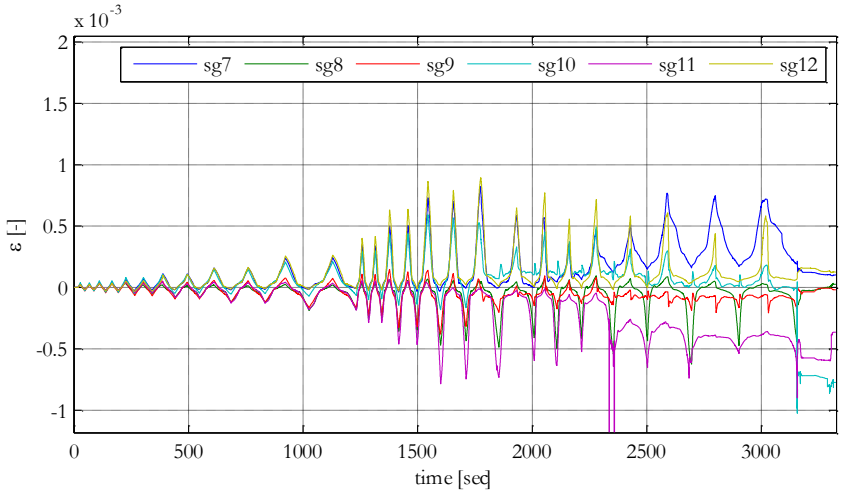

Figure 2.16 - Strain gauges recordings on the plasterboard of partition P-1 during the test

The seismic response of the plasterboard partitions can be referred to different limit state, as listed below:

1. operational limit state or SLO, identified also as damage state 1;
2. damage limit state or SLD, identified also as damage state 2;
3. life safety limit state or SLV, identified also as damage state 3;

Operational limit state achievement implies the need of repairing the damaged element, in order to restore the original condition. Damage limit state achievement, instead, implies that the component is damaged so that it must be partially removed and replaced; finally, life safety limit state implies that the damage level is such that life safety is not ensured or the partition must be totally replaced.

On the base of the previous definitions, it is possible to correlate the three limit states to the drift level (ϑ) reached by the partition in each step, using the damage recorded during the test, through the card of damage.

In particular, after a 0.34% drift the partition need further paper and compound, so the *damage state 1* is achieved. After a 0.87% drift the partition need to be partially replaced (*damage state 2* achievement), while the achievement of the *damage state 3* occurs for a 2.08% drift, i.e. when the buckling of a partition portion causes the failure of the whole partition.

2.3.2 Partition P-2: 5.00 m high partition, with 600 mm spaced M150-50/6 studs and a double layer of BA13 standard plasterboards

In Figure 2.17 the hysteretic curve, related to P-2 partition behavior during the quasi-static test performed in displacement control, is plotted. Also in this test, the specimen presents a slightly not-symmetric behavior. In particular: in the positive quarter, the force reaches its maximum value corresponding to a displacement equal to 24 mm, in the negative quarter the force reaches the maximum values for a displacement equal to 15 mm. It starts exhibiting damage corresponding to a displacement of 8 mm and loosing linearity under 16 mm. The collapse, due to buckling, occurs for a displacement equal to 150 mm, i.e. at a very high drift level (3.00%). The overall behaviour results in a high initial stiffness and a high ductility of the partition.

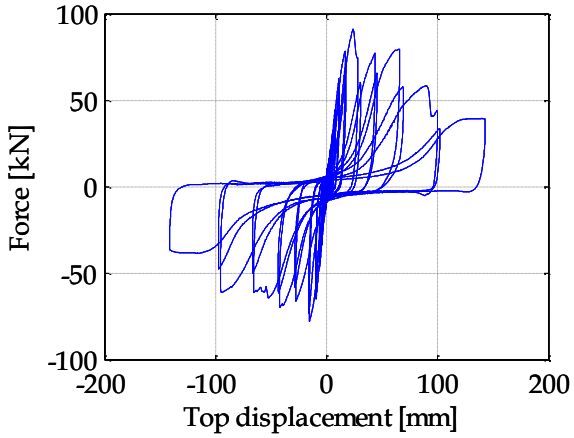

Figure 2.17 - Hysteretic curve exhibited by the partition P-2 under the selected test protocol

The deformations on the steel stud (sg1 – sg6 in Figure 2.18) are about 1.2‰. It is interesting to observe that when the stud buckling is reached the strain gauges record very small compressive strains, since the stud does not have any resistance to compressive forces anymore. The deformations recorded on the plasterboard panels (sg7 – sg12 in Figure 2.19) are slightly smaller than the ones recorded on the studs, i.e. up 0.8‰.

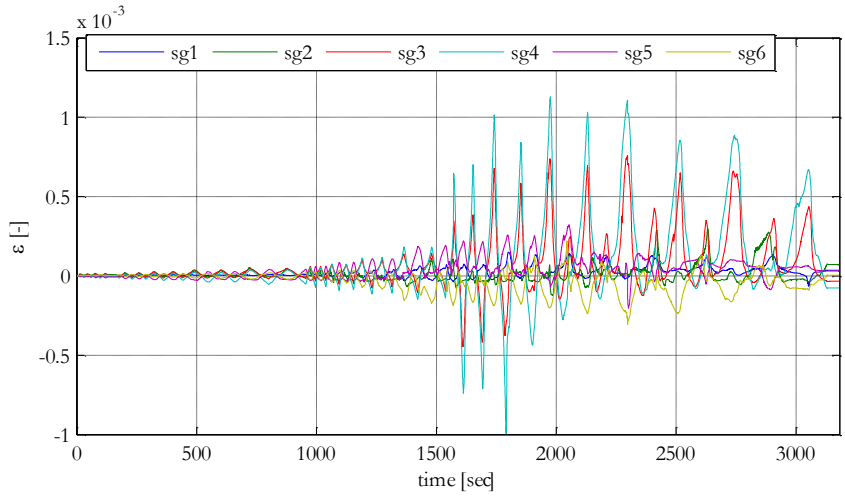

Figure 2.18 – Strain gauges recordings on the steel studs of partition P-2 during the test

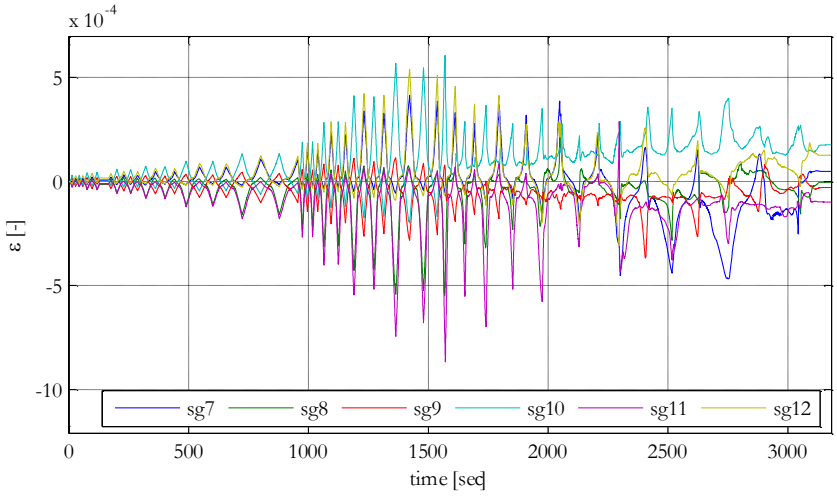

Figure 2.19 - Strain gauges recordings on the plasterboard of partition P-2 during the test

Referring to damage limit state, the minor drop of gypsum dust and cracks in the paper for a 0.16% drift, denotes the achievement of the *damage state1 (*Figure 2.20*a)*. For a 0.91% drift, the *damage state 2* is reached, since the detachment between adjacent panels (Figure 2.20b) and the first out of plane cusps imply a removal and replace of a partition portion. For an about 3.00% drift, severe damage are recorded: local plastic deformation on the panel, very large detachment between adjacent panel and out of plane cusp of the specimen denote risks for human life. The *damage state 3* is achieved (Figure 2.20c).

(a) (b) (c)

Figure 2.20 - Recorded damage for specimen P-2: (a) crack in paper (damage state 1), minor panel detachment (damage state 2), (c) global buckling of the partition with panel expulsion

2.3.3 Partition P-3: 5.00 m high partition, with 900 mm spaced M100-50/6 studs and a single layer of BA18S standard plasterboards

The relationship among the top force and the top displacement, resulting from the quasi-static test conducted on the partition P-3, is shown in Figure 2.21. It can be seen that the specimen exhibits a slightly non-symmetric behavior: in the positive quarter, i.e. the pushing direction, the force reaches its maximum value corresponding to a 20 mm displacement, while in the negative quarter the force reaches the maximum values to a 25 mm displacement.

The specimen starts undergoing inelastic deformation and losing linearity at a 11 mm displacement: some sounds denote the screws bearing the connected plasterboards, the paper installed between the adjacent panels starts cracking (Figure 2.20a) and a minor drop of gypsum is observed. For a 20 mm top displacement, when the maximum force is recorded, the paper between the different panels completely cracks. Corresponding to a 68 mm displacement, a global out-of-plane curvature of the specimen is exhibited (Figure 2.20b), i.e. the partition collapses due to the buckling of the studs. At this displacement value a significant strength degradation is visible on the hysteretic curve and the *damage state 3* is reached.

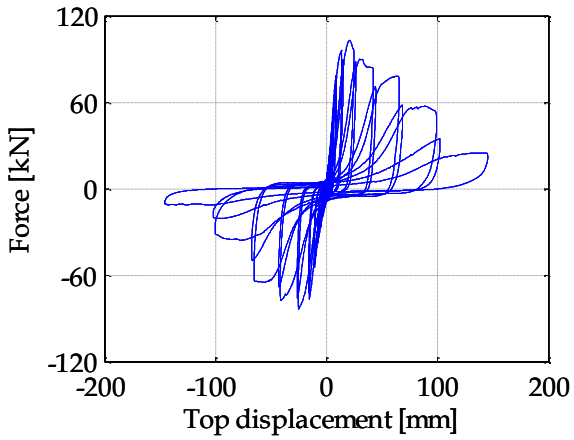

Figure 2.21 - Hysteretic curve exhibited by the partition P-3 under the selected test protocol

(a) (b)

Figure 2.22 - Partition damage: (a) visible opening on the paper of the lateral panel (0.20% drift) and (b) global out-of-plane curvature of the specimen (1.37 % drift).

In Figure 2.23 and Figure 2.24 the recordings in the strain gauges are plotted versus the time. The maximum deformation on the steel stud (sg1 – sg6) is about 0.8‰. The maximum deformation recorded on the plasterboard panels (sg7 – sg12) are slightly larger than the ones recorded on the studs, i.e. up 1.4‰.

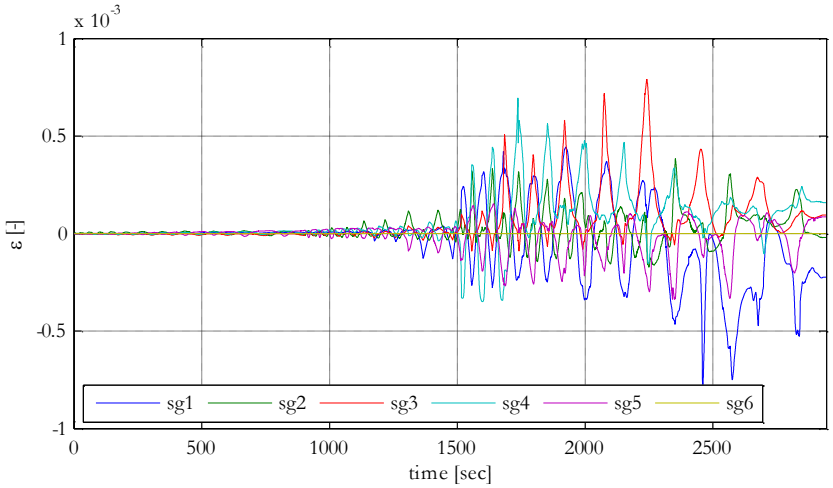

Figure 2.23 - Strain gauges recordings on the steel studs of partition P-3 during the test

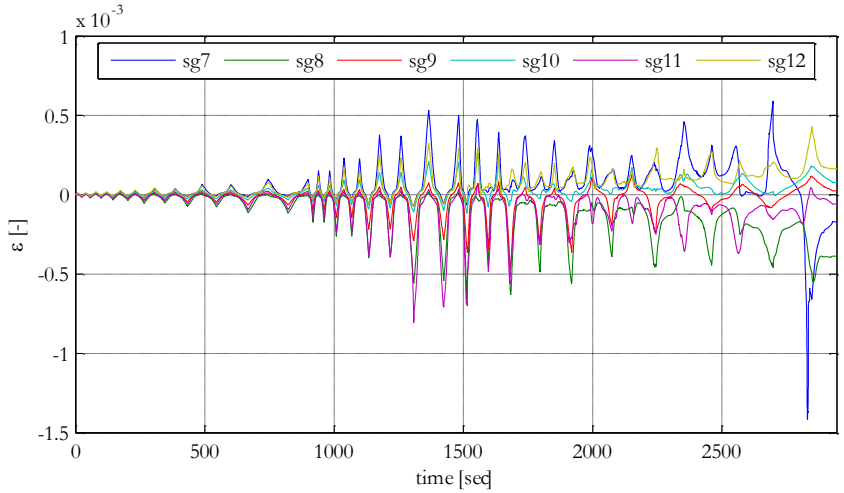

Figure 2.24 - Strain gauges recordings on the plasterboard of partition P-3 during the test

2.3.4 Partition P-4: 5.00 m high partition, with 400 mm spaced M100-50/6 back to back studs and a double layer of BA18 plasterboards

The force displacement curve of the fourth tested partition, shown in Figure 2.25, highlights a non-symmetric behavior of the specimen during the cyclic test. The specimen starts undergoing inelastic deformations and loosing linearity, under 9.7 mm displacement, presenting a visible opening on the paper of lateral panels and minor material drop. The buckling of a portion of the partition is clearly visible in the hysteresis for a displacement equal to 80.7 mm.

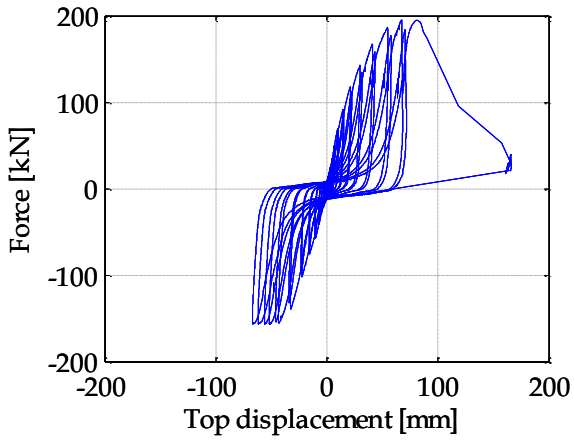

Figure 2.25 - Hysteretic curve exhibited by the partition P-4 under the selected test protocol

The strains recorded during the test are shown in Figure 2.26 and Figure 2.27. The maximum deformations on the steel stud (sg1 – sg6) are about 1.1‰. The deformations recorded on the plasterboard panels (sg7 – sg12) are slightly smaller than the ones recorded on the studs, i.e. up 0.9‰.

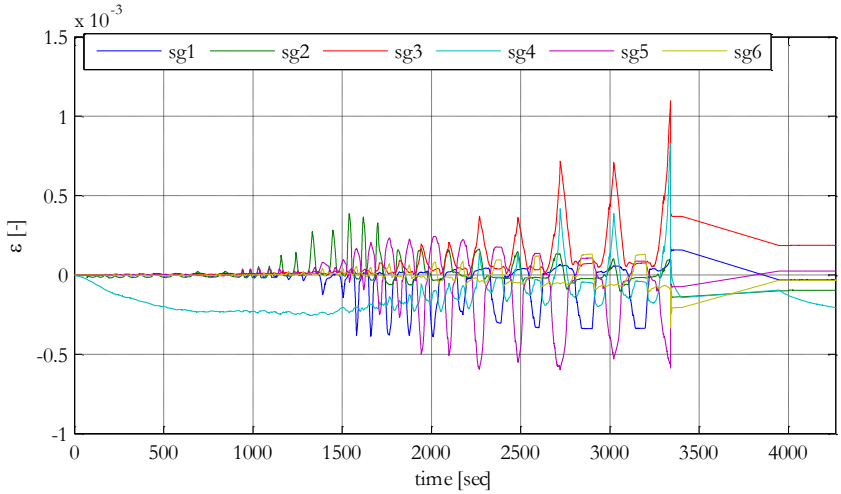

Figure 2.26 – Strain gauges recordings on the steel studs of partition P-4 during the test

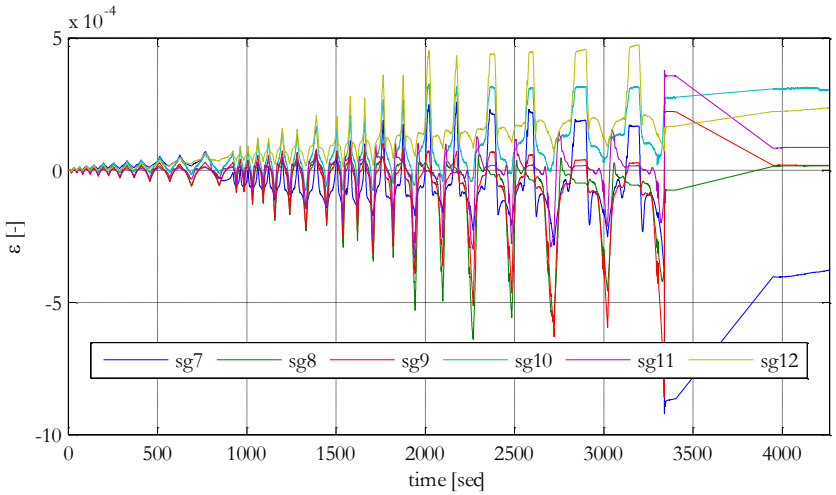

Figure 2.27 - Strain gauges recordings on the plasterboard of partition P-4 during the test

As for the previous specimen, also in this case the *damage state 1* is related to minor drop of gypsum dust and few openings in the paper, occurring for 0.32% drift. The *damage state 2* is achieved for a 1.15% drift, when diffusing slip of adjacent panels is recorded. The partition must be totally replaced (*damage state 3* achievement) when, for a 1.6% drift, the out of plane rotation of a specimen portion (Figure 2.28) and the expulsion of the top central panel is recorded.

Figure 2.28 - Out of plane rotation of a partition portion

Chapter 3

FEM MODEL OF THE TESTED PARTITION

In this chapter an original modeling technique for plasterboard partitions is proposed and validated. The aim is to define a proper finite element model able to evaluate the inter-story drift ratio that induces the failure of a generic plasterboard partition. The validation is performed comparing the analytical behavior of the specimen with the experimental results achieved in the quasi-static test campaign, conducted at the Laboratory of the Department of Structures for Engineering and Architecture at the University of Naples Federico II, described in Chapter 2.

3.1 Literature review of existing numerical model for plasterboard partitions

A literature review concerning the numerical modelling of wall nonstructural elements is provided. This literature review is mainly referred to gypsum partition walls with steel or wooden studs, whose model is calibrated on experimental tests.

An hysteretic modeling technique is proposed by Fulop and Dubina (2004) in order to assess the wall-stud cold-formed shear panel behavior. Using experimental results, achieved on fifteen wall panels under monotonic and cyclic loading, three different numerical techniques, from the simplest *bilinear* to the most complex *full nonlinear*, are employed to model the hysteretic behavior of the panels. The Authors validate the three models by performing dynamic nonlinear analysis and highlight

the importance of taking into account three main characteristic of the wall panel hysteretic behavior, i.e. pinching, over-strength and plastic deformation capacity. However, the wall panels of the mentioned study are considered as structural components capable to resist lateral forces. So they are different with respect the nonstructural plasterboard panels, herein presented.

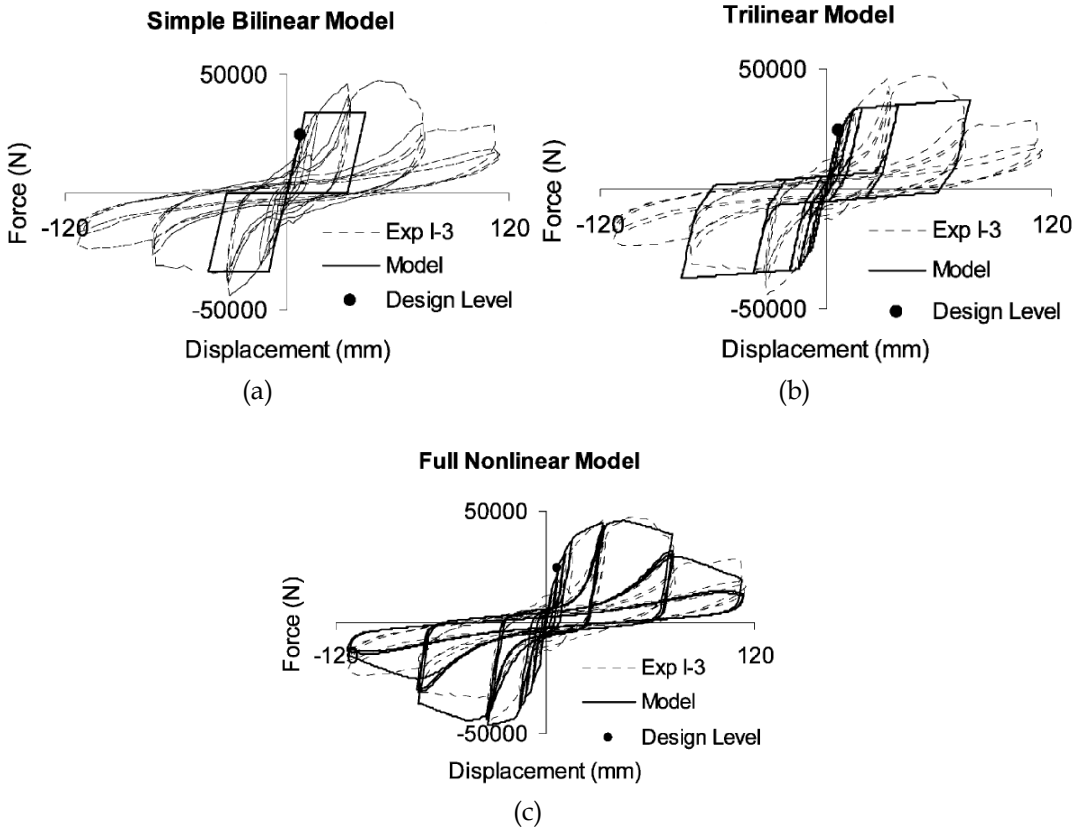

Figure 3.1 – Three models for hysteretic behavior of shear panels (after Fulop and Dubina, 2004)

Also in Folz and Filiatrault (2004) a numerical model is proposed to predict the quasi-static and dynamic behavior of structural wood shear wall panels. The global force-deformation response of the wood shear walls is find to be dominated by the individual sheathing-to-framing connectors used in the wall construction. Therefore, the Authors adopt the same hysteretic envelope to model the global cyclic response of the shear wall. A total of 10 parameters are required to define the hysteretic curve. The parameters calibration is possible through cyclic analysis of shear walls performed by using the CASHEW program. With the CASHEW program, a given wall is first subjected to a cycling testing protocol, after which a

fitting procedure extracts the parameters in order to represent the wall response by an equivalent SDOF shear wall spring element. This model, further validated by experimental tests, requires specifications of wall geometry, shear stiffness of the sheathing panels and hysteretic properties of the sheathing-to-framing connections. The hysteretic model is capable of taking into account strength degradation, failure of the wall at a prescribed maximum displacement, strength degradation based on the loading history, and pinching effect.

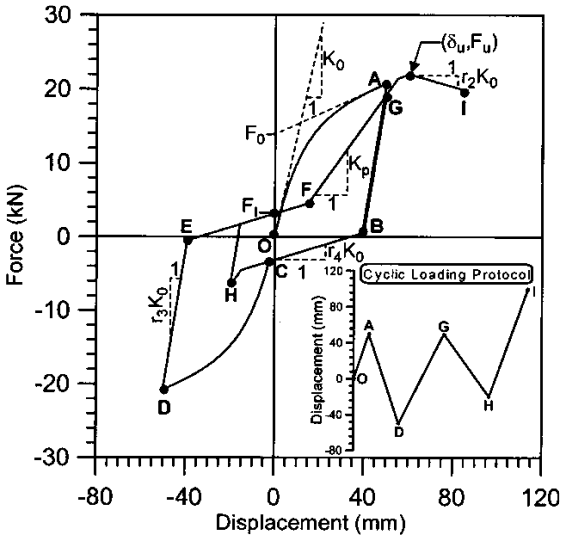

Figure 3.2 – Force-displacement model of wood shear model proposed byFolz and Filiatrault (2004)

In the class of macro-modeling procedure can be included the study of Fiorino et al. (2009), who propose a seismic design method for sheathed cold-formed steel shear walls. Through linear dynamic and nonlinear static procedures, three nomographs are obtained in order to determine the feature of a seismic resistant shear wall. The approach consists in a preliminary definition of the wall geometry and materials, usually deriving from architectural and technological choices or from the design for vertical loads, and a successive evaluation of the sheathing fasteners exterior spacing through linear dynamic (with the''LD''nomograph) or nonlinear static (with the ''NS'' nomograph) seismic analyses. Finally, stud thickness, hold-down anchor diameter, and shear anchor spacing are determined in such way that the ''capacity design'' criteria are satisfied (with the ''OC'' nomograph). A macro-model able to predict the whole pushover response curve of the shear wall is proposed as toll to obtain the design nomographs.

As before mentioned, the previous studies are mainly referred to structural wall system, whose behavior is usually different from nonstructural components, since the latter, by definition of nonstructural, are not intended for lateral load carrying mechanism of the structure. Several works are specifically related to nonstructural components modeling, as listed below. Some of them define macro-modeling procedure, in other studies the modeling process is more detailed, since finite element analysis are conducted.

Telue and Mahendran (2004) conducted experimental studies on cold formed steel walls lined with plasterboard. These studies point out that the studs' compression strength increases when the steel internal frame is covered by plasterboard on one or both sides. A finite element model was developed and validated using experimental results. In the finite element analysis, the studs and plasterboard were modelled as shell elements while the screws were modelled as beam elements along the length of the stud (Figure 3.3). Relevant contact surfaces were successfully included in the model. Appropriate geometric imperfections and residual stresses were also included in the model to obtain accurate results. However, the behavior of the walls is investigated only under compressive vertical loads.

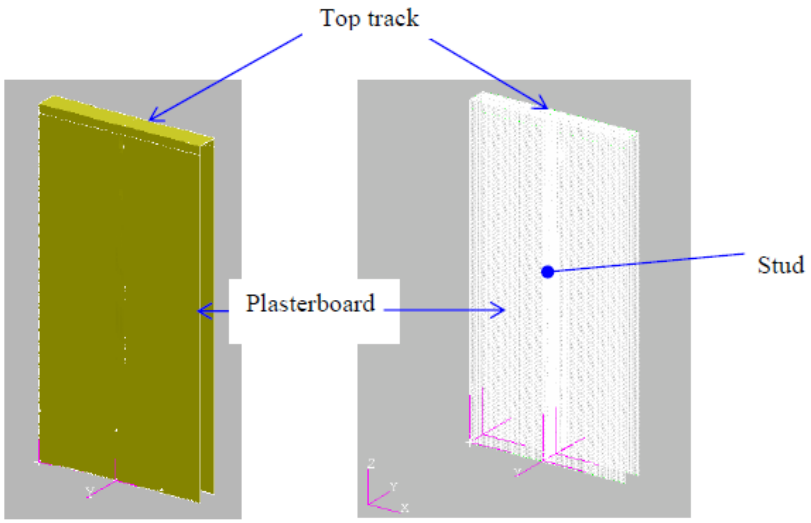

Figure 3.3 – Finite element model of both sides lined frame (after Telue and Mahendran, 2004)

In Kanvinde and Deierlein (2006) a macro-model is presented in order to evaluate the seismic behavior of plasterboard partition. The Authors propose an analytical model to determine the lateral shear strength and initial elastic stiffness

of wood and gypsum wall panels. In such a case, a uniaxial spring model is defined, by a series of parameters defining the backbone curve (Figure 3.4), which represents the nonlinear monotonic response that envelopes the cyclic response, and the cyclic nonlinear response (Figure 3.5) including strength and stiffness degradation and pinching phenomenon. The parameters validations is performed by using experimental tests on full-scale wall panels.

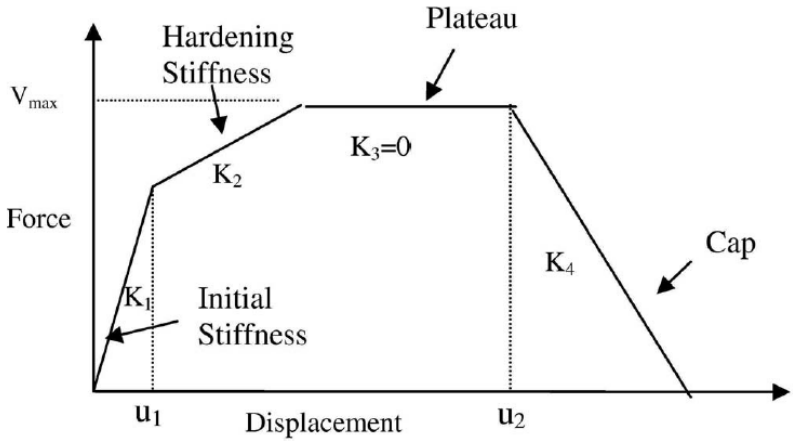

Figure 3.4 – Backbone curve of spring model for plasterboard partition (after Kanvinde and Deierlein, 2006)

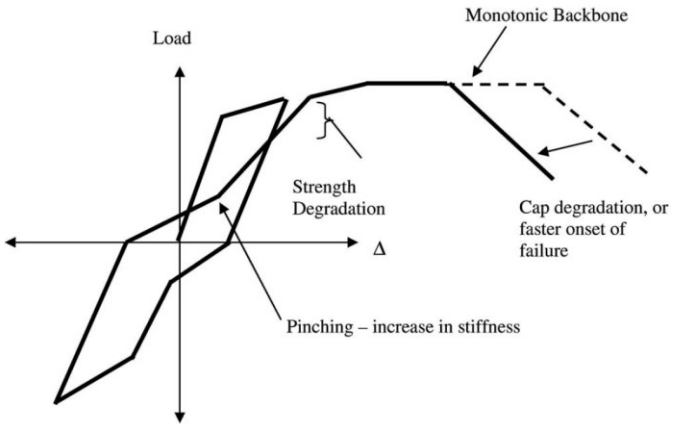

Figure 3.5 – Cyclic hysteretic model for plasterboard partition (after Kanvinde and Deierlein, 2006)

Davies et al. (2011) developed a numerical hysteretic macro-model for the in-plane behavior of partition walls (Figure 3.6). The parameters characterizing the

hysteretic curve are calibrated by using regression analysis to fit the force-displacements curves of 35 wall specimens. These specimens are designed and constructed according to different construction techniques and subjected to both dynamic and quasi-static tests. The parameters necessary for the definition of the hysteric curve are nine, including: initial stiffness, post yield stiffness factor, post capping stiffness factor considering strength degradation, unloading stiffness factor, yield strength, capping strength, intercept strength, reloading or pinch power factor and, finally, softening factor.

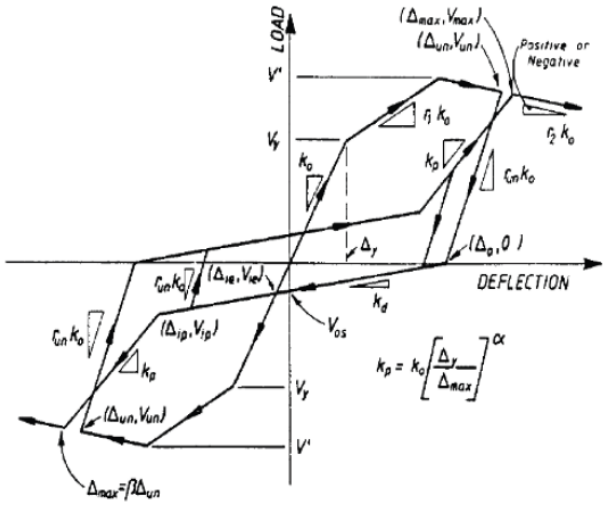

Figure 3.6 – Hysteretic model for plasterboard partition proposed by Davies et al. (2011)

A numerical macro-model for plasterboard partition is also proposed by Wood and Hutchinson, 2012: a pinching material model, available in OpenSees (McKenna and Fenves, 2013), is used in order to reproduce the in-plane behavior of the partitions. The 24 parameters of the model are calibrated by a large number of experimental data obtained from about fifty tests performed on plasterboard partition walls (Retamales et al., 2013). The first 16 parameters describe the force-displacement envelope or backbone of the model, while the remaining eight parameters control the cyclic behavior, i.e. the unloading and reloading behavior.

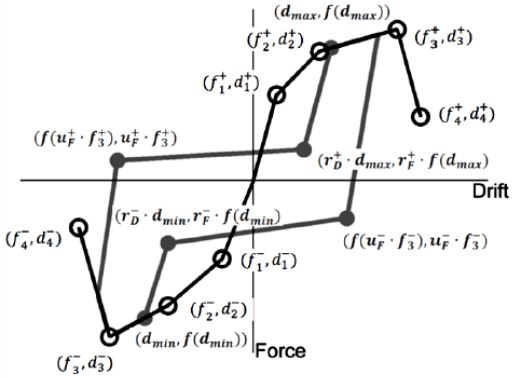

Figure 3.7 – Pinching material model used for modeling plasterboard partition through a single spring (after Wood and Hutchinson, 2012)

3.2 Proposed FEM model for the tested partitions

The previous bibliography review highlights some lacks in the literature about the numerical modeling of plasterboard internal partitions. The numerical models above mentioned focused mainly on steel stud shear walls, which are conceived as structural component, i.e. capable of supporting lateral load like wind or earthquakes and whose characteristics, e.g. stud typology, restraint at the base, failure mode, are usually different if compared to internal partition walls. Also in cases in which nonstructural internal partitions are considered, not always the models are conceived for seismic loads (Telue and Mahendran, 2004) or , in other cases, it is not possible to take into account the different parameters that influence the seismic behavior of the component (Kanvinde and Deierlein, 2006).

Hence, the development of a FEM numerical model of nonstructural component, herein dealt with, would allow to investigate the seismic behavior of a generic partition, taking into account all its features, e.g. studs geometrical and mechanical properties, layer of plasterboards, etc.

The proposed model for the tested partitions (see Chapter 2), is defined in order to investigate the in-plane behavior of such components through the analytical method. SAP2000 (CSI Computer & Structures Inc., 2004) program is adopted to perform finite element analyses.

The analytical model is defined as a 2-D plane model, in order to reduce the computational effort. However, this assumption does not jeopardize the results thanks to the symmetry of the system with respect to the plane in which the

partition is modeled. The whole system reflects the geometrical features of the real partitions in terms of width and height, studs spacing, panels dimension and arrangement, panel-to-stud screw connections spacing. The surrounding test frame is also modelled. An example of a complete FEM model in Sap2000 is provided in Figure 3.8.

A 4-hinged steel frame, representative of the steel test setup (Figure 2.2), is modeled by means of two horizontal (HEB280) and two vertical (tubular profile) frame elements. Internal hinges are provided at the end of the beam elements in order to simulate the statically indeterminate scheme. The base horizontal steel beam is externally restrained with several hinges, which fix the base of the specimen.

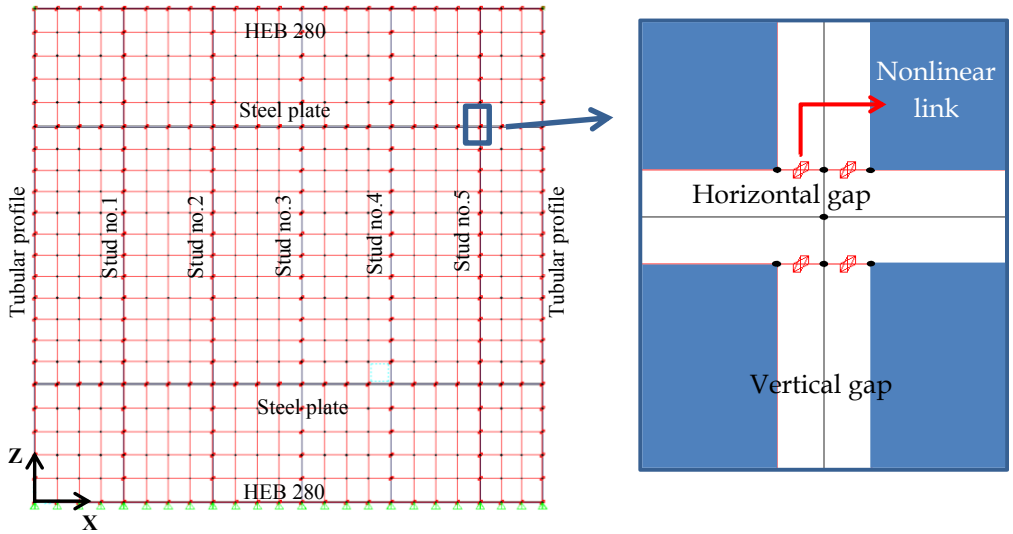

Figure 3.8 – (a) Finite element model of the tested partition in SAP2000 and (b) particular of stud-to-panel connection evidencing the horizontal and the vertical gaps

The studs are modeled by frame elements with C-shaped of I-shaped cross-section, depending on the presence of single or double studs in the partition. The boards, modeled as thin linear shell elements, are arranged in horizontal rows, defining many horizontal joints, as they are in the real specimen. In order to reproduce the actual installation conditions of the boards, horizontal and vertical gaps are included between the plasterboards and the adjacent elements both in the horizontal and in the vertical directions (Figure 3.8b). One layer of plasterboard is considered in the model, whose thickness is equal to the total thickness of the installed boards. The plasterboards are properly meshed with shell elements, whose

dimension depends on the screw spacing: indeed, the mesh allows introducing the panel-to-stud screw connections, according to their actual spacing. The screws, which connect the plasterboard (node *j* in Figure 3.9) either to the stud (node *i* in Figure 3.9) or to the surrounding frame, are modeled as nonlinear springs, i.e. NLLINK objects in SAP2000, whose backbone curve is defined in §3.2.1.2. These links act along the two translational directions in the plane of the partition as evidenced in Figure 3.8. A single link is representative of the behavior of two screws, which connect the plasterboard layers of each side of the partition either to the stud or to the surrounding frame.

In case of steel plates presence (Figure 2.3b) - an example is provided by the specimen P-3 of Table 2.1 - they are placed at the horizontal joints between the plasterboard panels. Horizontal frames between two consecutive studs model them; internal hinges are placed at the end of each frame in order to reproduce the actual constraint given by a single screw. Each plasterboard is connected to the steel plate through several equally spaced screws. The steel studs are only connected to the plasterboards through the nonlinear links. They are not connected to the steel setup, both at the base and at the top.

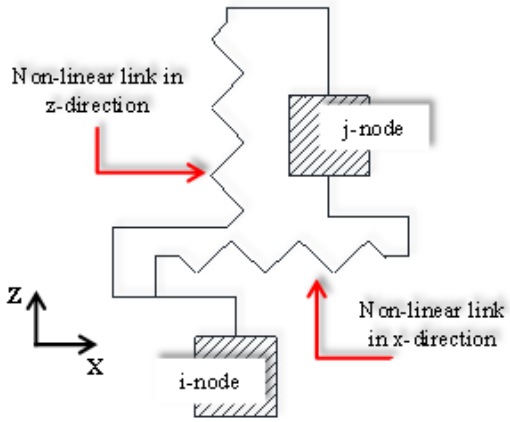

Figure 3.9. Stud-to-panel screw connection scheme.

The mechanical properties of the steel material adopted for the studs, the horizontal plates and test frame are listed in Table 3.1; the mechanical properties of the gypsum wallboard are listed in Table 3.2 and Table 3.3. Such properties are evaluated through experimental tests on both the steel studs and the gypsum boards used for the tested specimen, here omitted for the sake of brevity. Both the gypsum and the steel materials are modelled with a linear elastic material. The low stress level in the boards justifies such an assumption, as evidenced in §3.3;

moreover, a linear behavior of the stud can be assumed up to failure, since the collapse mechanism is governed by the elastic buckling failure.

Material	Tensile strenght *[Mpa]*	Young's Modulus *[Mpa]*
Steel	301	210000

Table 3.1 – Steel mechanical properties, based on experimental test

Type of board	Young modulus *[Mpa]*	Compressive strength *[Mpa]*
BA18S	3394	7.6
BA18	2659	5.2
BA13	1888	3.2
BA13 Pregyflam	2965	5.4
BA15 Pregyflam	3383	6.4

Table 3.2 – Gypsum wallboard mechanical properties in compression, based on experimental test

Type of board	Young modulus *[Mpa]*	Tensile strength *[Mpa]*
BA18S	3811	1.3
BA18	3808	1.1
BA13	1885	1.3
BA13 Pregyflam	3041	1.6
BA15 Pregyflam	4536	1.4

Table 3.3 - Gypsum wallboard mechanical properties in tension, based on experimental test

The presence of the paper and the compound between adjacent plasterboards is neglected in the model, in a first stage of the modelling procedure. This choice is performed both in order to reduce the computational effort and define a simple model. It should not influence the evaluation of the inter-story drift that causes the collapse of the partition. Indeed, the paper and the compound typically crack at low inter-story drift demand level, much earlier than the partition collapse.

Finally, it should be noted that, despite the large number of elements, the model of the partition is quite simple. The nonlinearity is lumped in the panel-to-stud

screwed connections; this is widely supported by the experimental evidence that showed severely damaged screwed connections before the partition failure. The occurrence of the failure mechanism, due to the buckling of the partition, is a-posteriori checked; it is based on the internal forces acting on the stud for a given level of displacement demand (see §3.3.1).

3.2.1 Nonlinear link modeling panel-to-stud screwed connections

The calibration of the NNLINK mechanical behavior is conducted according to the results of several experimental tests performed on the screwed connections systems, adopted in the considered partitions. On the base of the experimental force-displacement curves, a trilinear curve is drawn for each connection system, as explained below.

3.2.1.1 Experimental data

The experimental campaign is conducted in the laboratory of the Siniat International S.p.a. The test setup is schematically shown in Figure 3.10: two back-to-back studs are connected to a single (or a double) plasterboards layer through two screws or (four screws) for each side. The self-drilling screws are characterized by a 3.5 mm diameter and a 35 mm length. The screws strength is evaluated in terms of Rockwell hardness, whose value is around 44.

Two pieces of wood are placed inside the stud (Figure 3.11a) to avoid the local crushing of the steel stud at the contact interface with compression plate. Moreover, in order to uniformly transfer the load to the specimen, a teflon plate is screwed in the wooden pieces.

The load is applied on the top of the system in a monotonic way up to the specimen failure with a 2mm/min rate; two displacement transducers (see Figure 3.11b) are placed on each side of the stud in order to record the screw-to-board relative displacement. A global view of the test setup is shown in Figure 3.11c.

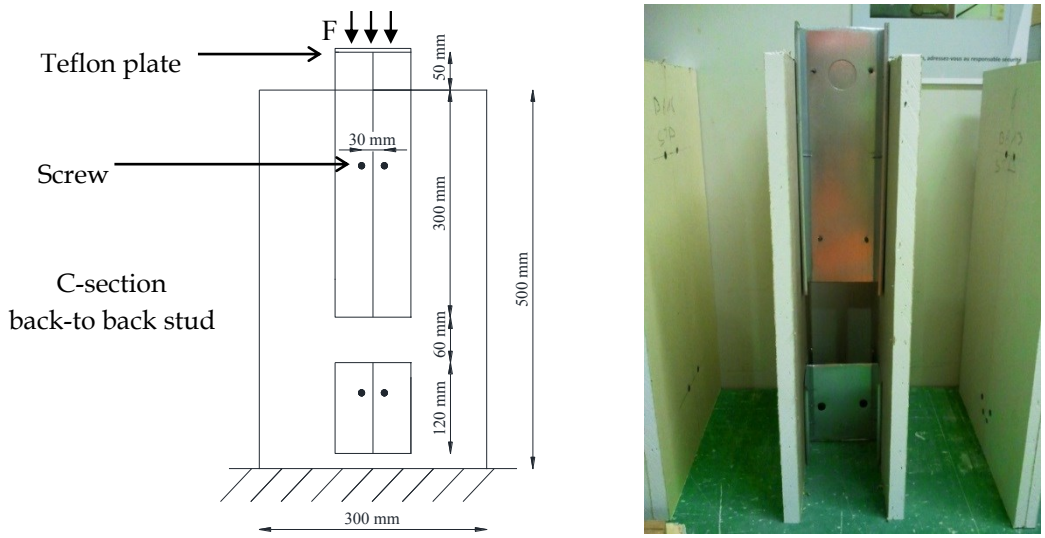

Figure 3.10 - (a) Schematic view of the tested specimen dimensions (in mm) and (b) assembled specimen before testing.

Figure 3.11 - (a) Particular of wood pieces and Teflon plate, (b) displacement transducers position and (c) whole test setup view

In case that the partition provides a double layer of plasterboards for each side, two configurations of connection are investigated, as shown in Figure 3.12. Indeed, the vertical screws spacing in the inner layer is usually double than the outer one. So, since the plane model of the partition provides just one plasterboard layer, the links are assigned with a constant spacing, i.e. equal to the external one, by alternating configuration 1 (Figure 3.12a) and configuration 2 (Figure 3.12b).

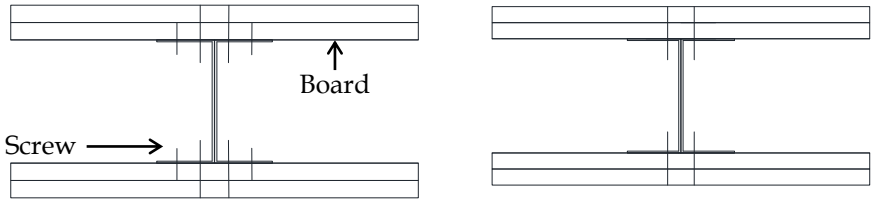

Figure 3.12 – (a) Configuration 1 of the panel-to-stud connection providing 4 screws for each side of the partition and (b) configuration 2 providing two screw for each partition side

In Table 3.4 are listed all the panel-to-stud screwed connections tested, evidencing the board typology, the board thickness and the number of layer, since the screws and the stud typology are always the same. The first connection system provides one layer of BA18S board for each partition side, so one configuration is tested, i.e. with two screws for each side (see Figure 3.12b). For the other connections systems, in which two layer of boards are screwed to the studs, both configuration 1 and configuration 2 are subjected to experimental test.

Type of board	Thickness	Number of layer	Configuration tested	
	[mm]	*[-]*	**1**	**2**
BA18S	18	1		✓
BA18	18	2	✓	✓
BA13	12,5	2	✓	✓
BA13 Pregyflam	12,5	2	✓	✓
BA15 Pregyflam	15	2	✓	✓

Table 3.4 – List of the panel-to-stud screwed connections tested

The following figures show the experimental backbone curve achieved from the tests. It should be noted that both for BA13 (Figure 3.14) and BA18 (Figure 3.15) plasterboard the maximum strength in configuration 1, providing 4 screws for each partition side, is almost twice the maximum strength in configuration 2, where the board are connected to the stud by two screws per side.

Three tests are performed for *Pregyflam* boards for each configuration, for both BA13 (Figure 3.16) and BA15 (Figure 3.17). The maximum strength achieved when four screws per side are used, in this case, is not twice the maximum strength in configuration 2, providing two screws connecting the board to the stud.

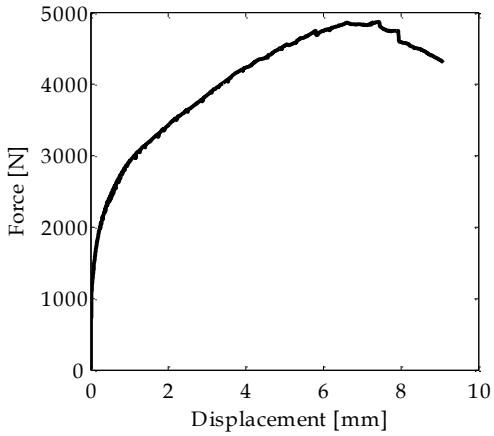

Figure 3.13 – Force – displacement curve of panel-to-stud connection for BA18S plasterboard panel

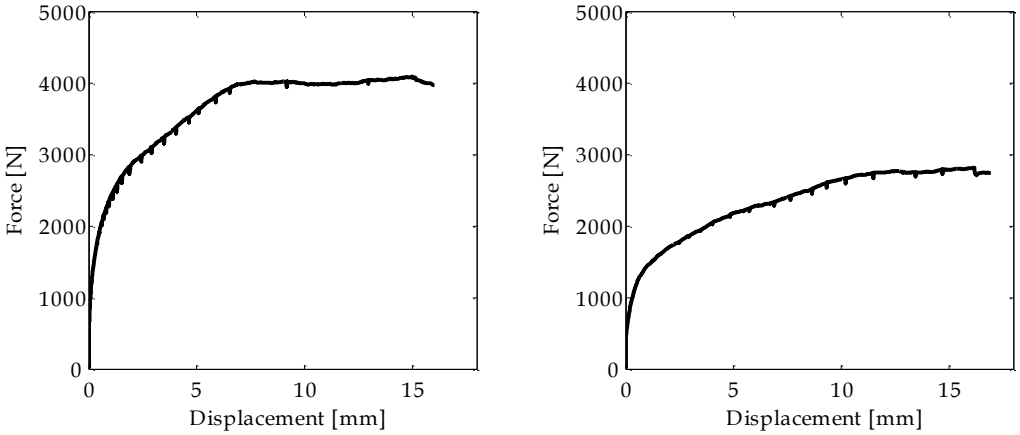

Figure 3.14 - Force – displacement curve of panel-to-stud connection for BA13 plasterboard panel in (a) configuration 1 and (b) configuration 2

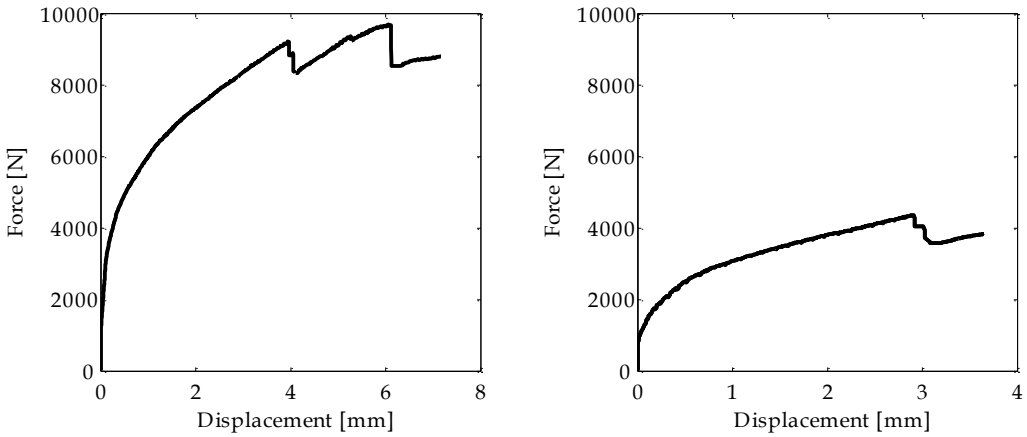

Figure 3.15 - Force – displacement curve of panel-to-stud connection for BA18 plasterboard panel in (a) configuration 1 and (b) configuration 2

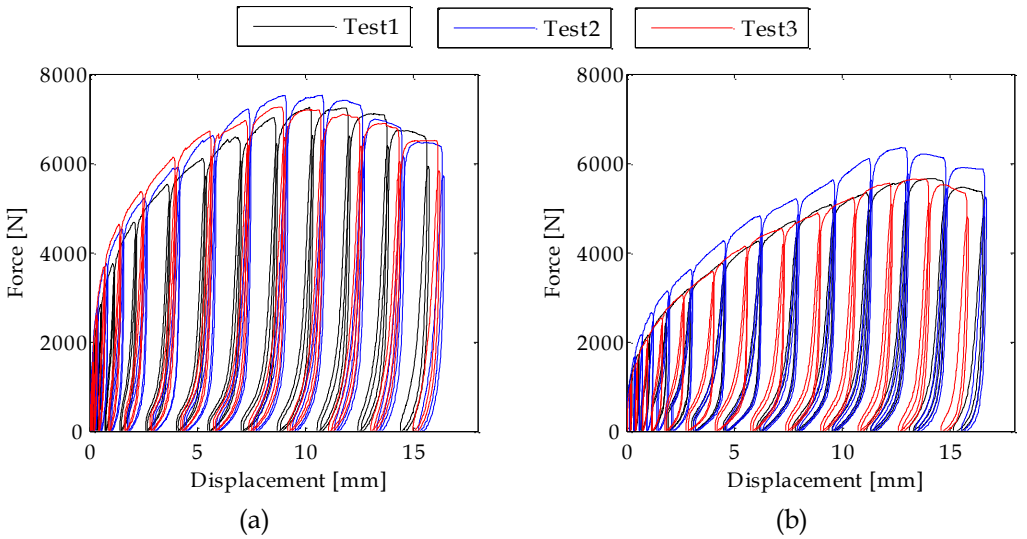

Figure 3.16 – Force-displacement curve of panel-to stud connection for BA13 Pregyflam plasterboard panel in (a) configuration 1 and (b) configuration 2

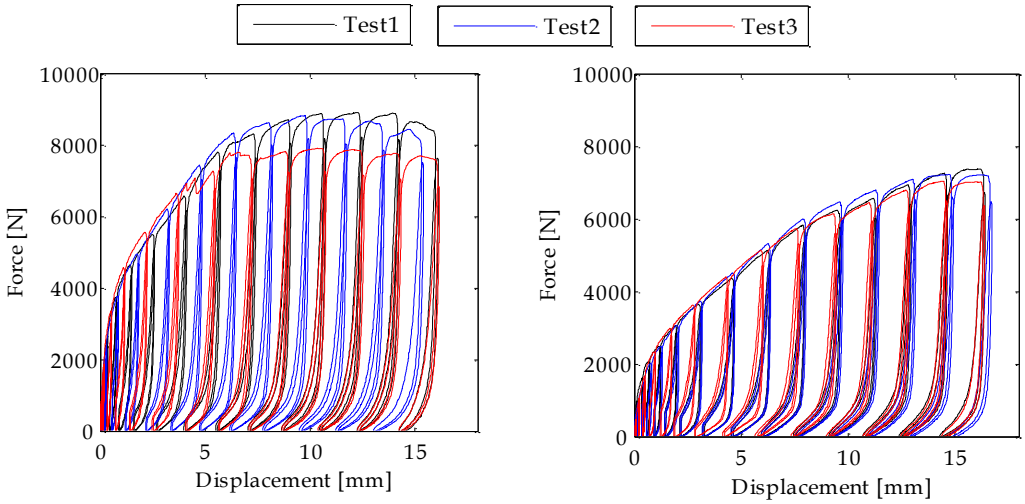

Figure 3.17 - Force-displacement curve of panel-to stud connection for BA15 Pregyflam plasterboard panel in (a) configuration 1 and (b) configuration 2

The tests herein presented cover all the possible panel-to-stud screwed configurations of the tested partitions, shown in Table 2.1.

3.2.1.2 Calibration of the screwed connection backbone curve

In order to include the actual behavior of the panel-to-stud screwed connections in the plane model of the partitions, a tri-linear fitting curve is assigned to NLLINK spring in SAP2000. Four specific points define the tri-linear envelope, depicted schematically in Figure 3.18, where:

- F_{max} is the maximum force reached during the experimental test and d_{max} is the corresponding displacement;
- F_u and d_u are the ultimate force and displacement reached at the specimen failure, respectively;
- F_y value is obtained by imposing two conditions: (a) the initial stiffness k, i.e. the slope of the first branch of the tri-linear curve, is evaluated according to Schafer (2013) as:

$$k = \frac{0.4F_{max}}{d_{0.4}} \tag{3.1}$$

in which $d_{0.4}$ is the displacement value that corresponds to 0.4 F_{max} force; (b) the dissipated energy up to F_{max} is the same both in the experimental and in the numerical force-displacement curve.

The yielding displacement d_y can be clearly evaluated as follows:

$$d_y = \frac{F_y}{k} \tag{3.2}$$

The third branch of the envelope is simply obtained assuming a linear envelope from the capping point, i.e. the point characterized by the maximum force F_{max}, to the ultimate point.

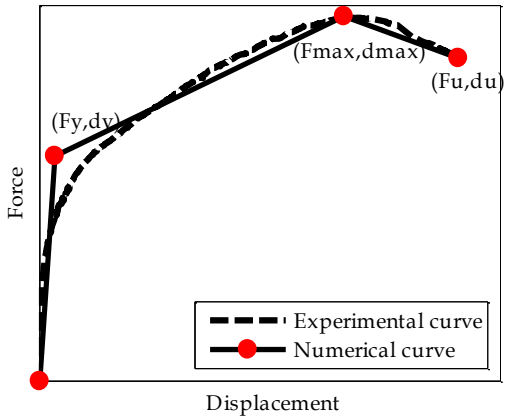

Figure 3.18. Experimental and tri-linear backbone curves of the screws connection

In Figure 3.19, Figure 3.20 and Figure 3.21 are shown the trilinear envelopes (red lines) for BA18S, BA13 and BA18 plasterboard respectively, obtained according the above mentioned procedure. Figure 3.22 and Figure 3.23 illustrate the trilinear envelope (red curves) of screwed connection for Pregyflam boards. The black line of each graph in Figure 3.22 and Figure 3.23 represents the mean curve of the envelop of the maxima of the loading-unloading curves of Figure 3.16 and Figure 3.17.

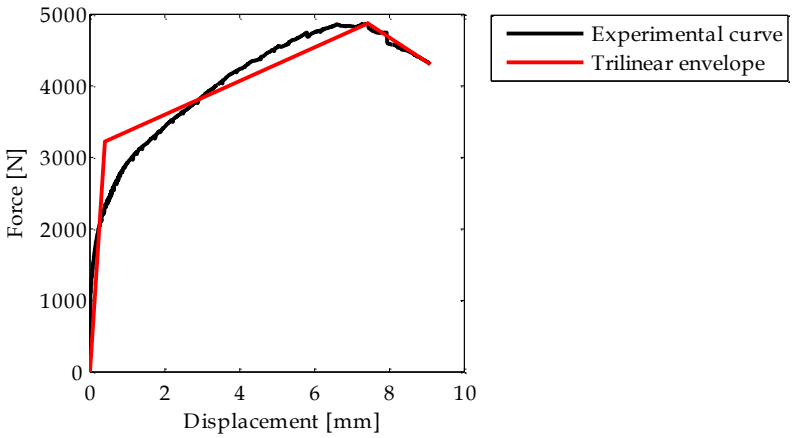

Figure 3.19 – Trilinear envelope of the backbone curve for BA18S screwed connection

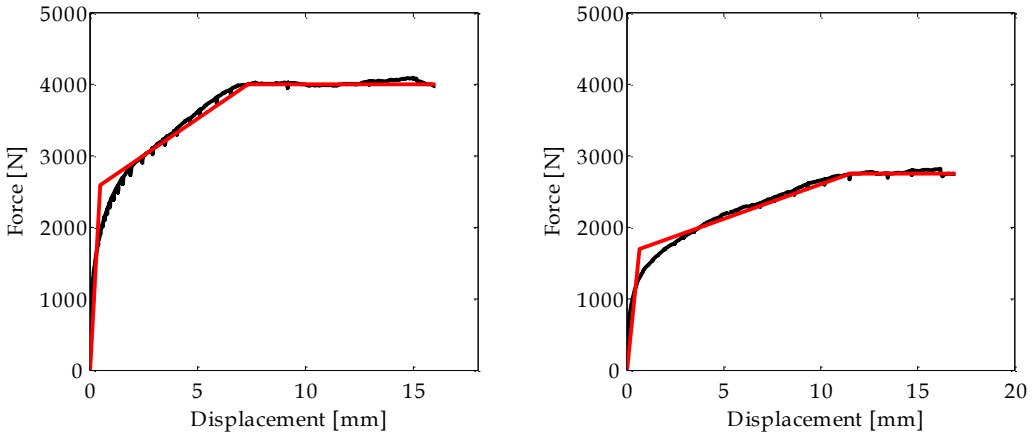

Figure 3.20 - Trilinear envelope of the backbone curve for BA13 screwed connection in (a) configuration 1 and (b) configuration 2

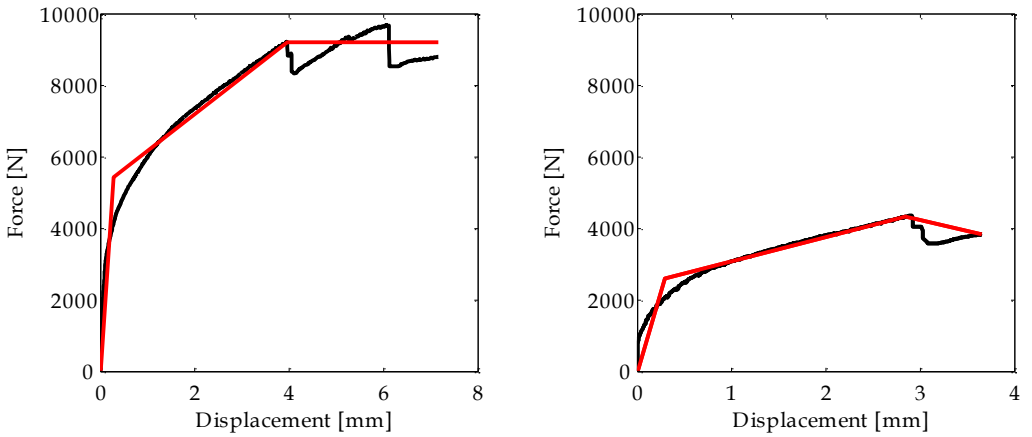

Figure 3.21 - Trilinear envelope of the backbone curve for BA18 screwed connection in (a) configuration 1 and (b) configuration 2

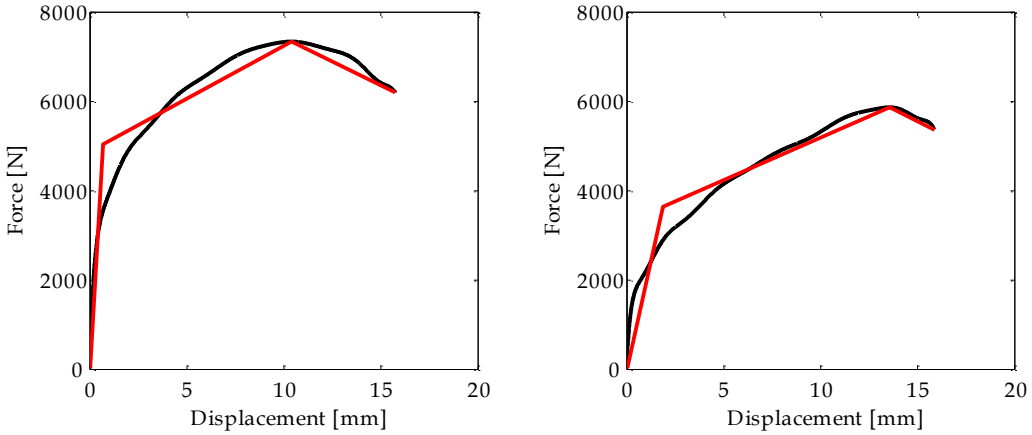

Figure 3.22 - Trilinear envelope of the backbone curve for BA13 Pregyflam screwed connection in (a) configuration 1 and (b) configuration 2

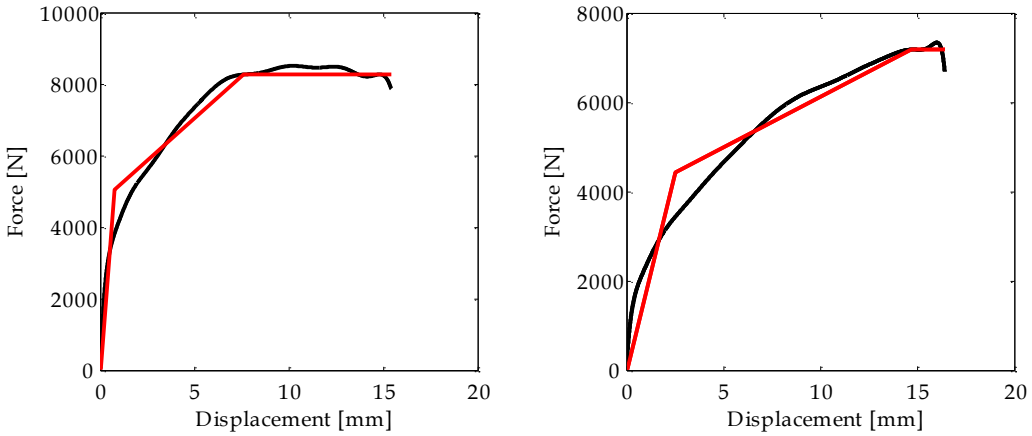

Figure 3.23 - Trilinear envelope of the backbone curve for BA15 Pregyflam screwed connection in (a) configuration 1 and (b) configuration 2

It should be noted that the forces assigned to the connections in the partition model are obtained scaling down the forces by a factor of two, since the tri-linear curve in Figure 3.18 is representative of the behavior of four screws whereas the nonlinear spring included in the model corresponds to two screws.

3.3 Numerical – experimental comparison for FEM model validation

The analytical models (shown in Figure A. 1, Figure A. 5, Figure A. 9 and Figure A. 13 of the Appendix) of the four tested specimens described in the Chapter 2 (P-1, P-2 P-3 and P-4 of Table 2.1) are subjected to a large-displacement nonlinear static analysis in displacement control through the SAP2000 program (CSI Computer & Structures Inc., 2004). A monotonic load is applied to the model, since the nonlinear behavior of the partitions is lumped in the panel-to-stud screwed connections and only the monotonic experimental curve is available for these connection systems. The top displacement is applied in consecutive steps reaching a 100 mm maximum displacement, i.e. 2.0% inter-story drift.

The force applied to the partition top is transferred to the base through the plasterboard panels. In Figure 3.24, referred to the partition P-3, the stress trends highlight that the compression stresses in the plasterboards are concentrated in a diagonal strut, i.e. from the top left to the bottom right of each panel. The maximum stress values are close to 1.0 MPa at the final step of the analysis, i.e. corresponding to the 2.00% partition drift. In Figure 3.25 tensile diagonal strut is visible in each plasterboard panel from the bottom left to the top right, the maximum tension stress value is about 0.9 MPa. Similar stress trend and stress value are recorded also for specimen P-1, P-2 and P-4, as shown in the Appendix. The low level of stresses justifies the modeling of the gypsum material with a linear elastic behavior (§3.2).

In turn, the panels transfer the load to the studs through the screws; the studs are therefore subjected to both bending moment and compression axial force. The studs compression recorded in the FEM models is confirmed by the local plastic deformation in the studs of the tested partitions, due to the contact at their base with the base horizontal guide, as shown in Figure 3.26.

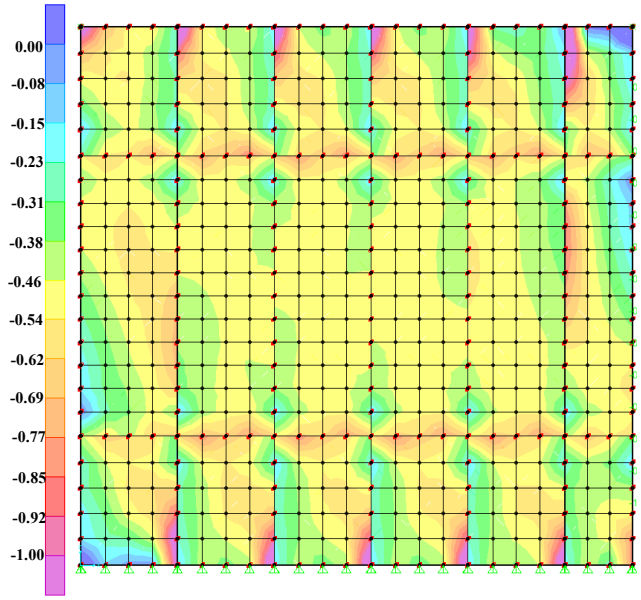

Figure 3.24. Compression stresses (in MPa) diagram on plasterboards of specimen P-3 at last step of the analysis

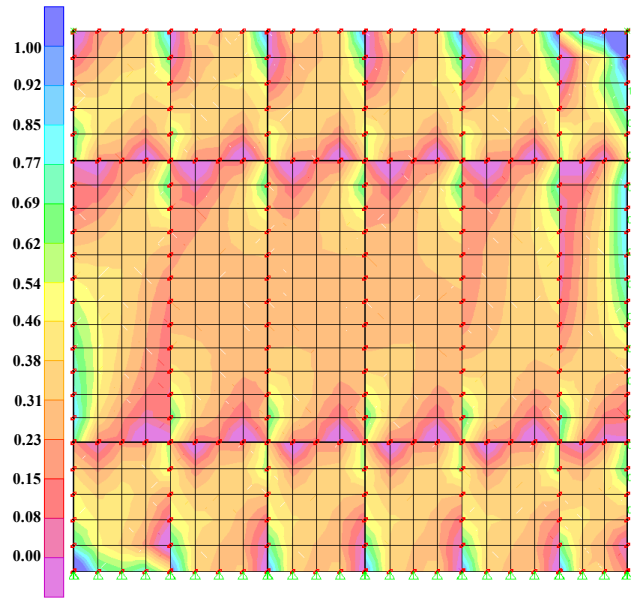

Figure 3.25 - Tension stresses (in MPa) diagram on plasterboards of specimen P-3 at last step of the analysis

Figure 3.26. Stud damage due to compression at the partition bottom.

The bending moment diagram on studs reveals a concentration of stress values crossing the horizontal joints red circled in Figure 3.27a. In these zones the high stress values can justify the concentration of damage, which is experimentally pointed out exactly over and under the horizontal joints (Figure 3.27b). Even if the Figure 3.27 is specifically referred to the P-3 specimen FEM model, similar considerations can be drown for the other specimen models, i.e. P-1, P-2 and P-4 (see Figure A. 2, Figure A. 6 and Figure A. 14 of the Appendix).

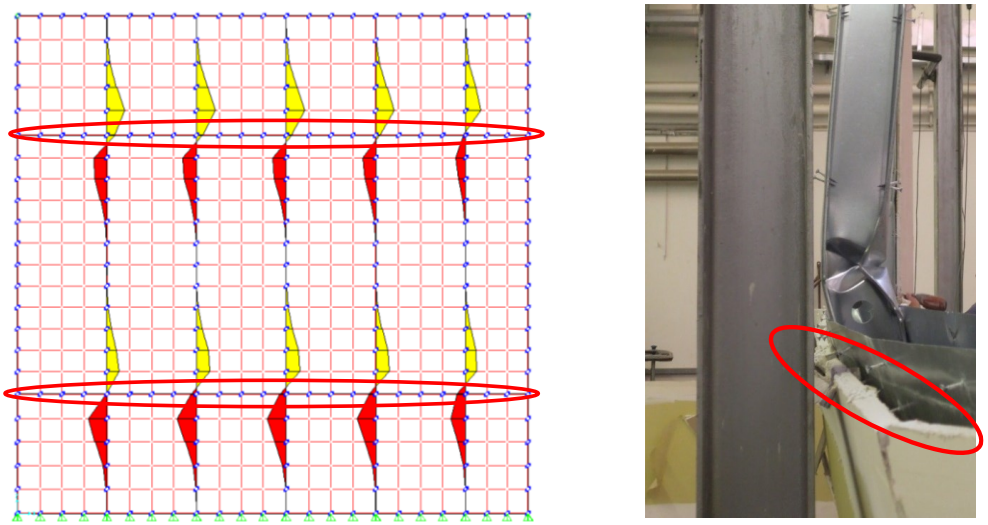

(a) (b)

Figure 3.27. (a) Bending moment diagram on studs of P-3 specimen at the last step analysis crossing horizontal joints (in red circles) and (b) observed damage on stud below the horizontal joint (red circled).

Furthermore, the numerical deformed shape (Figure 3.28a) points out a relative displacement between plasterboard, evidenced also in the experimental test on the partition (Figure 3.28b)

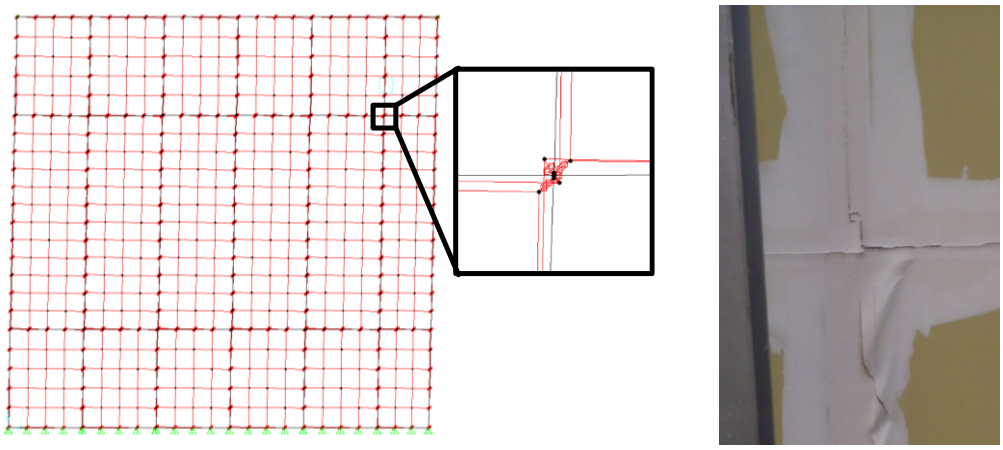

(a) (b)

Figure 3.28. (a) Deformed shape of the analytical model and (b) particular of the board overlap in the corner.

The results of the performed analysis are remarkable since the behavior of the analytical model seems to reproduce quite accurately the experimental evidence.

3.3.1 The Direct Strength Method applied to the modeled partitions

The occurrence of the partition buckling is assessed according to the Direct Strength Method (DSM) proposed by Schafer (2013). This method, developed to design cold-formed steel stud walls covered by panels connected to the stud, is herein employed as a-posteriori checking method of the modeled partitions. Indeed, the tested system investigated in this work can be included in the structural system typology studied by Schafer.

The DSM stems from a long-term project with the aim of developing a reliable method for the design of cold-formed steel stud wall whose behavior is influenced by the buckling of the studs, when subject to compression and/or bending moment.

The DSM provides three different buckling failure modes of the cold-formed steel elements:

- local buckling that involves a distortion of a portion of the cross-section. The half-wavelength of the local buckling mode is less than or equal to the largest characteristic dimension of the compression member of the cross section (Figure 3.29a);

- distortional buckling (Figure 3.29b) that produces a significant distortion of the cross-section: usually the flanges buckle presenting relative rotation with respect to the undeformed condition of the web, i.e. the section tends to "open" or to "close". The half-wavelength of distortional buckling is usually included between the local and the global buckling half-wavelength ;
- global buckling, or “Euler” buckling, that involves the translation and/or the rotation of the entire cross-section (Figure 3.29c). Both the stud length and its restraint condition determine the half-wavelength characterizing the global buckling of the stud.

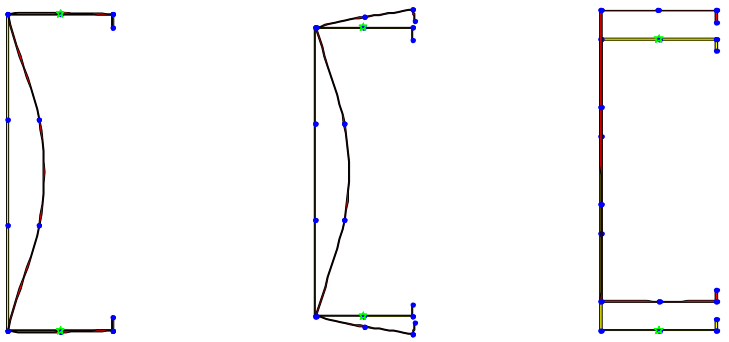

(a) (b) (c)

Figure 3.29. Three different buckling failure modes: (a) local buckling, (b) distortional buckling and (c) global buckling.

A series of experimental tests (Vieira and Schafer, 2010) on covered studs prove that the occurrence of the stud buckling is influenced: (a) by the mechanical and geometrical characteristics of the studs, (b) by the sheathing system and (c) the board-to-stud connections, that provide a bracing restraint to the stud. The influence of the panels and the panel-to-stud connections are modelled through elastic springs that restraint the steel stud. Three different springs, i.e. two translational ones and a rotational one, are introduced at the fastener location (Figure 3.30).

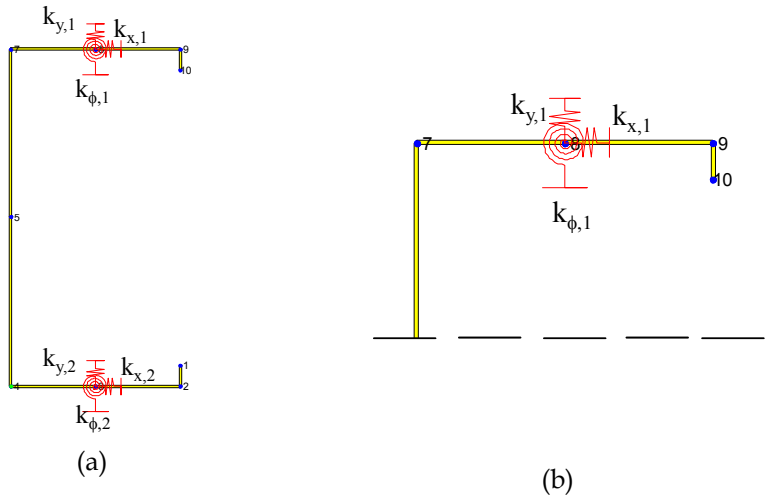

Figure 3.30. Model of the stud in the DSM method: (a) stud section with springs at two sides and (b) details of the springs.

The stiffness values (k_x, k_y and k_ϕ) can be evaluated through closed-form formulas provided byVieira and Schafer (2010), even if an experimental evaluation is preferred.

The "k_x" spring represents the contribution of the boards to the in-plane lateral stiffness, taking into account the diaphragm effect of the boards (k_{xd}) and the shear stiffness of the screwed connections (k_{xl}) (Vieira and Schafer, 2012). This stiffness can be evaluated according to the formula(3.3), developed by the plane model of Figure 3.31.

$$k_x = \frac{1}{\frac{1}{k_{xl}} + \frac{1}{k_{xd}}} \tag{3.3}$$

where:

$$k_{xl} = \frac{P}{\delta} = \frac{3 \cdot p \cdot E \cdot d^4 \cdot t^3}{4 \cdot t_b^2 \cdot (9 \cdot p \cdot d^4 + 16 \cdot t_b \cdot t^3)} \tag{3.4}$$

with:

- E: Young's modulus of steel stud;
- I: inertia modulus of steel stud;
- t_b: board thickness;
- d: screws diameter;

$$k_{xd} = \left(\frac{2 \cdot \pi \cdot \mathrm{G} \cdot \mathrm{b} \cdot \mathrm{t}}{\mathrm{L_n}} \right) * \sin\left(\frac{\pi d_f}{2 \cdot \mathrm{L}}\right) \cong (\pi^2 \cdot G_b \cdot t_b \cdot d_f \cdot w_{tf}) / L^2 \qquad (3.5)$$

with:

- G: shear modulus of the plasterboard;
- b: board width;
- L: board height;
- d_f: vertical screws spacing;
- n: studs number;

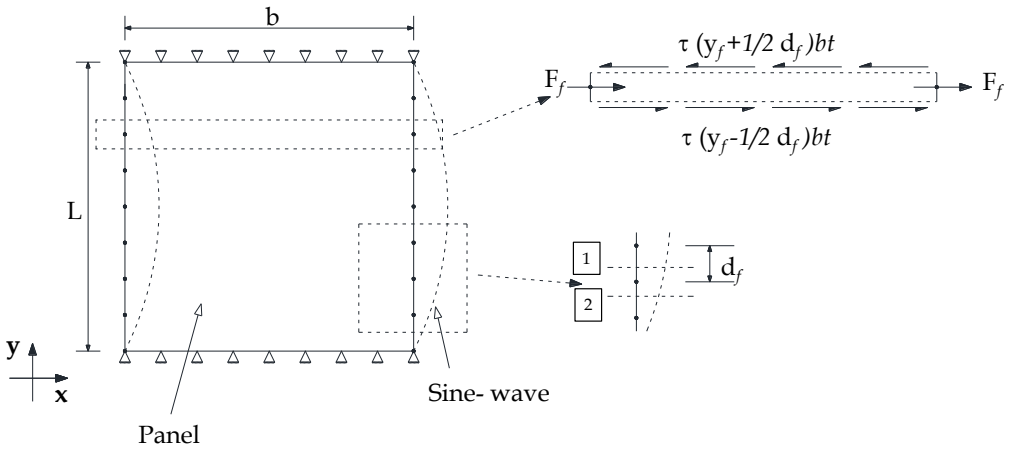

Figure 3.31 – Plane model used in lateral stiffness, k_x, evaluating (from Vieira and Schafer, 2013)

For the analytical model herein presented, the shear stiffness of the connection, i.e. the k_{xl} contribution, is evaluated upon the experimental tests, detailed in §3.2.1. In particular, the k_{xl} corresponds to the backbone initial stiffness defined in §3.2.1.2. The "k_y" is representative of the out of plane stiffness that develops from the sheathing under major-axis bending (see Figure 3.32) and can be evaluated as follow (3.6):

$$k_y = \frac{(EI)_w \cdot \pi^4 \cdot d_f}{L^4} \qquad (3.6)$$

where:

- d_f :vertical screws spacing;
- L: partition height;
- EI_w: supplementary stiffness provided by the plasterboard.

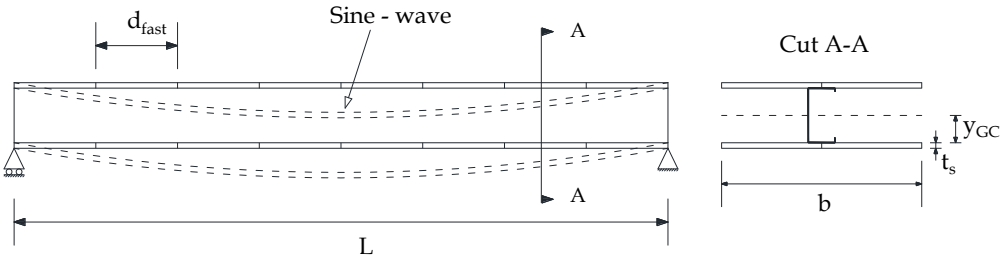

Figure 3.32 - Analytical model for the out of plane stiffness, k_y, evaluation (after Vieira and Schafer, 2013)

The "k_ϕ" spring is representative of the rotational restraint given by the presence of the panel. This contribute is evaluated by the equation (3.7), concerning the scheme of Figure 3.33.

$$k_\varphi = k_{\varphi 1} \cdot d_f \tag{3.7}$$

being:

$$k_{\varphi 1} = \frac{1}{\frac{1}{k_{\varphi w}} + \frac{1}{k_{\varphi c}}} \tag{3.8}$$

Where, $k_{\phi w}$ represents the board rotational stiffness and can be evaluated as provided by (3.9):

$$k_{\phi w} = \frac{EI_w}{L} \tag{3.9}$$

with:

- EI_w: supplementary stiffness provided by the plasterboard;
- L: partition height.

The screw rotational stiffness values, $k_{\phi c,}$ are listed in tables provided in Schafer (2013).

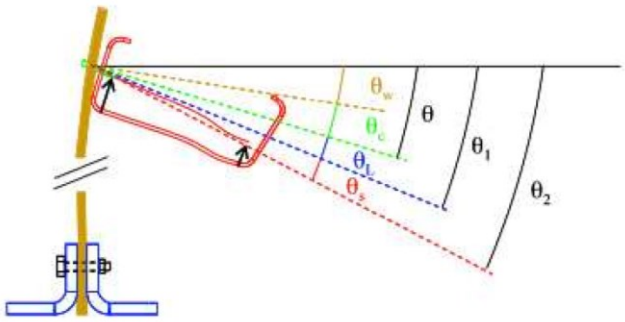

Figure 3.33 – Considered scheme for rotational stiffness, k_ϕ, contribution (after Schafer et al., 2009)

The application of the DSM method consists in determining the axial forces and bending moments that produce the instability of the stud covered by boards. The nominal axial (P_n) and flexural (M_n) strength of the stud can be assessed by using the expressions provided by AISI-S100 (2007). In particular, three resisting axial force and bending moment values are defined, i.e. one for each instability failure mode. The nominal global (or *Eulerian*) axial strength is provided by (3.10) or (3.11):

$$P_{ne} = 0.658^{\lambda^2} P_y \qquad \text{if } \lambda_e < 1.5 \tag{3.10}$$

$$P_{ne} = 0.877 P_y \qquad \text{if } \lambda_e \geq 1.5 \tag{3.11}$$

The nominal local axial strength is evaluated according to (3.12) or (3.13):

$$P_{nl} = P_{ne} \qquad \text{if } \lambda_l < 0.766 \tag{3.12}$$

$$P_{nl} = \left[1 - 0.15\left(\frac{P_{crl}}{P_{ne}}\right)^{0.4}\right]\left(\frac{P_{crl}}{P_{ne}}\right)^{0.4} P_{ne} \qquad \text{if } \lambda_l \geq 0.766 \tag{3.13}$$

Finally the nominal distortional strength is evaluated as reported in (3.14) or (3.15):

$$P_{nd} = P_y \qquad \text{if } \lambda_d < 0.0561 \tag{3.14}$$

$$P_{nd} = \left[1 - 0.25\left(\frac{P_{crd}}{P_y}\right)^{0.6}\right]\left(\frac{P_{crd}}{P_y}\right)^{0.6} P_y \quad \text{if } \lambda_d \geq 0.0561 \tag{3.15}$$

Also for the bending moment strengths, the DSM provides similar formulations. The nominal global bending strength is equal to (3.16):

$$M_{ne} = M_y \tag{3.16}$$

The nominal local bending strength can be evaluated as follow (3.17) or (3.18):

$$M_{nl} = M_{ne} \qquad \text{if } \lambda_l < 0.766 \tag{3.17}$$

$$M_{nl} = \left[1 - 0.15\left(\frac{M_{crl}}{M_{ne}}\right)^{0.4}\right]\left(\frac{M_{crl}}{M_{ne}}\right)^{0.4} M_{ne} \quad \text{if } \lambda_l \geq 0.766 \tag{3.18}$$

The nominal distortional bending strength is evaluated according to (3.19) or (3.20):

$$M_{nd} = M_y \qquad \text{if } \lambda_d < 0.673 \tag{3.19}$$

$$M_{nd} = \left[1 - 0.22\left(\frac{M_{crd}}{M_y}\right)^{0.5}\right]\left(\frac{M_{crd}}{M_y}\right)^{0.5} M_y \quad \text{if } \lambda_d \geq 0.673 \tag{3.20}$$

In the previous formulations, the λ factors represent the instability multipliers, or *load factors,* which are evaluated through the CUFSM software (Schafer, 2012). This software is an open source (http://www.ce.jhu.edu/bschafer/cufsm/) finite strip elastic stability analysis program, which allows the identification of the buckling modes of cold-formed steel members (Adany and Schafer, 2006). Modelling the stud cross section, in terms of geometrical and mechanical features, complete of translational and rotational springs (see Figure 3.34), in the CUFSM software, λ_e, λ_l and λ_d factors can be evaluated, for both axial force and bending moment.

Knowing the load factor, and consequently the local, the global and the distortional strengths, in terms of axial force and bending moment, the DSM allows

the design of the cold formed steel stud, by defining the design axial force, P_n and the design bending moment, M_n according to (3.21) and (3.22) :

$$P_n = \min(P_{ne}, P_{nl}, P_{\mathrm{nd}}) \tag{3.21}$$

$$M_n = \min(M_{ne}, M_{nl}, M_{\mathrm{nd}}) \tag{3.22}$$

A design domain can therefore be drawn, as show in Figure 3.35.

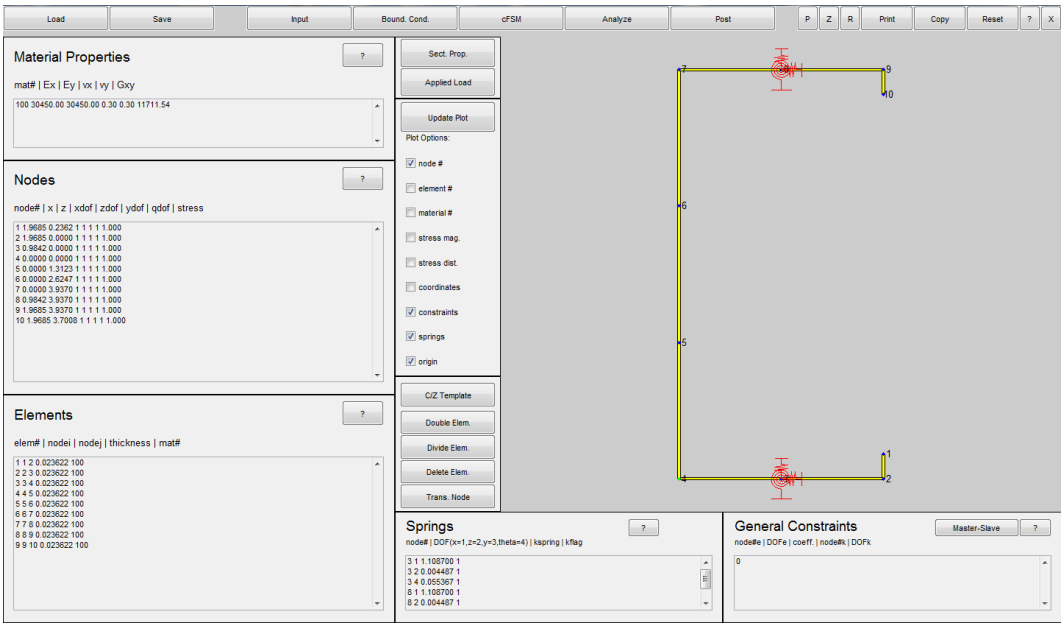

Figure 3.34 – Main screen of CUFSM software for input data of covered stud

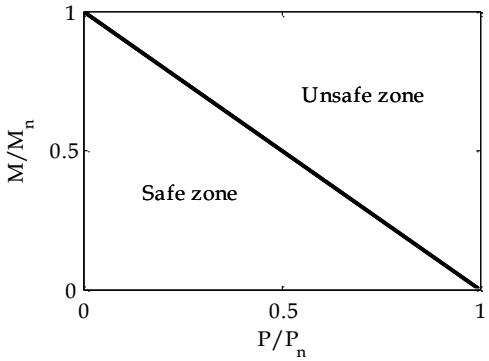

Figure 3.35 – Axial force – bending moment design domain for cold formed steel stud

Since the aim of this work is to define a suitable analytical model of steel stud sheathed partitions in order to verify the seismic behavior of such components, the

DSM is used as a-posteriori checking method. A domain for each buckling mode is defined (Figure 3.36) to check its occurrence for a given level of displacement demand. Therefore, the internal forces acting on the studs, in terms of axial force and bending moment resulting from the FEM analysis are compared to the limit curves.

In Figure 3.37, Figure 3.38, Figure 3.39 and Figure 3.40 the buckling occurrence is checked for the four tested partitions. The local and the distortional domain are overlapped for all the specimen, so a single limit curve is plotted representing both local and distortional buckling (indicated for brevity as "Local instability"). For each partition two figure are shown, the first one corresponds to the local (and distortional) instability occurrence, the second one corresponds to the global instability. Both of them are related to the stud that first buckles.

For partition P-1 up to the 0.50% inter-story drift (Figure 3.37a) the internal stresses in the stud no. 1 (see Figure A. 1 of the Appendix) are in the safe zone, for the 0.50% inter-story drift local instability occurs. When the partition reaches an inter-story drift equal to 1.30% (Figure 3.37b), the stud no. 1 globally buckles. For the same inter-story drift in the other studs only local buckling occurs. Nevertheless, the whole partition can be considered failed at this step.

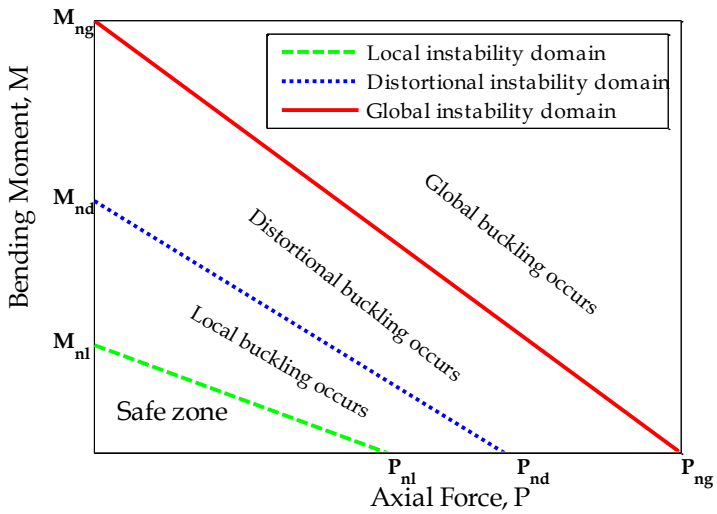

Figure 3.36. Local, distortional and global buckling domain for partition verification

In partition P-2 local instability occurs in stud 1 (Figure A. 5) for 0.45% drift (see dotted line in Figure 3.38a), while the internal forces exceed the global domain (black solid line in Figure 3.38b) when the partition drift reaches the 0.9% inter-story drift.

The Figure 3.39 refers to the specimen P-3 for which local instability occurs in stud 3 (Figure A. 9) at 0.54% inter-story drift (Figure 3.39a). The stud shows global instability for 1.3% inter-story drift (Figure 3.39b).

Finally, for specimen P-4 local instability occurs for 0.70% drift, while for a 1.40% inter-story drift global instability is observed in stud no.3 (Figure A. 13).

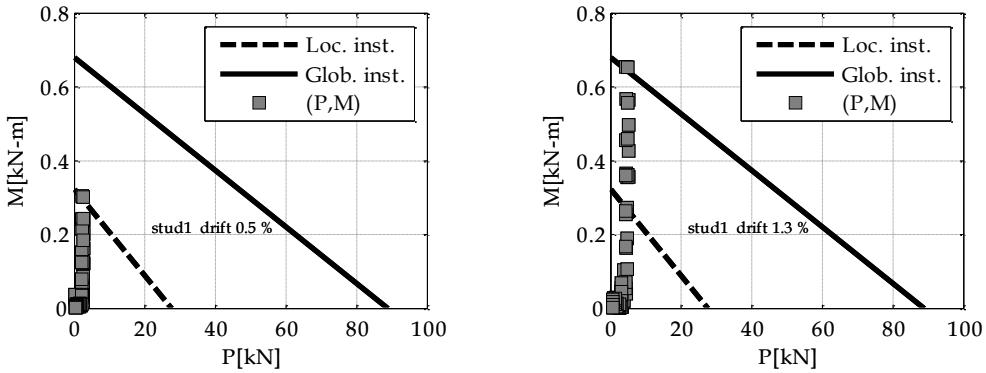

Figure 3.37 – (a) Local and (b) global instability occurrence for P-1 specimen FEM model

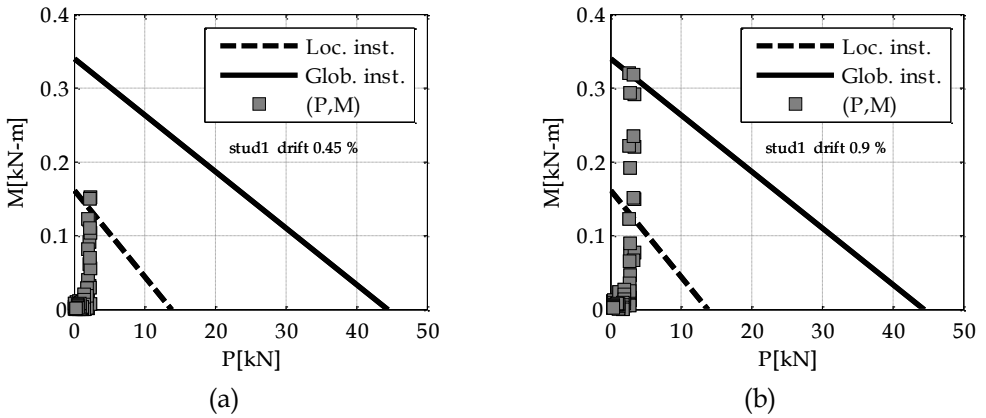

Figure 3.38 - (a) Local and (b) global instability occurrence for P-2 specimen FEM model

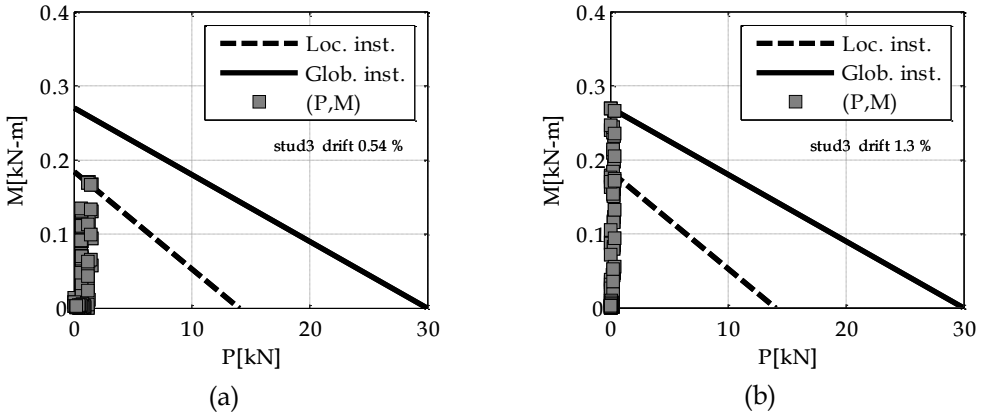

Figure 3.39 - (a) Local and (b) global instability occurrence for P-3 specimen FEM model

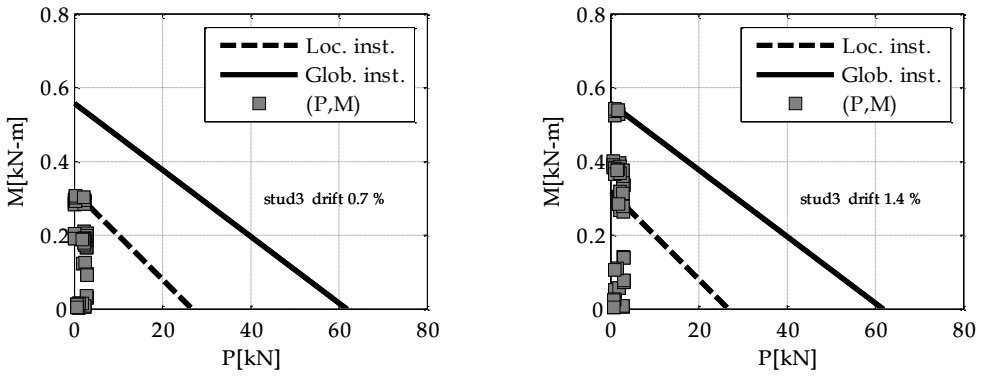

Figure 3.40 - (a) Local and (b) global instability occurrence for P-4 specimen FEM model

3.3.2 Experimental – numerical damage comparison

A comparison between the experimental damage of the tested partitions and the prediction of the analytical model is performed in this Section.

In Figure 3.41 the comparison between the analytical envelope curve (solid black line) and the numerical backbone (solid red line) is shown for the partition P-1. The green point on the analytical curve denotes the screws yielding, while the red one is representative of the global buckling of the partition. The nonlinear behavior of the screws occurs for a 10 mm top displacement, quite in accordance with the experimental evidence in which nonlinearity occurs for a 16 mm top displacement. The failure of the analytical model occurs for a 70 mm top displacement, corresponding to a 1.4% inter-story drift, considering the occurrence of global instability in a single stud as the partition failure. Beyond this point, the curve is plotted as a dotted line since it is not representative of the partition behavior. The analytical curve does not match the experimental one: both the strength and the

stiffness are underestimated. The experimental evidence demonstrates that at 95 mm displacement (1.90% drift) the specimen starts showing a global out-of-plane curvature. It can be deduced that the model estimates, from a safety side, the inter-story displacement required to induce global buckling failure mode of the specimen.

In case of partition P-2, the numerical model (red line in Figure 3.42), underestimates both the initial stiffness and the maximum strength with respect the experimental behavior. For an 11 mm top displacement some screws of the analytical model start to yield (green point in Figure 3.42), while the nonlinearity of the tested specimen is appreciable for a 16 mm top displacement. The numerical global instability occurs for a 0.90% inter-story drift (red point in Figure 3.42 for 45 mm displacement) that well catches the first out of plane instability of the tested partition, occurred for a 0.92% drift (corresponding to 46 mm top displacement).

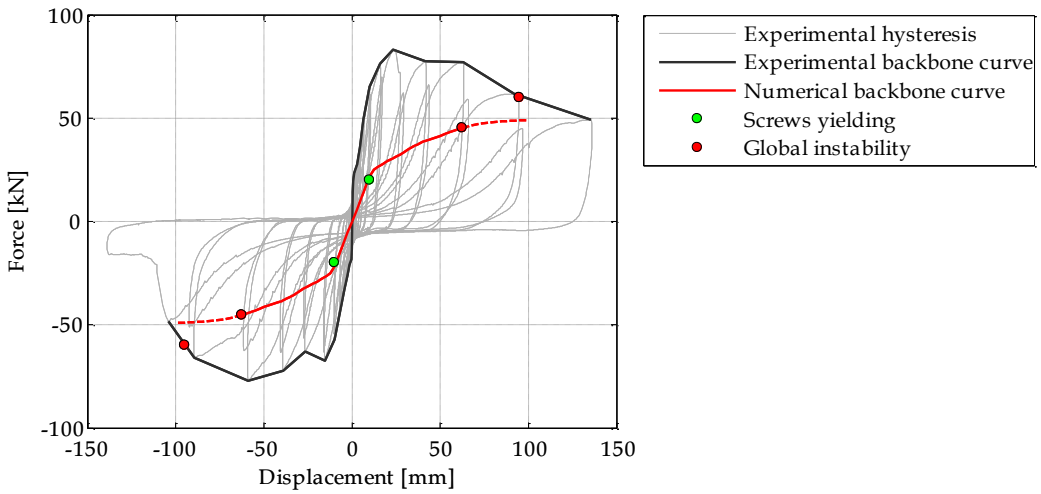

Figure 3.41 – Numerical pushover curve - experimental backbone curve comparison for partition P-1

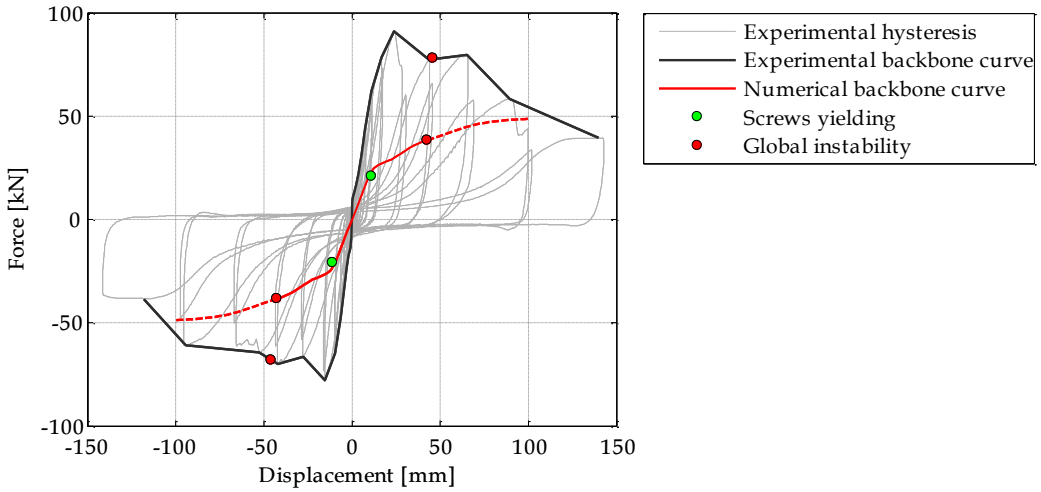

Figure 3.42 – Numerical pushover curve - experimental backbone curve comparison for partition P-2

For partition P-3, the comparison between the numerical pushover curve and the experimental force-displacement backbone curve is shown in Figure 3.42. In the analytical model, nonlinear behavior of the screws occurs for a top displacement equal to 10 mm (green marker in Figure 3.42); the failure of the partition (red marker in Figure 3.42) occurs at 1.30% interstory drift. The experimental curve exhibits an initial stiffness similar to the stiffness recorded in the analytical model. The screw bearing mechanism occurs at an 11 mm displacement, which is similar to the displacement required to yield some screws in the analytical model.

Beyond a 10 mm top displacement, the analytical curve does not match the experimental one: both the strength and the stiffness are underestimated. Finally, the experimental evidence demonstrates that at 68 mm displacement (1.37% drift) the specimen starts showing a global out-of-plane curvature. It can be deduced that the model well catches the inter-story displacement required to induce global buckling failure mode of the specimen. At that point, the force acting on the partition is also well predicted by the model.

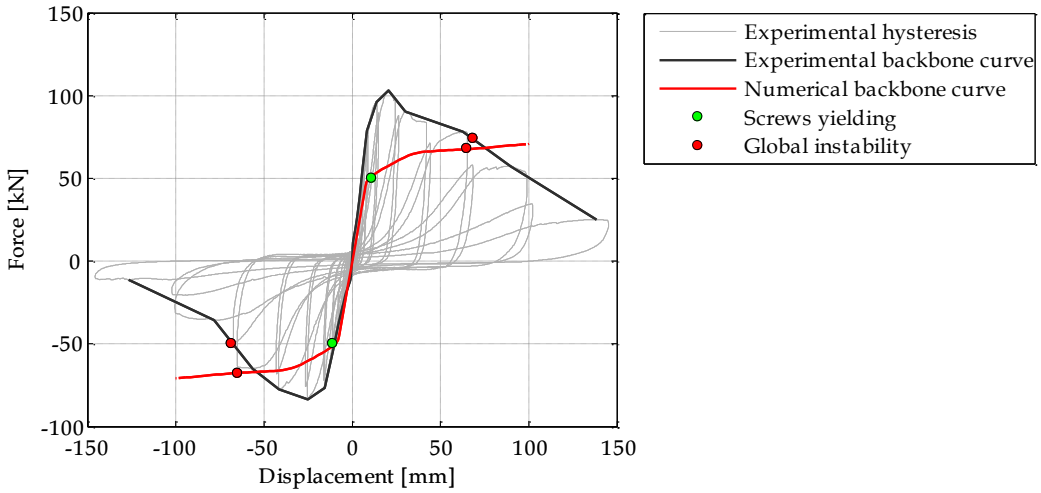

Figure 3.43 - Numerical pushover curve - experimental backbone curve comparison for partition P-3

The Figure 3.44 shows the comparison between the numerical pushover curve (red line) and the experimental envelope (black line) for partition P-4. The numerical model fits the initial stiffness of the tested partition up to the screws yielding, occurring for a 9-10 mm displacement (green point in Figure 3.44). Beyond this value that exactly corresponds to the experimentally evidenced screw bearing mechanism, the numerical curve does not fit the experimental one. The displacement corresponding to the global instability in the numerical model is equal to 70 mm (1.40% drift), while the first out of plane cusp in visible in the tested partition for a 1.6% inter-story drift, i.e. 80 mm top displacement.

To summarize, in all the partition model the analytical backbone curve does not match well both the initial stiffness and partition maximum strength. This phenomenon is due to the non-inclusion of the paper and the compound in the model (see §3.2). However, this approximation is limited up to the failure of the paper and the compound that occurs for all the specimens at about 20 mm top displacement, i.e. well before the failure of the specimen.

Instead, the global instability inter-story drift is well caught by the numerical model, even if in some case it is safe sided, as highlighted in Table 3.5. Furthermore, the positions of the cross sections of the studs where the internal forces exceed the global instability domain demonstrate that global buckling occurs exactly across the horizontal joint, confirming the experimental evidence (see Figure 3.27).

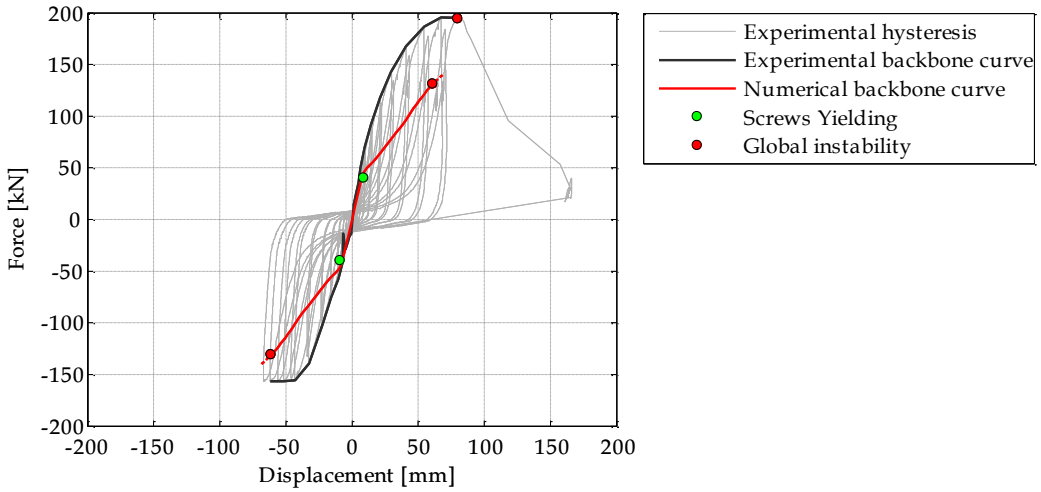

Figure 3.44 - Numerical pushover curve - experimental backbone curve comparison for partition P-4

Partition code	Experimental collpse drift [%]	Numerical collpse drift [%]
P-1	1.90	1.40
P-2	1.37	1.30
P-3	0.92	0.90
P-4	1.60	1.40

Table 3.5 – Numerical- experimental comparison in terms of collapse drift

3.3.3 Experimental – numerical strain comparison

A comparison in terms of strains between the numerical and the experimental models is illustrated in this Section.

For each partition (P-1, P-2, P-3, P-4) the strains recorded by the strain gauges on steel studs during the experimental tests are compared to the strains resulting from the models, for the same stud in the same position.

The analytical strains are evaluated from the analysis of the stud cross section subjected to the bending moment and the axial force, assuming linear elastic behavior. The experimental strains curves are obtained by considering both the positive and the negative peak strains achieved at each cycle of the experimental tests.

For partition P-1, the comparison between the recorded strain in strain gauge S3 and the strain recorded on stud no.1 is made in Figure 3.45. The numerical strain trend (solid line) is quite similar to the positive experimental one (dotted line). It is noteworthy that for a 25 mm partition top displacement the experimental negative strain gauge trend (dashed line) shows a variation of the slope (green point in Figure 3.45), which can be associated to the local instability recorded in the numerical model. For a 65 mm top displacement the slope increase should be associated to the global instability evidenced by the numerical model. Obviously, these slope variations are not caught by the model, since the buckling verification is performed at the end of the analysis.

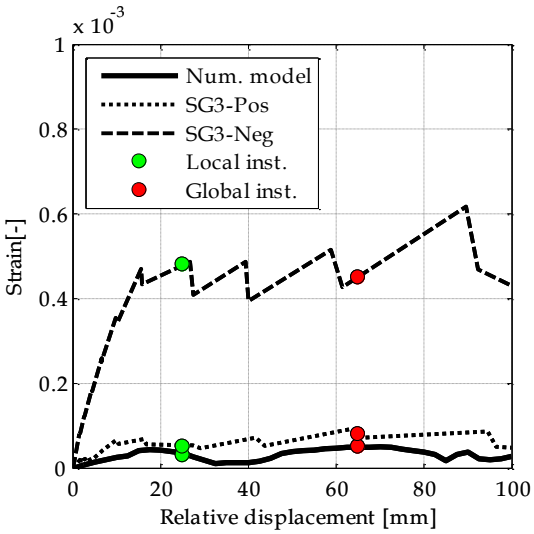

Figure 3.45 - Strain recording (SG3) trends vs relative displacement demand on stud no. 1 of partition P-1

In Figure 3.46 the comparison between the numerical strains and the experimental strain gauges recordings is made for partition P-2. In both cases (strain gauges SG3 on stud no. 5 and strain gauge SG4 on stud no. 4), beyond the blue markers, which denote the paper crack recorded during the experimental tests, the experimental curves (dashed and dotted lines) show a slope increase. In correspondence of the local instability occurrence (green point) no slope variation is observed in the experimental recordings, while both the positive and the negative envelopes point out an abrupt slope variation for the numerical global instability occurrence (red points). As mentioned before, the slope variations are not caught by the model (solid line), since the buckling verification is performed at the end of the analysis.

For partition P-3, from the comparison of the strains in stud no. 1 (Figure 3.47), the main difference is evidenced for small relative displacements, i.e. up to the paper cracking (blue marker), due to the absence of the paper and the compound between the plasterboard. Indeed, for low displacement demand level, the plasterboards absorb the total lateral load and the stud is lightly loaded. This phenomenon is not caught by the model since the paper and the compound between adjacent plasterboards are not included in the model.

Beyond the blue marker in Figure 3.48, the steel stud is stressed and the experimental curve exhibits a slope increase. It should be noted that the slope of the strain-displacement curve is very close to the numerical one.

For a relative displacement close to 30 mm, represented by the green marker in the plot, the experimental curve denotes an abrupt variation of the slope, which can be associated to the local buckling failure of the stud, confirming the numerical results. Finally, the global buckling of the stud is clearly evident on the experimental curve for a displacement close to 68 mm, confirming the numerical results. Hence, the curve after 68 mm should be neglected.

In case of partition P-4, the numerical strains are compared only to the positive envelope of the strain recorded in strain gauge SG3. The curves slope are quite similar for different displacement level and the experimental curve shows a slope variation for 35 mm displacement (green point) when local instability occurs in the numerical model.

The strain trends herein analyzed confirm that the inter-story displacement required to induce both local and global instabilities are well predicted by the numerical FEM model.

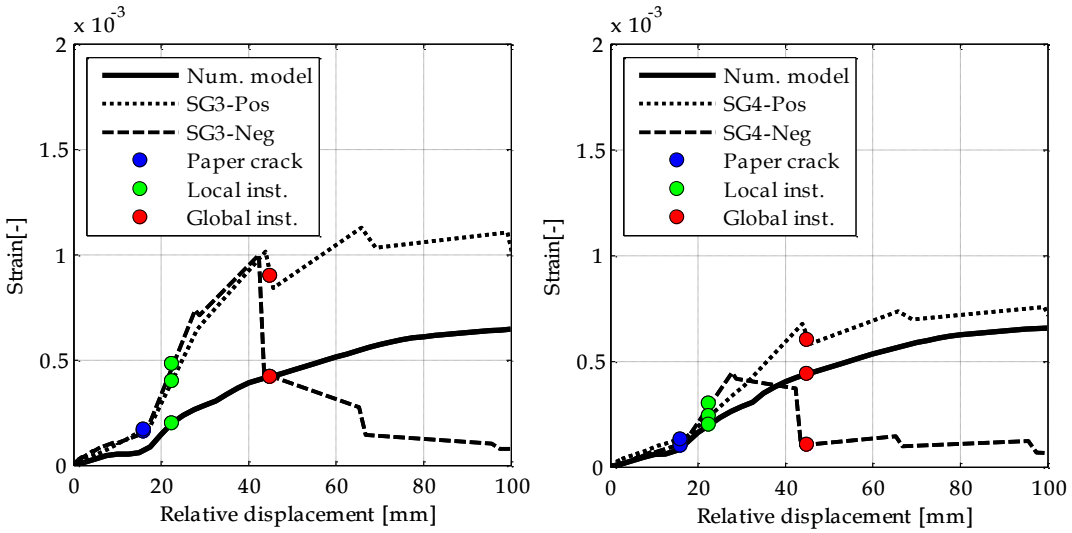

Figure 3.46 - Strain recording (SG3-SG4) trends vs relative displacement demand on stud no. 5 and stud no. 4 of partition P-2

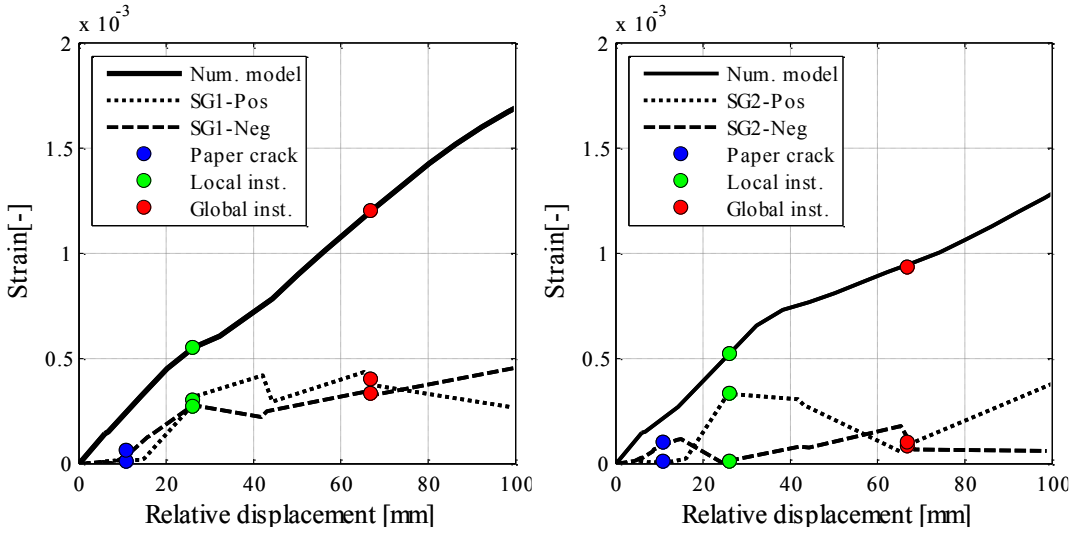

Figure 3.47. Strain recording (SG1 and SG2) trends vs relative displacement demand on stud no. 1 of partition P-3

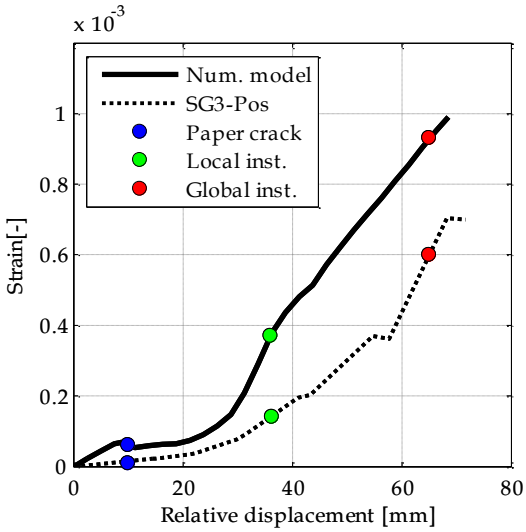

Figure 3.48 - . Strain recording (SG3) trends vs relative displacement demand on stud no. 8 of partition P-4

3.4 FEM model improvement

The FEM model (identified as *classic* model), described in the previous section and used for the seismic assessment of plasterboard partitions, has the advantage of being a very simple model, able to identify the drift related to the local instability of the studs, and the collapse drift of the partition, corresponding to the studs' global instability. Nevertheless, the FEM analysis, performed on models representative of tested partitions, have highlighted that the numerical model is not able to fit the stiffness and the maximum strength of the real partitions, even if the collapse drift is well caught (Table 3.5).

In order to improve the numerical – experimental fitting a *refined* FEM model of a tested partitions is proposed. The *classical* FEM model and the *refined* one are subject to a nonlinear static analysis, assuming large displacements in SAP2000 program. Both the partitions model behavior is verified by using the Direct Strength Method proposed by Schafer.

3.4.1 Introduction of contact between plasterboard in the *refined* model

The *refined* model of the tested partition differs from the *classic* one in the introduction of contact element between the plasterboard and the plasterboard and the surrounding frame, neglected in the first step of the FEM model definition. The

contact is modelled by using *multi-linear plastic link* element available in SAP2000, whose backbone curve is defined assuming that:

- in **compression** field the plasterboard penetration must be avoid during the analysis; it is possible by assigning a link stiffness larger enough with respect the board stiffness. Since the board Young's modulus is on overage equal to 3500 MPa, a link stiffness equal to 35000 MPa is considered appropriate to simulate the board non-penetration;
- in **traction** direction, the contact element should represent the presence of paper and compound that contribute to the whole strength and stiffness of the partition up to their own failure. Therefore, a tensile elastic-brittle behaviour of the link is calibrate, so that the analytical behaviour of the partition corresponds to the experimental one.

The complete force displacement curve of the multi-linear plastic link is shown in Figure 3.49.

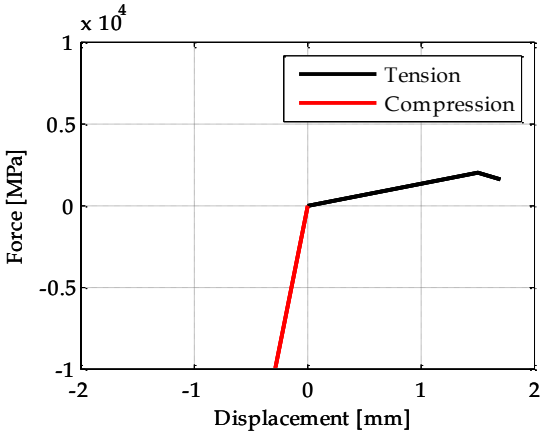

Figure 3.49 – Force-displacement curve for contact element

The multi-linear elastic links are assigned to the model as shown in Figure 3.50.

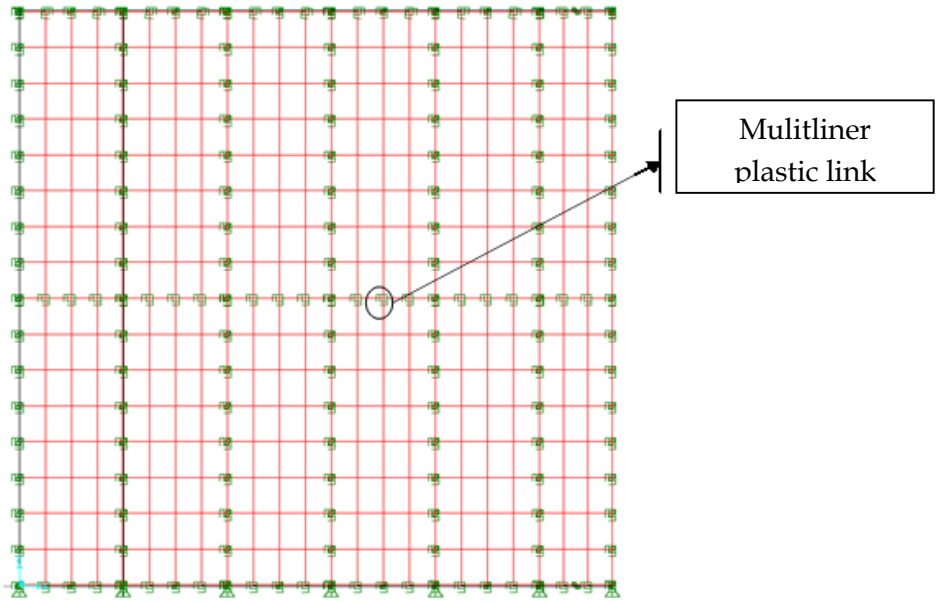

Figure 3.50 - Refined partition model with multi-linear plastic link simulating plasterboard contact

3.4.2 Results and discussions

Both the *classical* and the *refined* numerical models are subjected to a large displacement nonlinear static analysis (pushover) in displacements control. In both cases the bending moment diagram on studs reveals high stress values crossing horizontal joint, above and below the joint (Figure 3.51).

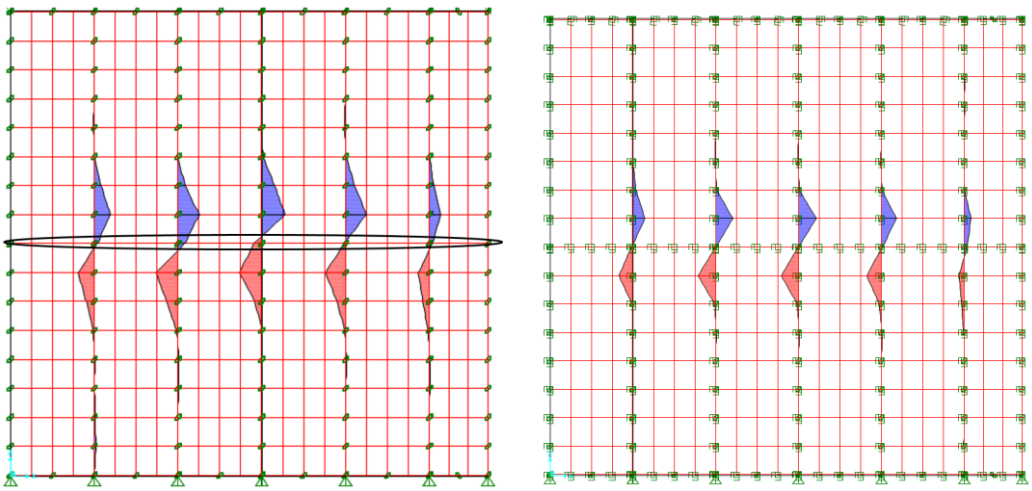

(a) (b)

Figure 3.51 - Diagrams of bending moments on the studs in (a) *classical* model and (b) *refined* model

On the base of the axial load and bending moment acting on the studs, the partition behavior is verified according to the DSM. The Table 3.6 shows the values corresponding to the collapse drift both for classic and refined models, compared to the experimental one. In both cases the global instability of the modelled partition occurs for a about 0.4 % inter-story drift, this value is safe sided with respect the experimental one.

Model	**Experimental collpse drift** *[%]*	**Numerical collpse drift** *[%]*
Classic	0.41	0.89
Refined	0.40	

Table 3.6 – Drift corresponding to the global instability of the numerical models, classic and refined, compared to the experimental one

Both the numerical models, classic and refined one, are compared to the experimental behavior of the tested partition, in term of push over curve, as shown in Figure 3.52. An early comparison between numerical force - displacement backbone curve of the *classical* model and experimental hysteretic curve shows that the numerical model (red in Figure 3.52) underestimates both the stiffness and the strength of the tested specimen. This phenomenon is due to the non-inclusion of the contact between the plasterboards and of the paper and compound in the model. Indeed, the numerical *refined* model, including the multi-linear plastic link, simulating the contact between plasterboard, is able to predict both the initial stiffness and the maximum strength (green curve in Figure 3.52) of the tested partition. This model including the contact between the plasterboards needs to be improved, since it must be calibrated on a greater number of tested partitions. Furthermore, it should be taken into account the progressive removal of nonlinear plastic link simulating the presence of paper and compound, whose contribute is negligible after a certain level of inter-story drift. At present, some attempts are being made in this direction.

However, as explained above the refined model provides the same collapse drift of the classic one, then it can be concluded that, since the target of the present study consists on evaluating the in plane seismic performance of the plasterboard partition, defining the inter-story drift ratio that induces the failure, the classical numerical model is to be preferred. In this case, indeed, the computational effort is reduced in terms of both modelling procedure and analysis times.

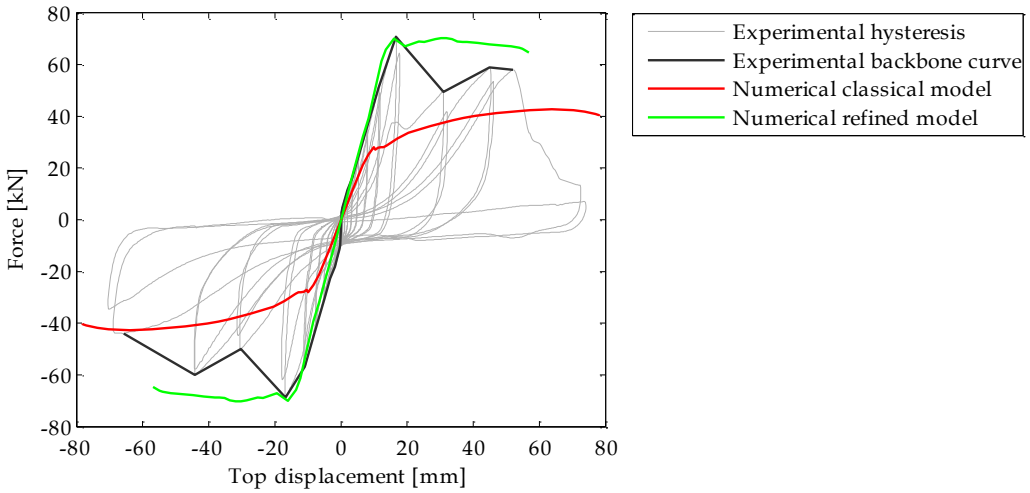

Figure 3.52 - Comparison between the experimental backbone curve and the numerical ones, both for classical (red line) and refined (green line) models

Chapter 4

FEM MODEL EXTENSION TO DIFFERENT CONFIGURATIONS OF PLASTERBOARD PARTITIONS

The FEM model proposed in Chapter 3 represents a simple technique to model the in-plane seismic behavior of plasterboard partitions, in order to evaluate the inter-story drift required to induce partition failure.

The numerical - experimental comparison proves the efficiency of the model. This model allows evaluating the collapse inter-story drift of several partitions, which cannot be investigated via experimental tests due to their configuration. Furthermore, it allows investigating the influence of several geometrical and mechanical parameters on the collapse drift ratio; indeed, in this chapter the application of the FEM model to different partitions, whose width and height are larger than the tested partitions, is presented.

4.1 Numerical tool development for FEM model computerization

The evaluation of the inter-story drift that induces the partition collapse, as before mentioned, is assessed through the application of the Schafer's method, by using the studs' internal forces, in terms of axial force and bending moment, resulting from the static nonlinear analysis in large displacement, which the generic partition is subject to. This implies a prior definition of the FEM model of the partition, respecting all the mechanical and the geometrical features. When the

partition dimensions increase, a huge computational effort in the FEM model definition and in the output data processing is required. With the aim of speeding up the whole procedure of partition modelling and data post-processing, an automatic tool is developed, through the MatLab software. A schematic flow chart of the automatic procedure is shown in Figure 4.1.

Starting for the input data, the pre-processor file generates a text file containing all the information required for the definition of the model in SAP2000 program. The latter automatically starts to perform the nonlinear static analysis on the modelled partition up to a defined inter-story drift (usually 3.00%). The analysis output are processed by the post-processor file, which extrapolates the buckling load factor from the CUFSM software and calculates the collapse drift, corresponding to the global instability domain overcoming.

This automatic procedure, detailed in the follow, represents a valued tool aimed not only for assessing the in-plane seismic performance of several plasterboard partition configurations, but also for performing a huge number of analysis in order to evaluate the influence of different parameters on the collapse drift.

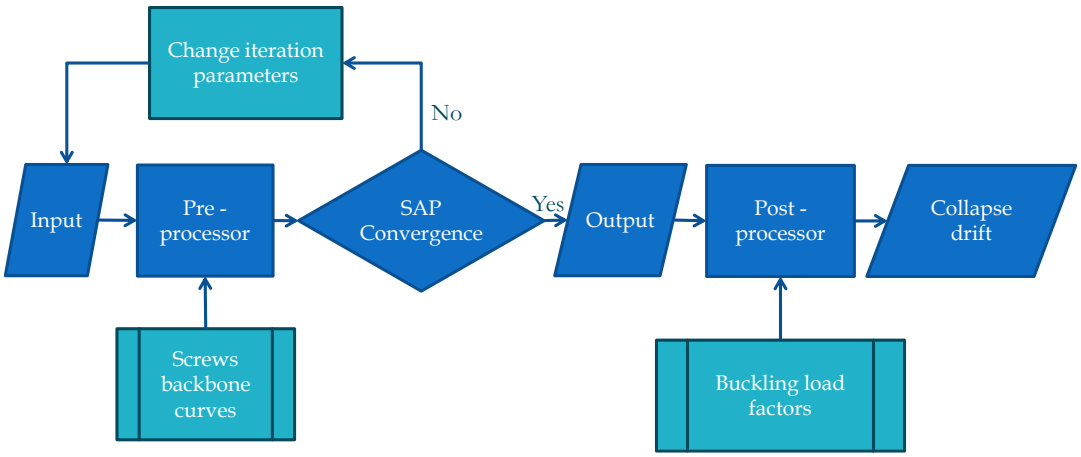

Figure 4.1 – Schematic flow chart of the automatic tool for seismic assessment of plasterboard partition

4.1.1 Pre-processor development

The pre-processor tool is composed of three Matlab files:

- the *Input.m* file
- the *Preprocessor.m* file
- the *Sap_Anlysis.m* file

On the base of the features of the partition, for which the in plane seismic performance is to be assessed, the user must be change the input data in the *Input.m* spreadsheet, as simple indicated in Figure 4.2.

```
clear all
clc
close all

%------------------INPUT DATA-----------------------------------------------------------
f1=1; %[N] actuator force
l=3000;%[mm] %width of the partition
h=11000; %[mm] %height of the partition
stud_sp=400;  %[mm] %studs spacing
screw_sp_v=300;%[mm] %screws spacing in vertical direction
screw_sp_h=0;%[mm] %screws spacing in horizontal direction %Put 0 if not provided%
hb=2600; %[mm] %height of the board
h_s=150; %[mm] stud height - C Section
w_s=50; %[mm] stud width - C Section
t_s=0.6; %[mm] stud tickness - C Section
stud_type=2; %Put 1 for C-Section simple%  %Put 2 for C-Section Back to Back"
board_width=1200; %[mm] %width of the board

lastra='ba15f';  %ba13=BA 13  Double layer
                 %ba18=BA 18  Double layer
                 %ba18ol=BA 18 one layer
                 %ba13f=BA 13 Double layer Pregyflam
                 %ba15f=BA 15 Double layer Pregyflam



%-------------------------------------------------------------------------------------
```

Figure 4.2 – Screenshot of the *Input.m* spreadsheet

The input data can be gathered as follow:

- partition geometrical dimensions (*l* , *h* and *stud_sp* parameters);
- horizontal and vertical screws spacing (*screw_sp_v* and *screw_sp_h*);
- studs' typology and studs cross section dimension (*h_s*, *w_s*, *t_s* and *stud_type*);
- panel geometrical dimension (*hb*, *board_width*);
- panel typology (*lastra*).

The choice of the panel typology (variable *lastra*) automatically assigns a panel-to-stud screwed connection to the partition, according to the force displacement curves defined in §3.2.1.2.

When the *Input.m* spreadsheet is complete, the *Preprocessor.m* file collects the input data and compiles a text file, namely *Preprocessor_SAP.$2k*, which can be read by the Sap2000 programs to generate the FEM model.

The *Preprocessor.m* spreadsheet includes several scripts put in the logical order of Sap2000 compiling:

1. Material definition (Figure 4.3): the lines are compiled in order to define the steel and the gypsum properties;

```
%------------MATERIAL DEFINITION----------------------------------------
fprintf(fid,'%s \n','TABLE:  "MATERIAL PROPERTIES 01 - GENERAL"');
fprintf(fid,'%s \n','Material=CF   Type=ColdFormed   SymType=Isotropic   TempDepend=No   Color=Blue ');
fprintf(fid,'%s \n',' ');

fprintf(fid,'%s \n','TABLE:  "MATERIAL PROPERTIES 02 - BASIC MECHANICAL PROPERTIES"');
fprintf(fid,'%s \n','Material=CF  UnitWeight=0   UnitMass=0   E1=210000 | G12=80769.2307692308   U12=0.3   A1=0.0000117');
fprintf(fid,'%s \n',' ');

fprintf(fid,'%s \n','TABLE:  "MATERIAL PROPERTIES 03D - COLD FORMED DATA"');
fprintf(fid,'%s \n','Material=CF   Fy=300   Fu=310.26410502821   SSHysType=Kinematic');
fprintf(fid,'%s \n',' ');

fprintf(fid,'%s \n','TABLE:  "MATERIAL PROPERTIES 04 - USER STRESS-STRAIN CURVES"');
fprintf(fid,'%s \n','Material=CF   Point=1   Strain=-1.22631904761905E-03 Stress=-300');
fprintf(fid,'%s \n','Material=CF   Point=2   Strain=0   Stress=0 PointID=A');
fprintf(fid,'%s \n','Material=CF   Point=3   Strain=1.22631904761905E-03 Stress=300');

fprintf(fid,'%s \n','TABLE:  "MATERIAL PROPERTIES 06 - DAMPING PARAMETERS"');
fprintf(fid,'%s \n','Material=CF   ModalRatio=0   VisMass=0   VisStiff=0   HysMass=0   HysStiff=0');
fprintf(fid,'%s \n',' ');
```

Figure 4.3 – Screenshot of the *Preprocessor.m* spreadsheet defining the material properties

2. Frame section, area section and link element force-displacement curve definition: this part of the script is intended to define the geometrical and the mechanical features of the stud cross section (Figure 4.4) and of the area elements defining the plasterboard (Figure 4.5). Furthermore, on the base of the uploaded panel-to-stud screwed connections, the script defines the force displacement curve of the nonlinear link elements.
3. Nodes coordinates definitions: the third section of the *Preprocessor.m* spreadsheet defines the nodal coordinates for frames and areas definition. Due to the appreciable partitions dimension, the high number of shells defining the plasterboard and the gap between plasterboard themselves, and plasterboard and the surrounding frame, several cycles composes the script in defining the nodal coordinates. The Figure 4.6 shows a screenshot in which a *for*-cycle is defined in order to generate the nodal coordinates of the plasterboard shells.
4. Frame, area and link element definitions: the nodes earlier defined are connected in order to generate frame elements (stud and surrounding

frame), shell elements (plasterboard panels) and link elements (panel-to-stud screws connections). Example of frame, area and link definition scripts are depicted in Figure 4.7, Figure 4.8 and Figure 4.9, respectively.

```
%-----------FRAME SECTION DEFINITION-----------------------------------------
%per stud tipo A (per stud tipo B usare un numero diverso da 1)
fprintf(fid,'%s \n','TABLE:  "FRAME SECTION PROPERTIES 01 - GENERAL"');
if stud_type==1
    if h_s==150
        fprintf(fid,'%s \n',(char (['SectionName="Stud"   Material=CF   Shape=General   t3=457.2   t2=252 _'])));
        fprintf(fid,'%s \n',(char (['  Area=156.48 TorsConst=18.5305 I33=525462.0495 I22=42999.7057 AS2=88.08 AS3=56.16 _'])));
        fprintf(fid,'%s \n',(char (['  S33=7006.1607   S22=1124.3498   Z33=7006.1607   Z22=1124.3498 _'])));
        fprintf(fid,'%s \n',(char (['R33=58.3334   R22=16.687   ConcCol=No   ConcBeam=No   Color=Gray8Dark '])));
        fprintf(fid,'%s \n',(char (['TotalWt=0   TotalMass=0   FromFile=No   AMod=1   A2Mod=1   A3Mod=1   JMod=1 '])));
        fprintf(fid,'%s \n',(char (['I2Mod=1   I3Mod=1   MMod=1   WMod=1   Notes="Added 17/10/2014 12:08:14"'])));

    elseif h_s==100
        fprintf(fid,'%s \n',(char (['SectionName="Stud"   Material=CF   Shape=General   t3=457.2   t2=254 _'])));
        fprintf(fid,'%s \n',(char (['Area=126.48   TorsConst=14.9305   I33=207264.47   I22=38113.24   AS2=58.08   AS3=56.16 _'])));
        fprintf(fid,'%s \n',(char (['S33=4145.2895   S22=1074.1617   Z33=4145.2895   Z22=1074.1617 _'])));
        fprintf(fid,'%s \n',(char (['R33=40.8146   R22=17.5021   ConcCol=No   ConcBeam=No   Color=White '])));
        fprintf(fid,'%s \n',(char (['TotalWt=0   TotalMass=0   FromFile=No   AMod=1   A2Mod=1   A3Mod=1   JMod=1   I2Mod=1 '])));
        fprintf(fid,'%s \n',(char (['I3Mod=1   MMod=1   WMod=1   Notes="Added 17/10/2014 12:22:09"'])));
    end
else
    if h_s==150
        fprintf(fid,'%s \n',(char (['SectionName="Stud"   Material=CF   Shape=General   t3=457.2   t2=254 _'])));
        fprintf(fid,'%s \n',(char (['  Area=312.96   TorsConst=102.307633651777   I33=1072532.8512   I22=135591.1552   AS2=180.155317010425 _'])));
        fprintf(fid,'%s \n',(char (['  AS3=110.806108468442   S33=14300.438016   S22=2711.823104 _'])));
        fprintf(fid,'%s \n',(char (['Z33=16634.5919999999   Z22=3769.24799999996   R33=58.54110086766 _'])));
        fprintf(fid,'%s \n',(char (['  R22=20.8147531O5196   ConcCol=No   ConcBeam=No   Color=White   TotalWt=0   TotalMass=0  _'])));
        fprintf(fid,'%s \n',(char (['  FromFile=No   AMod=1   A2Mod=1   A3Mod=1   JMod=1   I2Mod=1   I3Mod=1 _'])));
        fprintf(fid,'%s \n',(char (['MMod=1   WMod=1   Notes="Added 04/11/2014 14:47:07"'])));
    elseif h_s==100
        fprintf(fid,'%s \n',(char (['SectionName="Stud"   Material=CF   Shape=General   t3=457.2   t2=254 _'])));
        fprintf(fid,'%s \n',(char (['Area=252.96   TorsConst=73.5003647589787   I33=423903.2512   I22=135583.9552   _'])));
        fprintf(fid,'%s \n',(char (['AS2=123.162281347767   AS3=110.785171432284   S33=8478.065024   S22=2711.679104 _'])));
        fprintf(fid,'%s \n',(char (['Z33=9560.59200000001   Z22=3751.248   R33=40.9361926161637   R22=23.1514514171314   _'])));
        fprintf(fid,'%s \n',(char (['ConcCol=No   ConcBeam=No   Color=White   TotalWt=0   TotalMass=0   FromFile=No  _'])));
        fprintf(fid,'%s \n',(char (['AMod=1   A2Mod=1   A3Mod=1   JMod=1   I2Mod=1   I3Mod=1   MMod=1 _'])));
        fprintf(fid,'%s \n',(char (['WMod=1   Notes="Added 04/11/2014 15:25:20"'])));
    end
end
```

Figure 4.4 – Screenshot of the *Preprocessor.m* spreadsheet defining the stud frame section properties

```
fprintf(fid,'%s \n','TABLE:  "AREA SECTION PROPERTIES"');
fprintf(fid,'%s \n',(char (['Section="Plasterboard' num2str(Thick) 'mm"   Material=Gypsum   MatAngle=0   AreaType=Shell _'])));
fprintf(fid,'%s \n',(char (['Type=Shell-Thin   DrillDOF=Yes   Thickness=' num2str(Thick)  ' BendThick=' num2str(Thick)   ' Color=Green _ '])));
fprintf(fid,'%s \n',(char (['F11Mod=1   F22Mod=1   F12Mod=1   M11Mod=1   M22Mod=1   M12Mod=1   V13Mod=1 _'])));
fprintf(fid,'%s \n','V23Mod=1   MMod=1   WMod=1   Notes="Added 04/03/2013 15.02.42"');
fprintf(fid,'%s \n',' ');

fprintf(fid,'%s \n','TABLE:  "AREA SECTION PROPERTY DESIGN PARAMETERS"');
fprintf(fid,'%s \n',(char (['Section="Plasterboard' num2str(Thick) 'mm"   RebarMat=None   RebarOpt=Default'])));
fprintf(fid,'%s \n',' ');
```

Figure 4.5 - Screenshot of the *Preprocessor.m* spreadsheet defining the plasterboard area section properties

```
%----------------JOINTS DEFINITION&RESTRAINT-----------------------------
fprintf(fid,'%s \n','TABLE:  "JOINT COORDINATES"');
%joint for plasterboard

for i=(stud_n*sh_nx)+2:(stud_n*sh_nx+1+l_sh_nx) %last bay
    for j=1:y_bay+1
        for k=1:sh_nz(end)+1
            if k-1<=sh_nz(1)
                fprintf(fid,'%s \n', (char (['Joint=' num2str(100000*j+1000*k+1*i) ' CoordSys=GLOBAL   CoordType=Cartesian '   'XorR='...
                num2str(stud_n*sh_nx*lx_sh+((i-(stud_n*sh_nx+1))*l_lx_sh))   ' Y=' num2str((j-1)*ly)   ' Z=' num2str((k-1)*lz_sh(1))...
                ' SpecialJt=Yes'])));
            else
                for r=2:size(sh_nz,2)
                    if k-1<=sh_nz(r) && k-1>sh_nz(r-1)
                        Z1=((k-1)-sh_nz(r-1))*lz_sh(r);
                        for m=2:r
                            Z_aggiunta=sh_nz(m-1)*lz_sh(m-1);
                        end
                        fprintf(fid,'%s \n', (char (['Joint=' num2str(100000*j+1000*k+1*i) ' CoordSys=GLOBAL   CoordType=Cartesian ' 'XorR=' ...
                        num2str(stud_n*sh_nx*lx_sh+((i-(stud_n*sh_nx+1))*l_lx_sh))   ' Y=' num2str((j-1)*ly)   ' Z=' num2str(Z1+Z_aggiunta)...
                        ' SpecialJt=Yes'])));
                    else
                    end
                end
            end
        end
    end
end
```

Figure 4.6 - Screenshot of the *Preprocessor.m* spreadsheet defining the plasterboard nodal coordinates

```
fprintf(fid,'%s \n','TABLE:  "CONNECTIVITY - FRAME"');
%stud elements
for j=1:y_bay+1
    for k=1
        for i=sh_nx+1:sh_nx:sh_nx*stud_n+1
            fprintf(fid,'%s \n', (char ([ 'Frame=' num2str((i-1)/sh_nx) ' JointI=' num2str(1100000*j+1000*k+1*i) '_' ])));
            fprintf(fid,'%s \n', (char ([ ' JointJ=' num2str(11100000*j+1000*(sh_nz(end)+1)+1*i) ' IsCurved=No' ])));
        end
    end
end
```

Figure 4.7 - Screenshot of the *Preprocessor.m* spreadsheet defining the frame elements

```
fprintf(fid,'%s \n','TABLE:  "CONNECTIVITY - AREA"');
%plasterboard central
%central
%1°
mont=[1:sh_nx:(stud_n*sh_nx)+1 0:sh_nx:stud_n*sh_nx (stud_n*sh_nx)+l_sh_nx (stud_n*sh_nx)+1+l_sh_nx];
for i=1:stud_n*sh_nx+l_sh_nx+1
    if i~=mont
        for j=1:y_bay+1
            for k=2:sh_nz(1)-1
                fprintf(fid,'%s \n',(char (['Area=scc_' num2str(k) '_' num2str(j) '_' num2str(i) ' NumJoints=' num2str(n)   ])));
                fprintf(fid,'%s \n',(char (['Joint1=' num2str(100000*j+1000*k+1*i) 'Joint2=' num2str(100000*j+1000*k+1*(i+1)) ])));
                fprintf(fid,'%s \n',(char (['Joint3=' num2str(100000*j+1000*(k+1)+1*(i+1)) ' Joint4=' num2str(100000*j+1000*(k+1)+1*i)])));
            end
        end
    end
end
```

Figure 4.8 - Screenshot of the *Preprocessor.m* spreadsheet defining the area elements

```
fprintf(fid,'%s \n','TABLE:  "CONNECTIVITY - LINK"');
%link on the left
for i=1:sh_nx:(stud_n*sh_nx)+1
    for j=1:y_bay+1
            for k=2:sh_nz(end)+1
                if k~=sh_nz+1
                fprintf(fid,'%s \n', (char ([ 'Link=l_' num2str(k) '_' num2str(j) '_' num2str(i) ])));
                fprintf(fid,'%s \n', (char ([  ' JointI=' num2str(100000*j+1000*k+1*i)  ' JointJ=' num2str(200000*j+1000*k+1*i)])));
                end
            end
    end
end
```

Figure 4.9 - Screenshot of the *Preprocessor.m* spreadsheet defining the area elements

The point 4) closes the definition phase; an assignment phase follows:

5. Frame, area and link element assignment: Figure 4.10, Figure 4.11 and Figure 4.12 show some lines of the scripts that define the elements assignment.

```
fprintf(fid,'%s \n','TABLE:  "FRAME SECTION ASSIGNMENTS"');
%stud elements
for j=1:y_bay+1
    for k=1
        for i=sh_nx+1:sh_nx:sh_nx*stud_n+1
            fprintf(fid,'%s \n', (char ([ 'Frame=' num2str((i-1)/sh_nx) ' SectionType="Cold Formed C"   AutoSelect=N.A.' ])));
            fprintf(fid,'%s \n', (char ([ 'AnalSect=Stud   DesignSect=Stud   MatProp=Default' ])));
        end
    end
end
```

Figure 4.10 – Screenshot of the *Preprocessor.m* spreadsheet for frame section assignment

```
fprintf(fid,'%s \n','TABLE:  "AREA SECTION ASSIGNMENTS" ');
%plasterboard central
%central
%1°
mont=[1:sh_nx:(stud_n*sh_nx)+1 0:sh_nx:stud_n*sh_nx (stud_n*sh_nx)+1_sh_nx (stud_n*sh_nx)+1+1_sh_nx];
for i=1:stud_n*sh_nx+1_sh_nx+1
    if i~=mont
        for j=1:y_bay+1
            for k=2:sh_nz(1)-1
                fprintf(fid,'%s \n', (char (['Area=scc_' num2str(k) '_' num2str(j) '_' num2str(i)  ])));
                fprintf(fid,'%s \n', (char ([ ' Section="Plasterboard' num2str(Thick) 'mm"   MatProp=Default'])));
            end
        end
    end
end
```

Figure 4.11 – Screenshot of the *Preprocessor.m* spreadsheet for area section assignment

```
fprintf(fid,'%s \n','TABLE:  "LINK PROPERTY ASSIGNMENTS"');
%link on the left (viti doppie)
for i=1:sh_nx:(stud_n*sh_nx)+1
    for j=1:y_bay+1
        for k=2:2:sh_nz(end)+1
            if k<=sh_nz+1
                fprintf(fid,'%s \n', (char ([ 'Link=l_' num2str(k) '_' num2str(j) '_' num2str(i) ])));
                fprintf(fid,'%s \n', (char ([ ' LinkType="MultiLinear Elastic"   LinkJoints=TwoJoint   LinkProp=Viti_singole_dimezzate '])));
            end
        end
    end
end
```

Figure 4.12 - Screenshot of the *Preprocessor.m* spreadsheet for link property assignment

6. Load assignment: the script defines the load to assign to the partition.
7. Constrain and restrain assignment: the Figure 4.13 illustrates a part of the code defining the hinge restrains at the partition bottom.

```
%hinge for joint at bottom
for i= [1 (stud_n*sh_nx+l_sh_nx)+1]
    for j=1:y_bay+1
        for k=1
           fprintf(fid,'%s \n', (char (['Joint=' num2str(100000*j+1000*k+1*i) ' U1=Yes   U2=Yes   U3=Yes   R1=No   R2=No   R3=No'])))
        end
    end
end

for i=1:sh_nx:(stud_n*sh_nx)+1
    for j=1:y_bay+1
        for k=1
           fprintf(fid,'%s \n', (char (['Joint=' num2str(200000*j+1000*k+1*i) ' U1=Yes   U2=Yes   U3=Yes   R1=No   R2=No   R3=No'])))
        end
    end
end

for i=[sh_nx+1:sh_nx:(stud_n*sh_nx)+1 stud_n*sh_nx+l_sh_nx+1]
    for j=1:y_bay+1
        for k=1
           fprintf(fid,'%s \n', (char (['Joint=' num2str(300000*j+1000*k+1*i) ' U1=Yes   U2=Yes   U3=Yes   R1=No   R2=No   R3=No'])))
        end
    end
end
```

Figure 4.13 - Screenshot of the *Preprocessor.m* spreadsheet for restraint assignment

When the user runs the tool from the *Input.m* spreadsheet, the *Preprocessor.m* file generates the FEM model of the partition. Then, automatically, the *Sap_Analysis.m* starts to work by using the SAP 2000 API (Applied Program Interface). In this manner, it is possible to interface the Matlab software to the SAP2000 program that performs the nonlinear static analysis up to the assigned inter-story drift.

The *Sap_Analysis.m* file connects the preprocessor phase to the post processor one, since it is able to take out from SAP2000 the analysis results (see Figure 4.14) in terms of nodal displacements, nodal reactions and frame internal forces, and to import them in the Matlab operating system.

```
%Output displacement
NumberResults = 0;
joint_Obj = cellstr(' ');
joint_Elm = cellstr(' ');
ACase = cellstr(' ');
StepType = cellstr(' ');
StepNum = zeros(1,1,'double');
U1 = zeros(1,1,'double');
U2 = zeros(1,1,'double');
U3 = zeros(1,1,'double');
R1 = zeros(1,1,'double');
R2 = zeros(1,1,'double');
R3 = zeros(1,1,'double');
GroupElm  = 2;

%Load case definition
% ret = Sap.Results.Setup.DeselectAllCasesAndCombosForOutput;
ret = SapObject.SapModel.Results.Setup.SetCaseSelectedForOutput('largedisp_mar') ;

% Definition for diplay the output (step-by-step)
ret =SapObject.SapModel.Results.Setup.SetOptionNLStatic(2);

%Create the output for joint displacement
[ret, NumberResults, joint_Obj, joint_Elm, ACase, StepType, StepNum, U1, U2, U3, R1, R2, R3] = ...
    SapObject.SapModel.Results.JointDispl ('All', GroupElm , NumberResults, joint_Obj, joint_Elm, ACase,...
     StepType, StepNum, U1, U2, U3, R1, R2, R3);
```

Figure 4.14 - Screenshot of the *Postprocessor.m* spreadsheet for extrapolating the analysis results

4.1.2 Post-processor development

The post processor files are strictly connected to the preprocessor since, run out the nonlinear analysis, two spreadsheet elaborate the analysis results:

-*Schafer_LoadFactor.m*;
-*Schafer_Domain.m*;

The *Schafer_LoadFactor.m* spreadsheet collects, from *the Input.m* file, all the informations about the partition configuration and calculates the parameters used as input in the CUFSM software for the load factor evaluation (§3.3.1). Using the Matlab files version of the CUFSM operating system, the latter is linked to the post-processor files, so it automatically runs and provides the values of instability load factors.

Finally, the *Schafer_Domain.m* spreadsheet elaborate the load factor and the analysis results to obtain the instability domains and the inter-story drift corresponding to the global instability of the analyzed partition. The final output are:

- the Schafer's domain of the stud that first globally buckles;
- the numerical value corresponding to the collapse inter-story drift;
- the pushover curve of the analysed partition.

4.2 Partitions' configurations

The partition configuration analyzed in this section are listed in Table 4.1. The specimens, codified as S-1, S-2 up to S-11, are selected as most representative of the plasterboard partitions produced and installed by the Siniat International S.p.A. in the European area. The table includes all the information required in order to understand the partition configurations. The last columns points out the maximum height at which the specific partition is produced. The maximum heights, provided by the Siniat International Company, are evaluated on the base of static considerations. For each partition the in plane seismic behavior is assessed by performing nonlinear static analysis in SAP2000 on the partition FEM models, as defined in §3.2. Finally the collapse drift is evaluated by applying the DSM, as explained in §3.3.1.

Code	Panel			Number of	Stud	Stud dimension			Stud	Maximum
	Type of board	*width*	*thickness*	**layer**	**typology**	*web*	*flange*	*thickness*	**spacing**	**height**
S-1	BA13	1.2 m	12.5 mm	2	simple	150 mm	50 mm	0.6 mm	600 mm	8.80 m
S-2	BA13	1.2 m	12.5 mm	2	back to back	150 mm	50 mm	0.6 mm	400 mm	11.85 m
S-3	Pregyflam 13	1.2 m	12.5 mm	2	simple	150 mm	50 mm	0.6 mm	600 mm	8.80 m
S-4	Pregyflam 15	1.2 m	15 mm	2	back to back	150 mm	50 mm	0.6 mm	400 mm	11.00 m
S-5	BA18S	0.9 m	18 mm	1	simple	150 mm	50 mm	0.6 mm	900 mm	8.40 m
S-6	BA 18S	0.9 m	18 mm	1	back to back	150 mm	50 mm	0.6 mm	450 mm	12.75 m
S-7	BA13	1.2 m	12.5 mm	2	back to back	150 mm	50 mm	0.6 mm	600 mm	10.35 m
S-8	BA 13	1.2 m	12.5 mm	2	simple	150 mm	50 mm	0.6 mm	400 mm	10.30 m
S-9	BA 18	1.2 m	18 mm	2	back to back	100 mm	50 mm	0.6 mm	400 mm	7.00 m
S-10	BA 18S	0.9 m	18 mm	1	back to back	150 mm	50 mm	0.6 mm	900 mm	10.45 m
S-11	BA 18S	0.9 m	18 mm	1	simple	150 mm	50 mm	0.6 mm	450 mm	10.45 m

Table 4.1 – Modelled partition for collapse drift evaluation

4.3 Influence of the partitions height on the collapse drift

The tool presented in §4.1 is used in order to perform the numerical analysis on the partition listed in Table 4.1. In particular, with the aim of evaluating the influence of the partition dimension on the collapse drift, for each partition, maintaining the width constant and equal to the width of the tested partitions, i.e. 5 meters, several nonlinear analysis are performed by varying the height from 5 meters to the maximum static height, with a 1 meter spacing. The Table 4.2 lists the investigated height for each partition and the total number of the analyzed partitions. The complete computerization of the analysis procedure allows to model 70 partitions and to perform 70 nonlinear analyses in a very short time.

The results are shown in terms of force – inter-story drift ratio curves and collapse drift.

Partition Code	Investigated heights *[m]*	No. of partitions
S-1	5-6-7-8-8.80	5
S-2	5-6-7-8-9-10-11-11.85	8
S-3	5-6-7-8-8.80	5
S-4	5-6-7-8-9-10-11	7
S-5	5-6-7-8-8.40	5
S-6	5-6-7-8-9-10-11-12-12.75	9
S-7	5-6-7-8-9-10-10.35	7
S-8	5-6-7-8-9-10-10.30	7
S-9	5-6-7	3
S-10	5-6-7-8-9-10-10.45	7
S-11	5-6-7-8-9-10-10.45	7
	TOTAL	**70**

Table 4.2 – Investigated heights for each specimen

The Figure 4.15 shows the pushover curves for the specimen S-1: each of them is representative of the in-plane behavior of the specimen for the investigated height. As the figure highlights, the pushover curves are completely overlapped in the elastic field, evidencing the same initial stiffness for all the partitions, while they slightly differ in plastic field. It can be observed that the maximum strength is associated to the lower partition, i.e. 5 meters high (violet curve in Figure 4.15); the strength gradually decrease with the height increase.

The black dot on each curve of Figure 4.15 stands for the collapse drift, evaluated according to the methodology illustrated in the Chapter 3. The overlapped dots point out that the collapse drift is quite the same with height change, as listed also in Table 4.3. Therefore, a constant value of collapse drift, namely ϑ=0.96±0.07%, can be considered for the analyzed partition, regardless of the partition height, with an error less than 8% with respect the mean value, as shown in Figure 4.16.

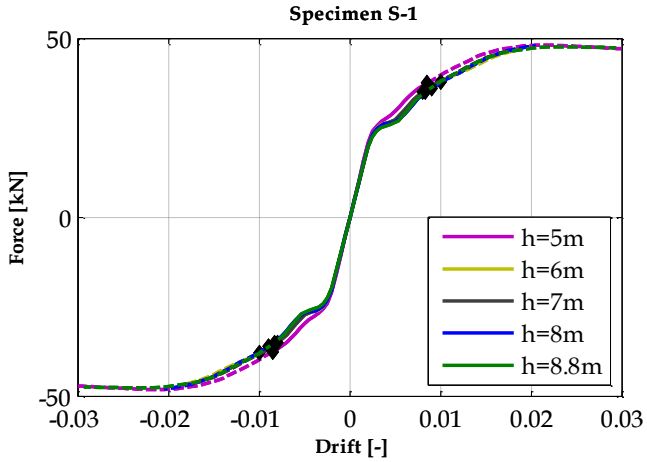

Figure 4.15 – Force vs drift pushover curve for S-1 partition at different heights

Specimen S-1		
Heights	**Horizontal joints number**	**Collapse drift**
[m]	*[-]*	*[%]*
5	1	0.90
6	2	1.10
7	2	0.90
8	3	0.95
8.8	3	0.95
mean value		**0.96±0.07**

Table 4.3 – Collapse drift of S-1 partition for different partition heights

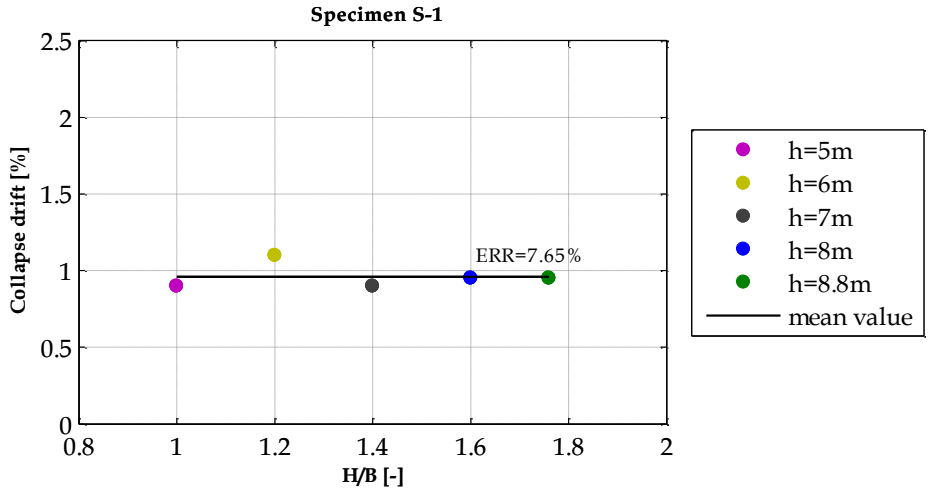

Figure 4.16 – Collapse drift vs H/B ratio for partition S-1

For the specimen S-2 the force-drift pushover curves for different heights are shown in Figure 4.17. Even if no black point is drown, for each partition height a lower bound of the collapse drift is identified, as shown in Table 4.4. These values are related to the maximum drift achieved during the analysis, for which no collapse is observed. Computational problems did not allow to perform further analysis steps. The results are considered satisfying since the collapse drift are greater than ϑ=2%.

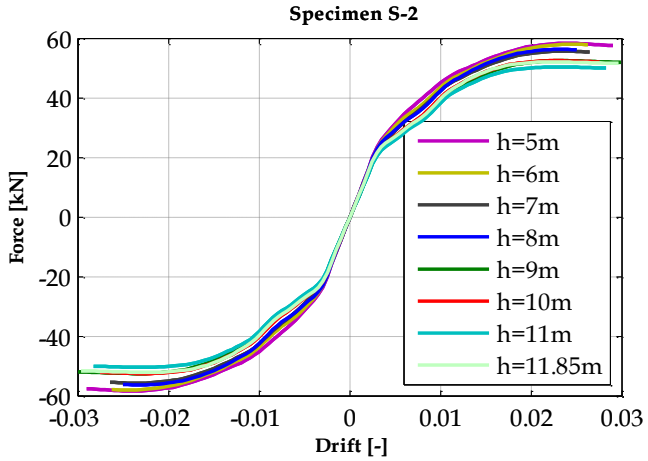

Figure 4.17 - Force vs drift pushover curve for S-2 partition at different heights

Specimen S-2		
Heights	**Horizontal joints number**	**Collapse drift**
[m]	*[-]*	*[%]*
5	1	> 2.9
6	2	> 2.6
7	2	> 2.6
8	3	> 2.5
9	3	> 3.0
10	3	> 2.7
11	4	> 2.8
11,85	4	> 3.0

Table 4.4 - Collapse drift of S-2 partition for different partition heights

Similar considerations, about the constant collapse drift ratio, and the quite similar in-plane behavior at different heights, can be done for all the analyzed partitions as reported in:

- Figure 4.18, Figure 4.19 and Table 4.5 for specimen S-3;
- Figure 4.20, Figure 4.21 and Table 4.6 for specimen S-4;
- Figure 4.22, Figure 4.23 and Table 4.7 for specimen S-5;
- Figure 4.24, Figure 4.25 and Table 4.8 for specimen S-6;
- Figure 4.26, Figure 4.27 and Table 4.9 for specimen S-7;
- Figure 4.28, Figure 4.29 and Table 4.10 for specimen S-8;
- Figure 4.30 and Table 4.11 for specimen S-9;
- Figure 4.31, Figure 4.32 and Table 4.12 for specimen S-10;
- Figure 4.33, Figure 4.34 and Table 4.13 for specimen S-11;

Despite these common aspects, it should be noted that a different collapse drift ratio is evaluated for each partition, since they differ from each other for type of steel studs and boards, for stud spacing and panel arrangement, as evidenced in Table 4.1.

Interesting evaluations can be done by comparing the behavior of similar specimens. As the Figure 4.16 points out, the collapse drift of the specimen S-1 is on overage equal to 0.95%, while the collapse drift for specimen S-2 is on overage larger

than 2.5% (Table 4.4). Partition S-1 and partition S-2 differ only for stud spacing, i.e., i.e. 600 mm in the former specimen, 400 mm in the latter one.

The results of the static nonlinear analyses show that the internal stresses are uniformly distributed along the different studs at a certain partition horizontal section. This always happens, also when the partition height increases. Furthermore, an higher stud density results in a fairer stress distribution at a given displacement, because it is not associated to a relevant increment of the partition stiffness.

Consequently, concerning the different behavior of the specimens S-1 and S-2, the larger collapse drift of the latter specimen is justified by the its reduced stud spacing and, hence, by the lower internal axial load and bending moment in each stud. This aspect is clearly pointed out also in the comparison between the specimens S-5 and S-6: the stud spacing is halved in the second specimen, as evidence in Table 4.1, and the collapse drift is improved, rising from a mean value of 0.35% to a collapse drift value of 2%. Similar considerations can be done for specimens S-10 and S-11: the double stud spacing of the second partition with respect the first one results in a higher collapse drift, namely it increase from 0.8% to 1.3%.

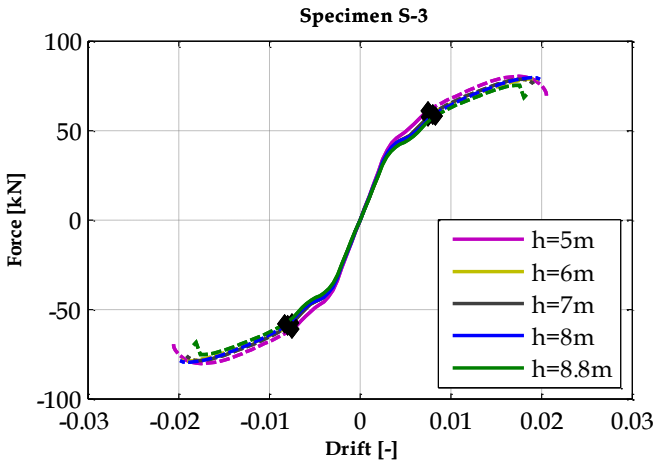

Figure 4.18 - Force vs drift pushover curve for S-3 partition at different heights

Specimen S-3		
Heights	**Horizontal joints number**	**Collapse drift**
[m]	*[-]*	*[%]*
5	1	0.80
6	2	0.85
7	2	0.80
8	3	0.85
8.8	3	0.90
mean value		**0.84±0.04**

Table 4.5 - Collapse drift of S-3 partition for different heights

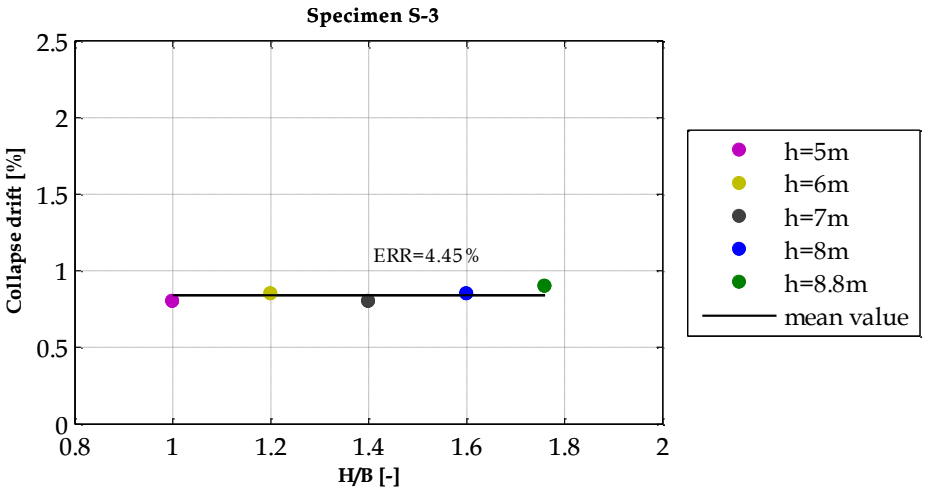

Figure 4.19 - Collapse drift vs H/B ratio for partition S-3

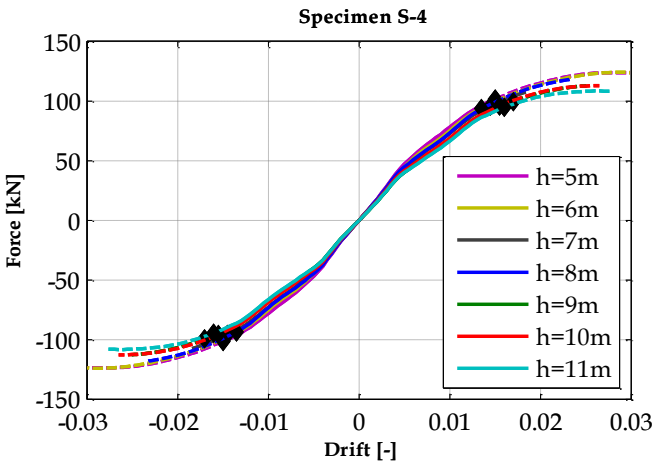

Figure 4.20 - Force vs drift pushover curve for S-4 partition at different heights

Specimen S-4		
Heights	**Horizontal joints number**	**Collapse drift**
[m]	*[-]*	*[%]*
5	1	1.60
6	2	1.60
7	2	1.50
8	3	1.40
9	3	1.80
10	3	1.60
11	4	1.70
mean value		**1.6±0.11**

Table 4.6 - Collapse drift of S-4 partition for different heights

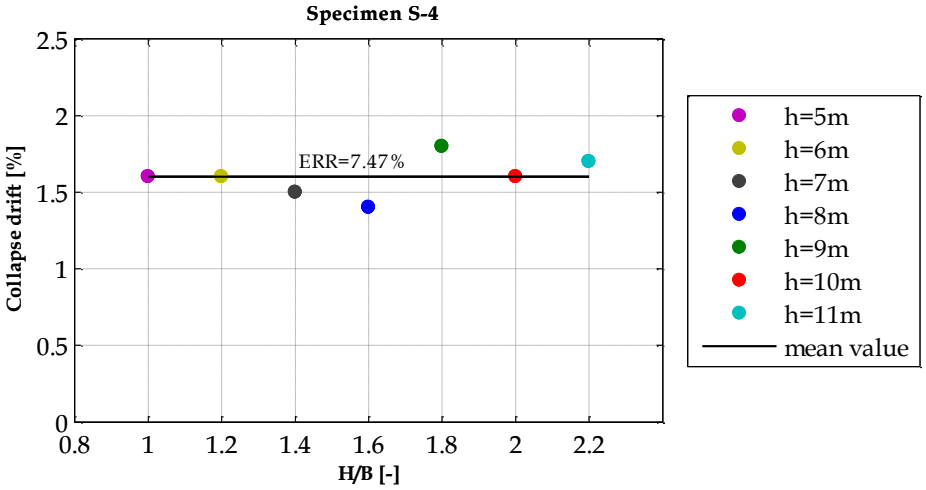

Figure 4.21 – Collapse drift vs H/B ratio for partition S-4

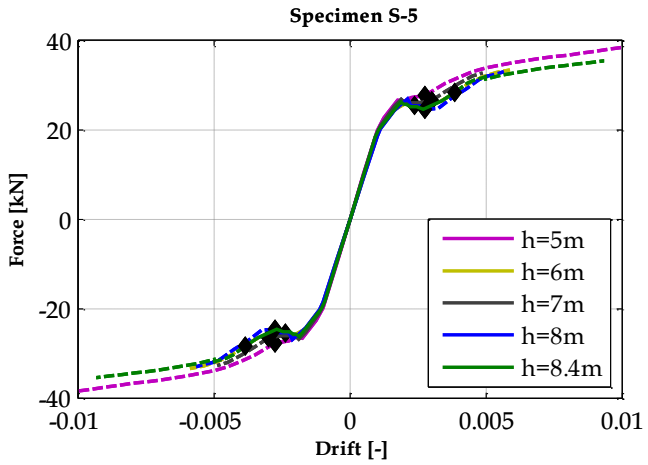

Figure 4.22 - Force vs drift pushover curve for S-5 partition at different heights

Specimen S-5		
Heights	**Horizontal joints number**	**Collapse drift**
[m]	*[-]*	*[%]*
5	1	0.35
6	2	0.26
7	2	0.35
8	3	0.33
8.4	3	0.46
mean value		**0.35±0.06**

Table 4.7 – Collapse drift of S-5 partition for different heights

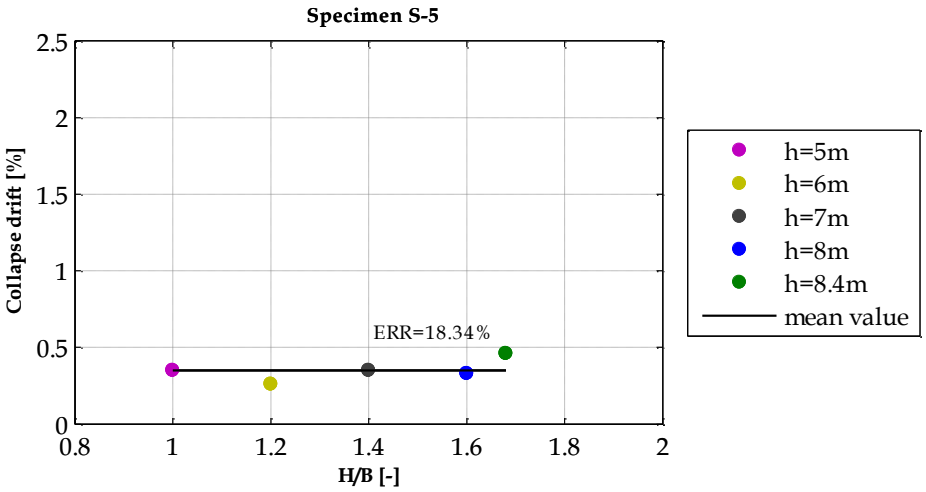

Figure 4.23 – Collapse drift vs H/B ratio for partition S-5

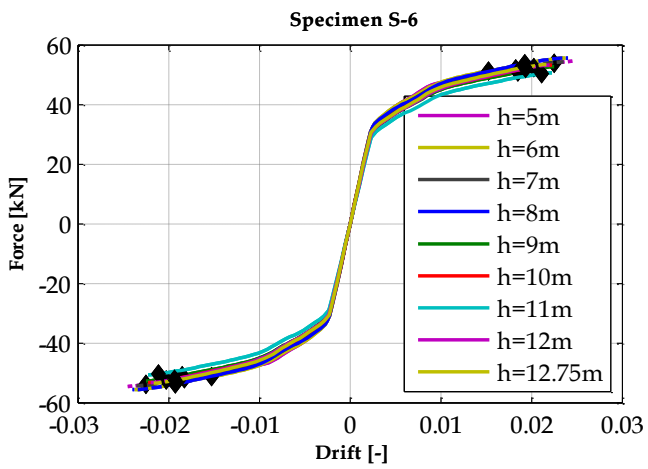

Figure 4.24 – Force vs drift pushover curve for S-6 partition at different height

Specimen S-6		
Heights	**Horizontal joints number**	**Collapse drift**
[m]	*[-]*	*[%]*
5	1	2.30
6	2	1.60
7	2	1.90
8	3	2.00
9	3	1.90
10	3	2.10
11	4	2.20
12	4	2.00
12.75	4	2.00
mean value		**2.00±0.18**

Table 4.8 – Collapse drift of S-6 partition for different heights

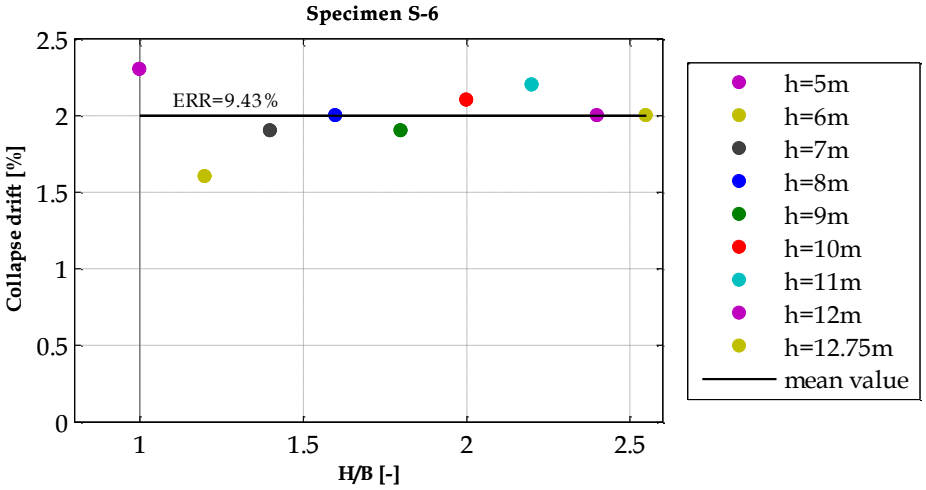

Figure 4.25 – Collapse drift vs H/B ratio for partition S-6

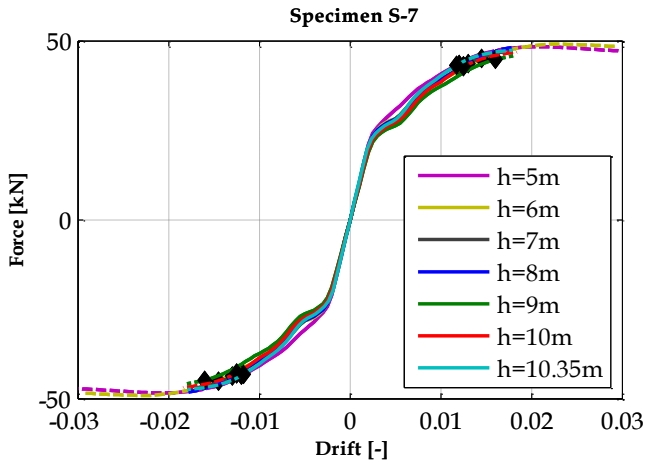

Figure 4.26 - Force vs drift pushover curve for S-7 partition at different height

Specimen S-7		
Heights	**Horizontal joints number**	**Collapse drift**
[m]	*[-]*	*[%]*
5	1	1.30
6	2	1.50
7	2	1.40
8	3	1.30
9	3	1.60
10	3	1.30
10.35	3	1.30
mean value		**1.38±0.11**

Table 4.9 - Collapse drift of S-7 partition for different heights

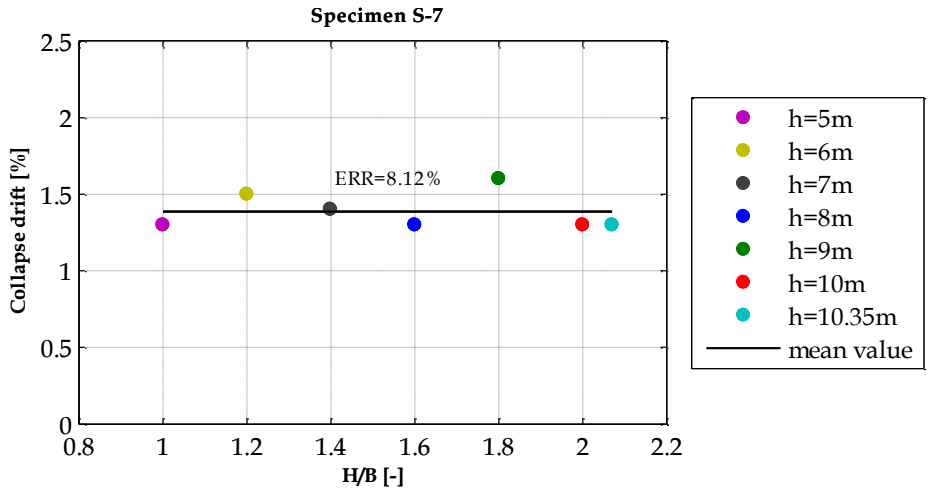

Figure 4.27 – Collapse drift vs H/B ratio for partition S-7

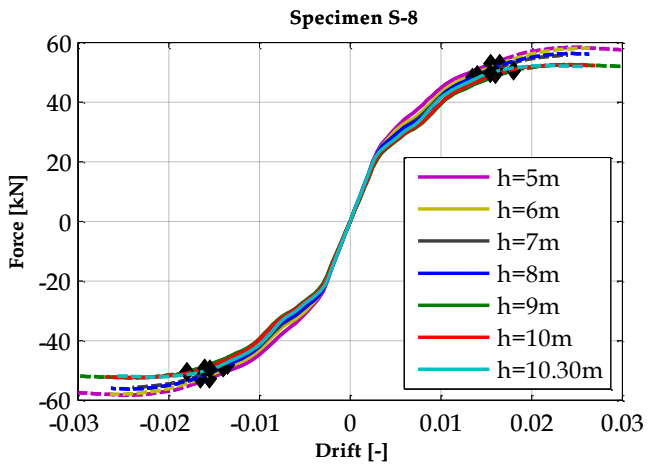

Figure 4.28 - Force vs drift pushover curve for S-8 partition at different height

Specimen S-8		
Heights	**Horizontal joints number**	**Collapse drift**
[m]	*[-]*	*[%]*
5	1	1.60
6	2	1.70
7	2	1.40
8	3	1.40
9	3	1.90
10	3	1.60
10.3	3	1.70
mean value		**1.61±0.16**

Table 4.10 - Collapse drift of S-8 partition for different heights

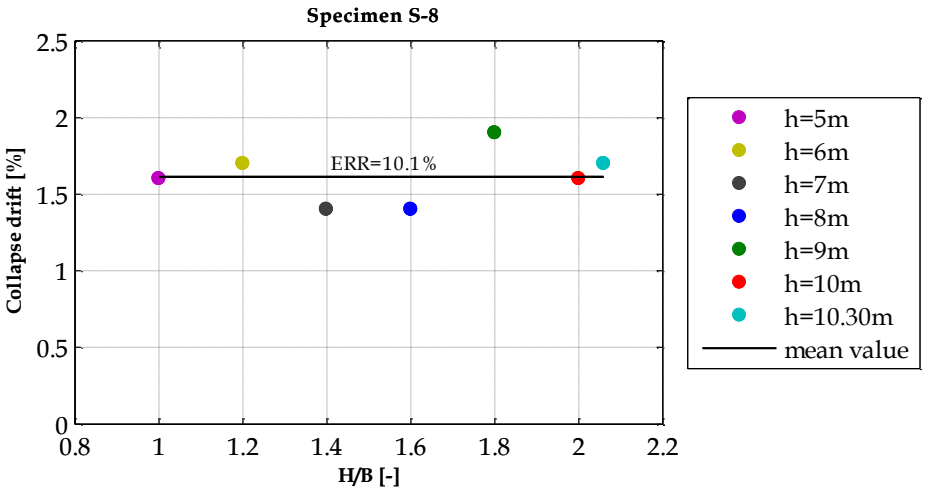

Figure 4.29 – Collapse drift vs H/B ratio for partition S-8

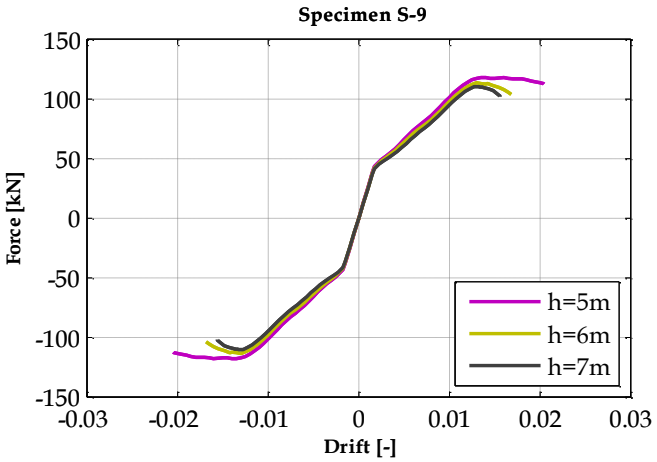

Figure 4.30 - Force vs drift pushover curve for S-9 partition at different height

Specimen S-9		
Heights	**Horizontal joints number**	**Collapse drift**
[m]	*[-]*	*[%]*
5	1	> 2.0
6	2	> 1.7
7	2	> 1.6

Table 4.11 - Collapse drift of S-9 partition for different heights

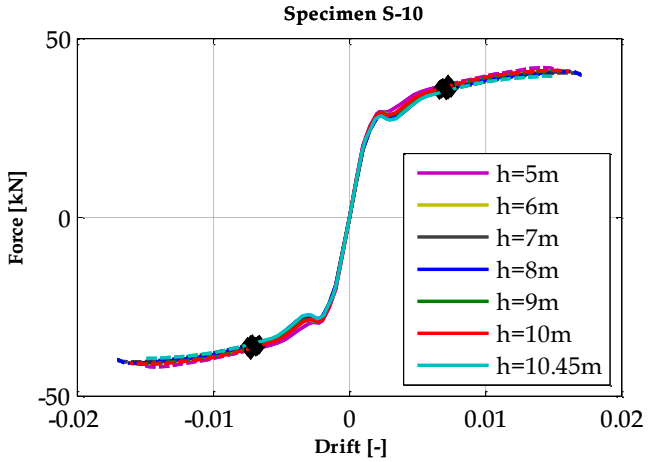

Figure 4.31 - Force vs drift pushover curve for S-10 partition at different height

Specimen S-10		
Heights	**Horizontal joints number**	**Collapse drift**
[m]	*[-]*	*[%]*
5	1	0.78
6	2	0.71
7	2	0.78
8	3	0.80
9	3	0.73
10	3	0.74
10.45	4	0.80
mean value		**0.76±0.03**

Table 4.12 - Collapse drift of S-10 partition for different heights

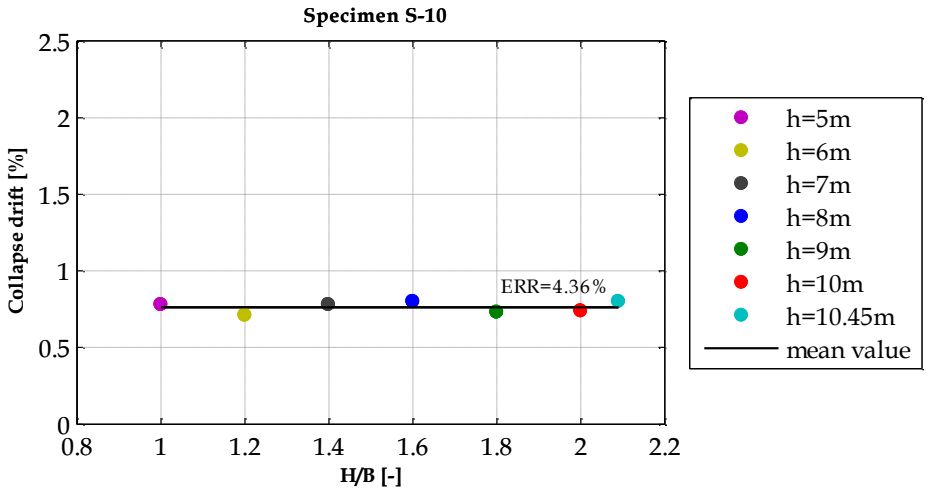

Figure 4.32 – Collapse drift vs H/B ratio for partition S-10

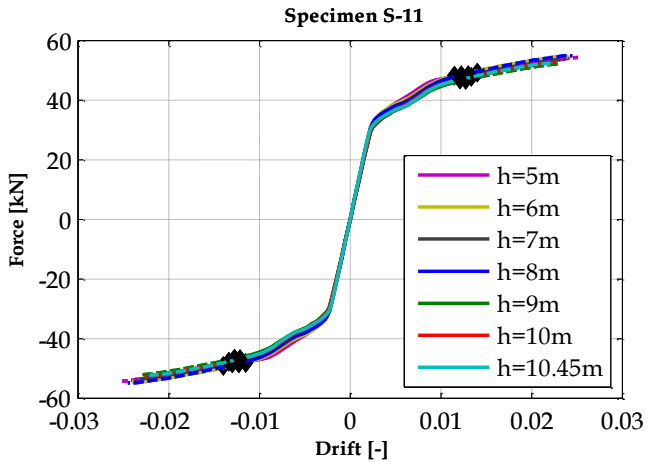

Figure 4.33 – Force vs drift pushover curve for S-11 partition at different height

Specimen S-11		
Heights	**Horizontal joints number**	**Collapse drift**
[m]	*[-]*	*[%]*
5	1	1.40
6	2	1.20
7	2	1.40
8	3	1.30
9	3	1.30
10	3	1.40
10.45	4	1.30
mean value		**1.61±0.16**

Table 4.13 – Collapse drift of S-11 partition for different heights

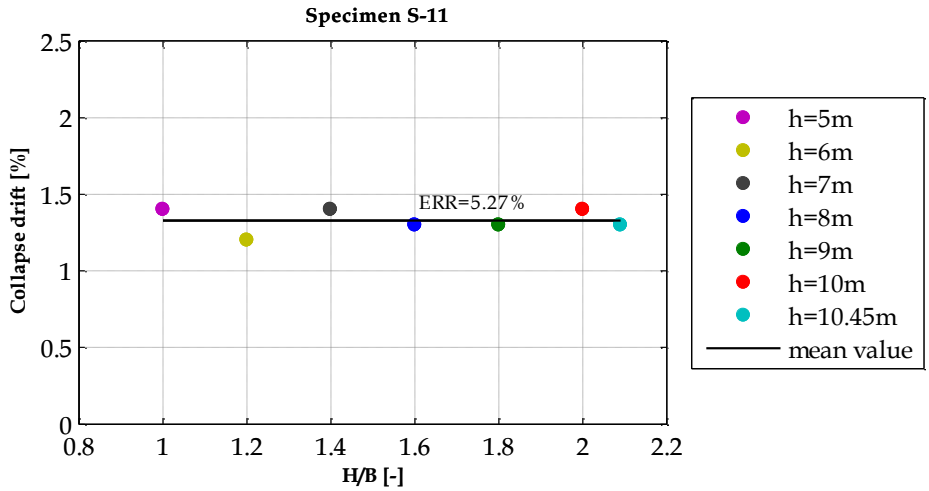

Figure 4.34 - Collapse drift vs H/B ratio for partition S-11

4.4 Influence of the partitions width on the collapse drift

Some of the specimens of Table 4.1 are further analyzed in order to evaluate the influence of partitions width on collapse drift. For each partition a constant height, i.e. equal to the maximum height (see last column of Table 4.1) is considered. Starting from a 3 meters value, the width is increased up to obtain a width-height ratio equal to two. The analyzed partitions are listed in Table 4.14.

Partition Code	Investigated widths *[m]*	No. of partitions
S-1	3-4-5-6-7-8-12-16	8
S-3	3-4-5-6-7-8-12-16	8
S-4	3-4-5-6-7-8-12-16-22	9
S-6	3-4-5-6-7-8-12-16-25.5	9
S-7	3-4-5-6-7-8-12-16-21	9
S-8	3-4-5-6-7-8-12-16-21	9
S-11	3-4-5-6-7-8-12-16-22	9
	TOTAL	**61**

Table 4.14 - Investigated width for each specimen

Each specimen is subject to nonlinear static analysis in displacement control and the results are show in terms of force versus drift pushover curve. The Schafer method is used as a posterior checking method by comparing the internal stresses, in terms of axial force and bending moment acting on the stud, to the limit domain identifying the occurrence of global instability failure. The drift corresponding to the global instability of the first stud is considered as failure drift for the whole analyzed partition (see §3.3.1). A black dot on the pushover curve points out the collapse drift achievement.

The analyses results (Figure 4.35, Figure 4.37, Figure 4.39, Figure 4.41, Figure 4.43, Figure 4.45, Figure 4.47) highlight that for each partition system a stiffness and a strength increase is recorded with the width increase, while the collapse drift gradually decreases, resulting in a less ductile behavior.

For each specimen a cubic decreasing trend of the collapse drift is identified, as depicted in Figure 4.36, Figure 4.38, Figure 4.40, Figure 4.42, Figure 4.44, Figure 4.46 and Figure 4.48, even if a unique decreasing low cannot be identified for all the analyzed specimens. It is noteworthy that for all the specimens the collapse drift becomes stable for a width - height ratio equal or larger than 1.5.

The analysis results also show that the most loaded stud is the external one on the opposite side with respect to the force application (see black circle in Figure 4.49). Furthermore, the stiffness of the partition increases as the width/height ratio increases. Then, as this ratio increases, the furthest stud, at a given displacement, is more loaded, and, consequently, its failure due to global instability occurs for inter-story drift values that gradually decrease.

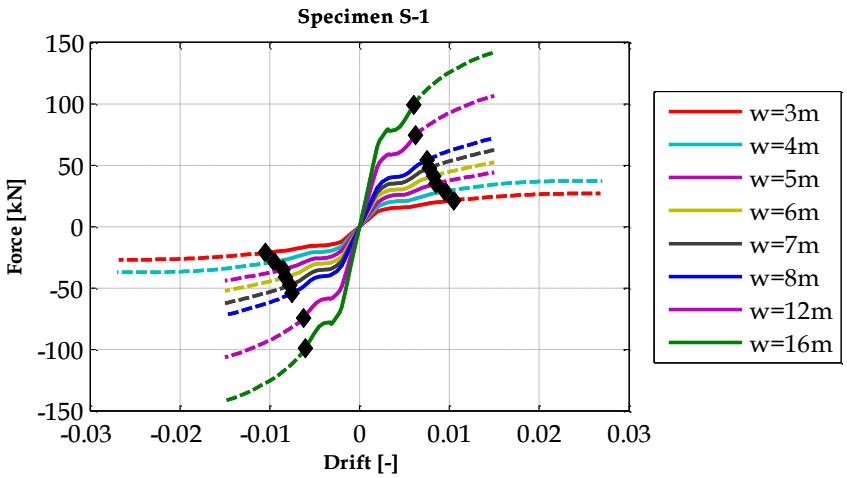

Figure 4.35 – Force vs drift pushover curve for S-1 partition at different widths

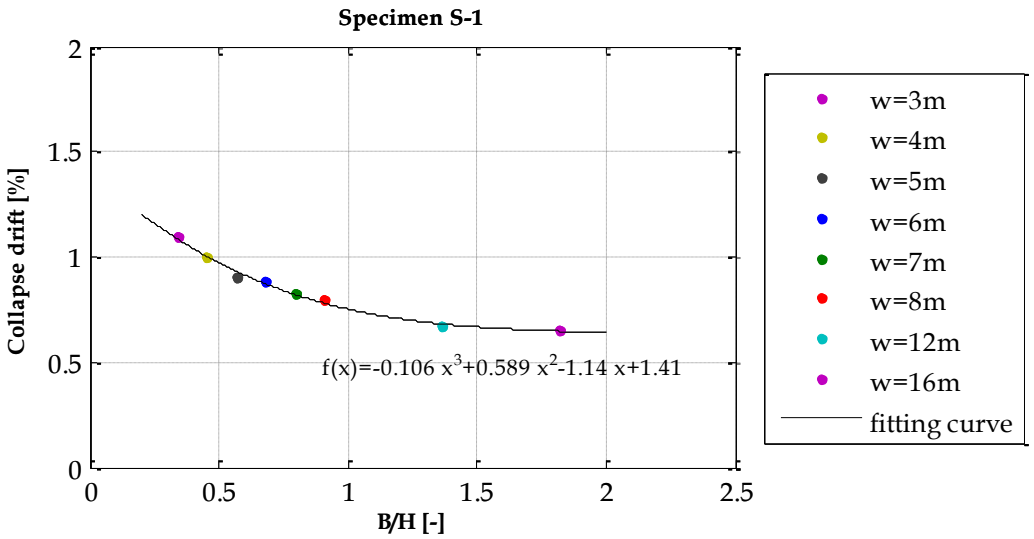

Figure 4.36 – Collapse drift versus width-height ratio for specimen S-1

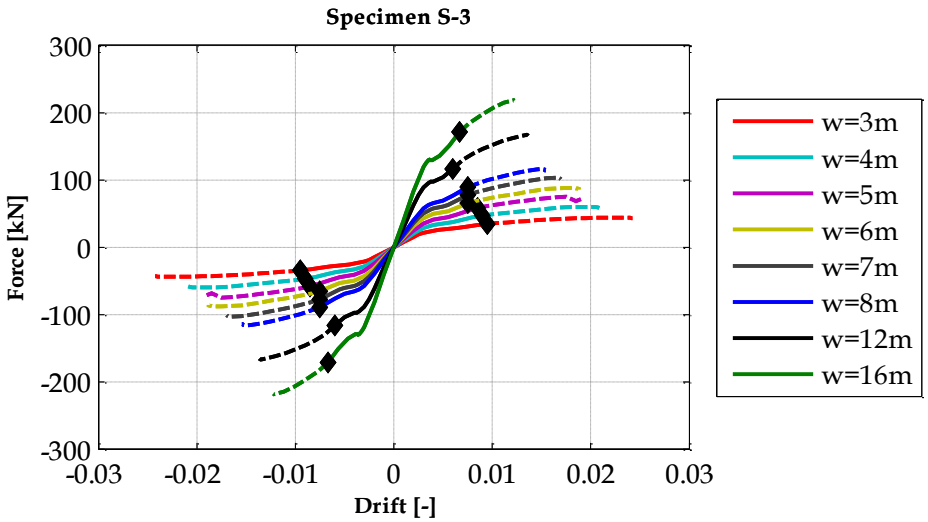

Figure 4.37 - Force vs drift pushover curve for S-3 partition at different widths

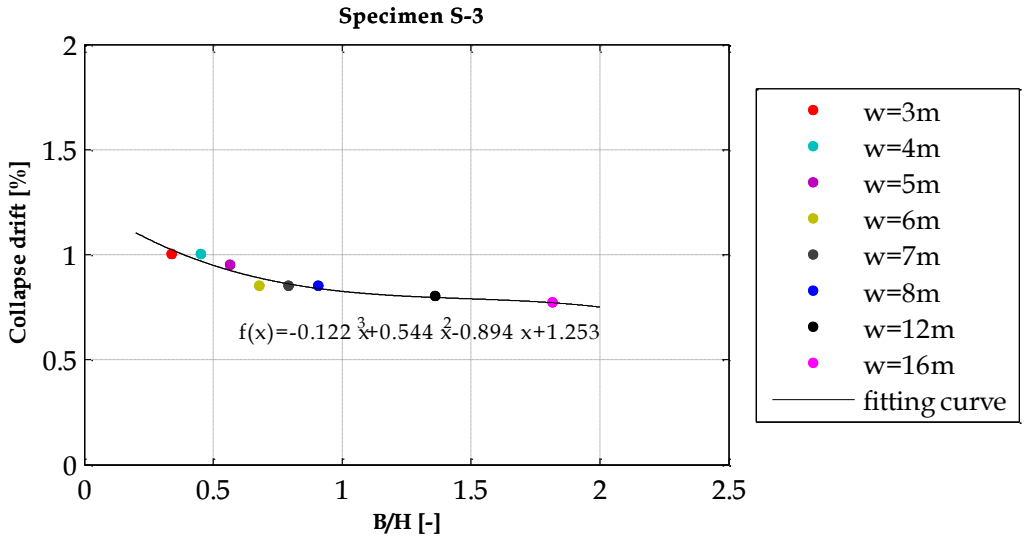

Figure 4.38 – Collapse drift versus width-height ratio for specimen S-3

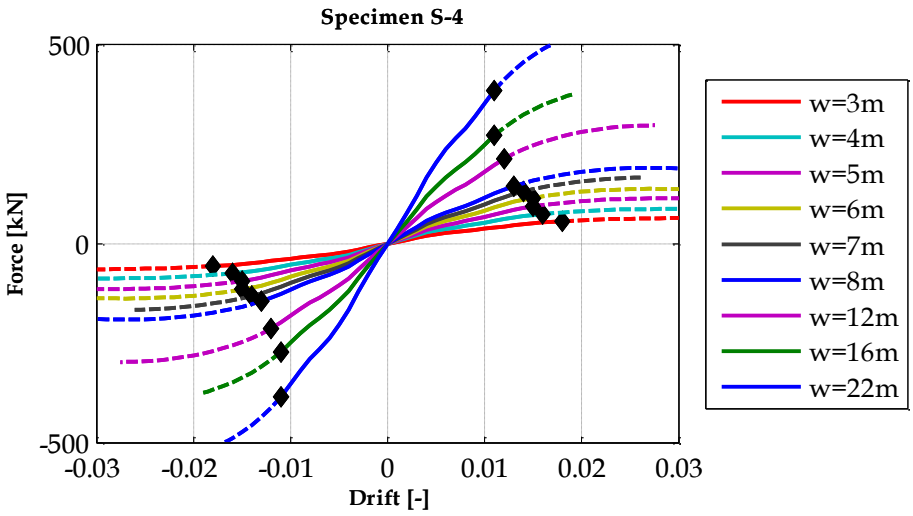

Figure 4.39 - Force vs drift pushover curve for S-4 partition at different widths

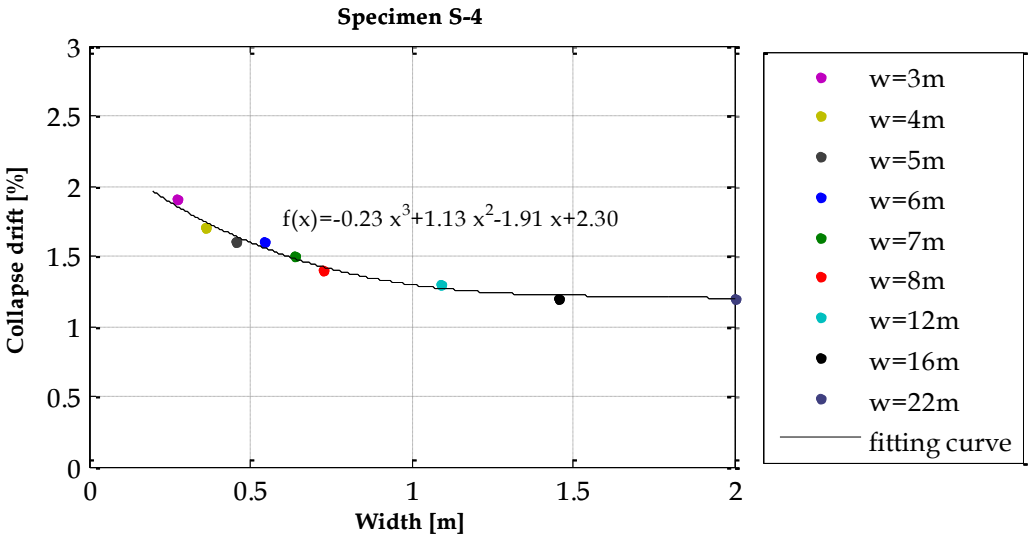

Figure 4.40 - Collapse drift versus width-height ratio for specimen S-4

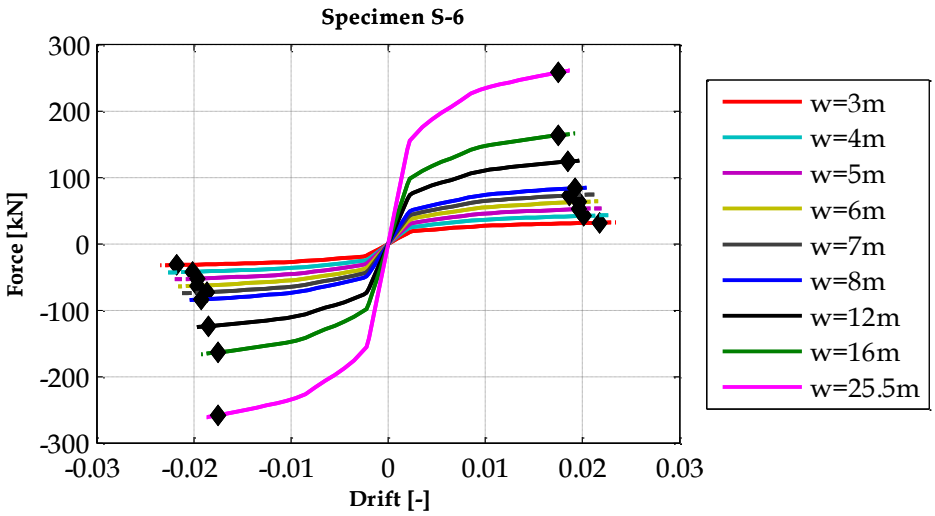

Figure 4.41 - Force vs drift pushover curve for S-6 partition at different widths

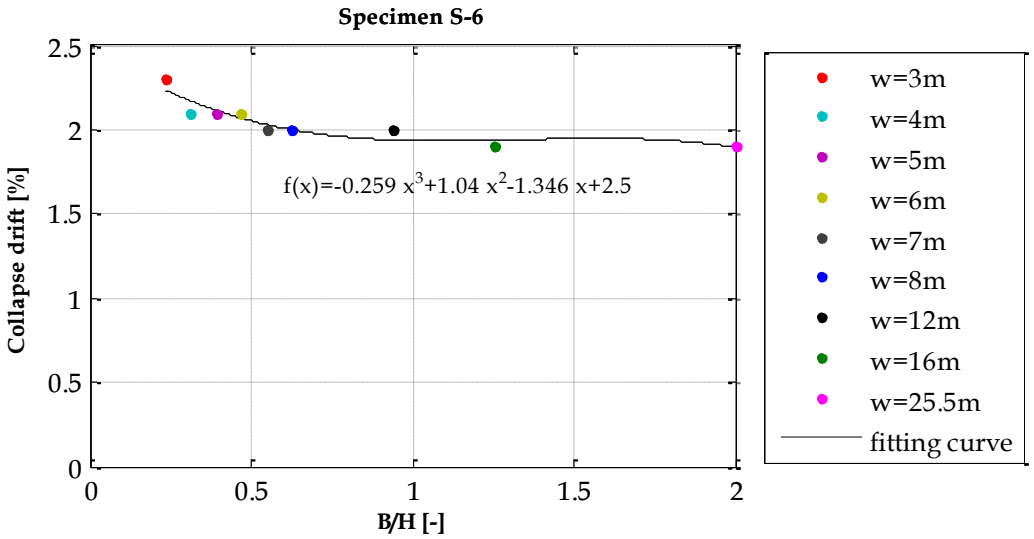

Figure 4.42 - Collapse drift versus width-height ratio for specimen S-6

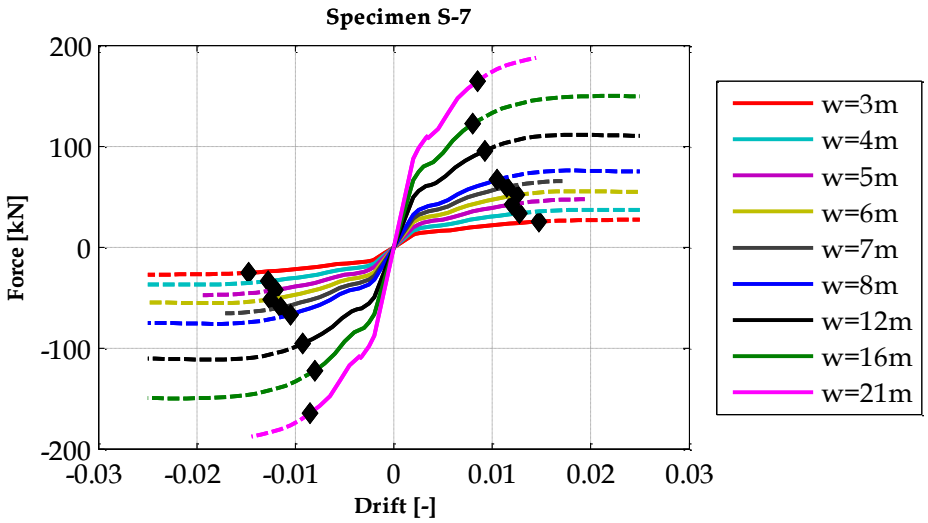

Figure 4.43 - Force vs drift pushover curve for S-7 partition at different widths

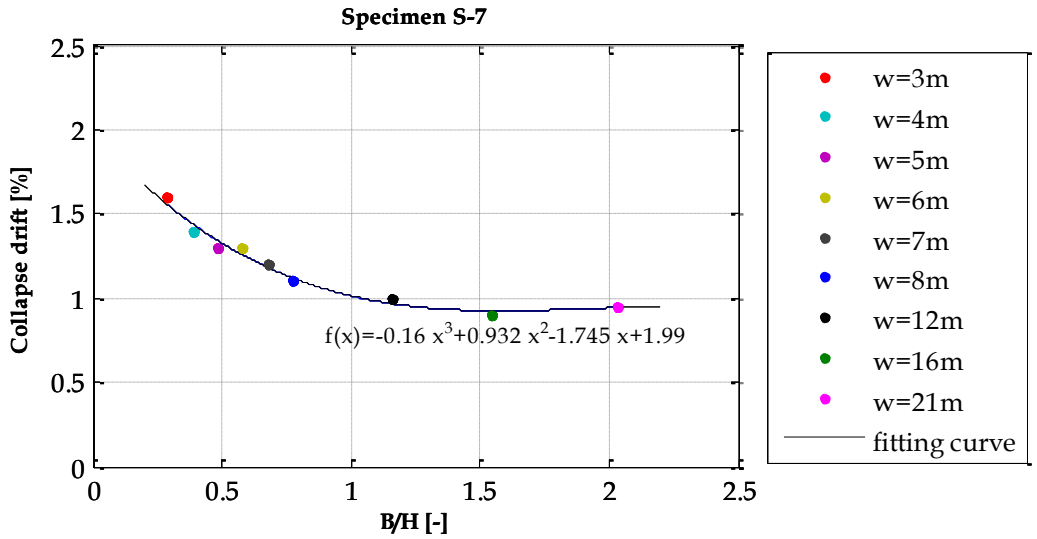

Figure 4.44 - Collapse drift versus width-height ratio for specimen S-7

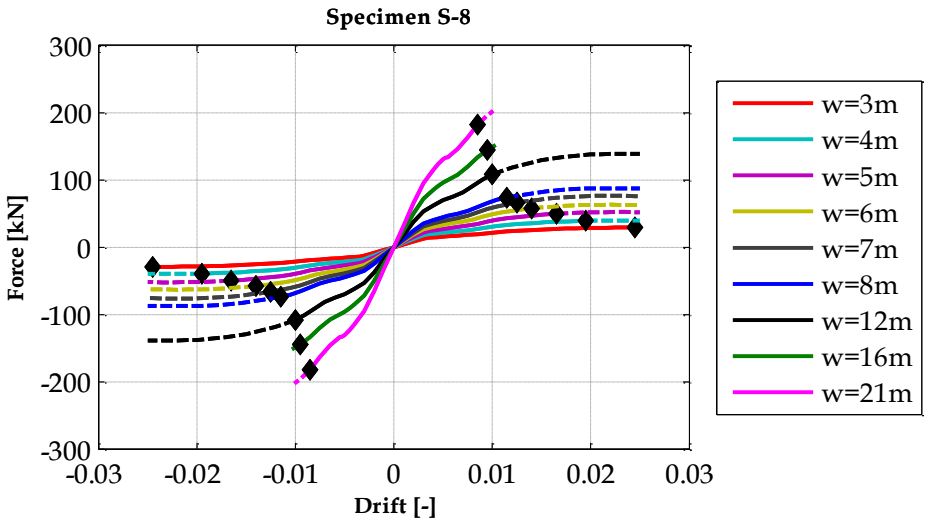

Figure 4.45 - Force vs drift pushover curve for S-8 partition at different widths

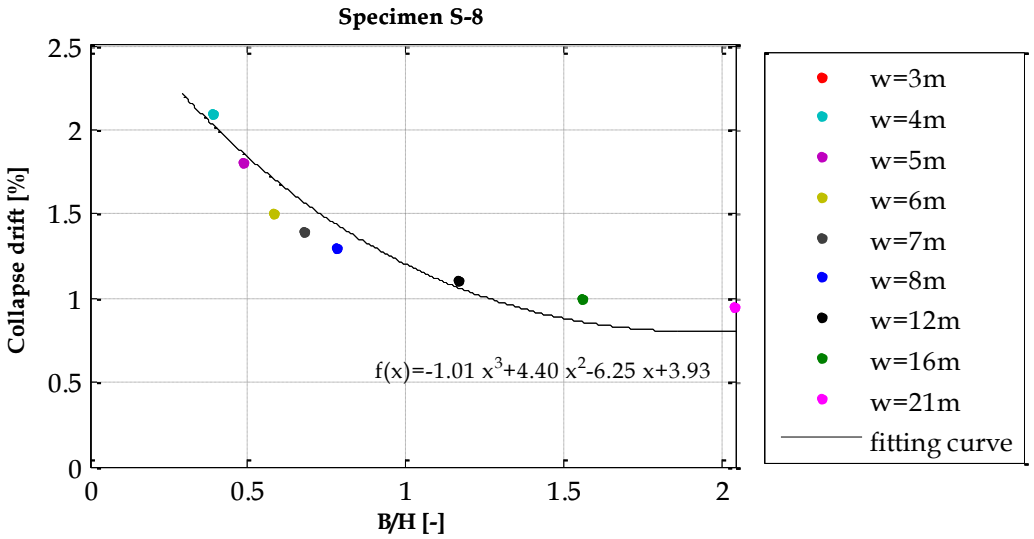

Figure 4.46 - Collapse drift versus width-height ratio for specimen S-8

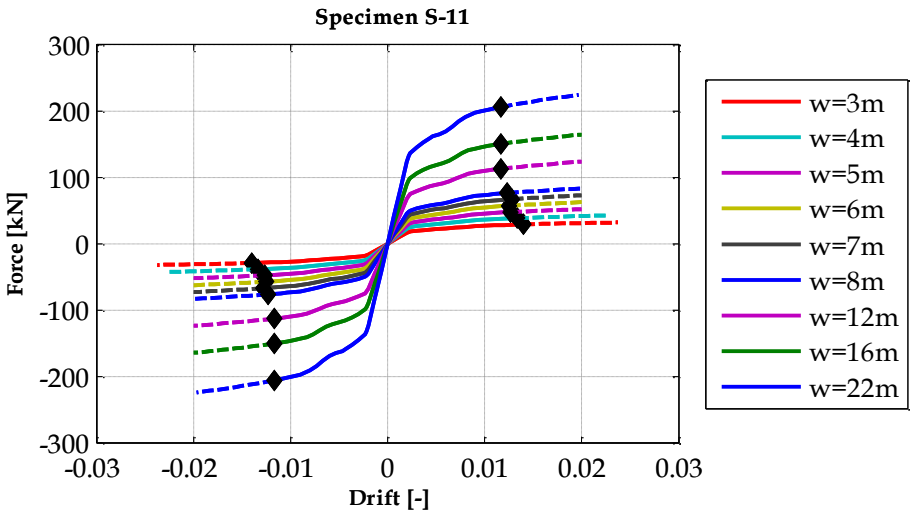

Figure 4.47 - Force vs drift pushover curve for S-11 partition at different widths

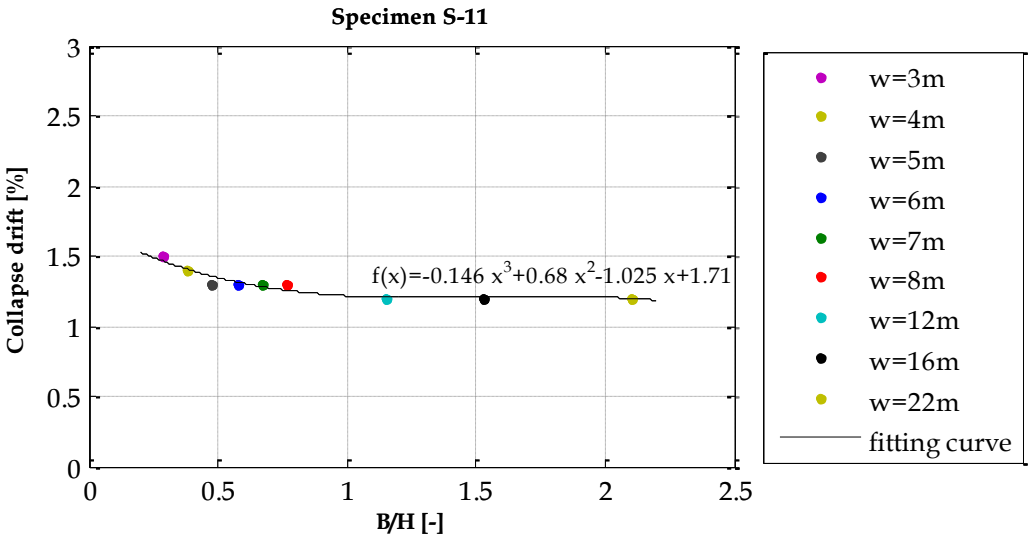

Figure 4.48 - Collapse drift versus width-height ratio for specimen S-11

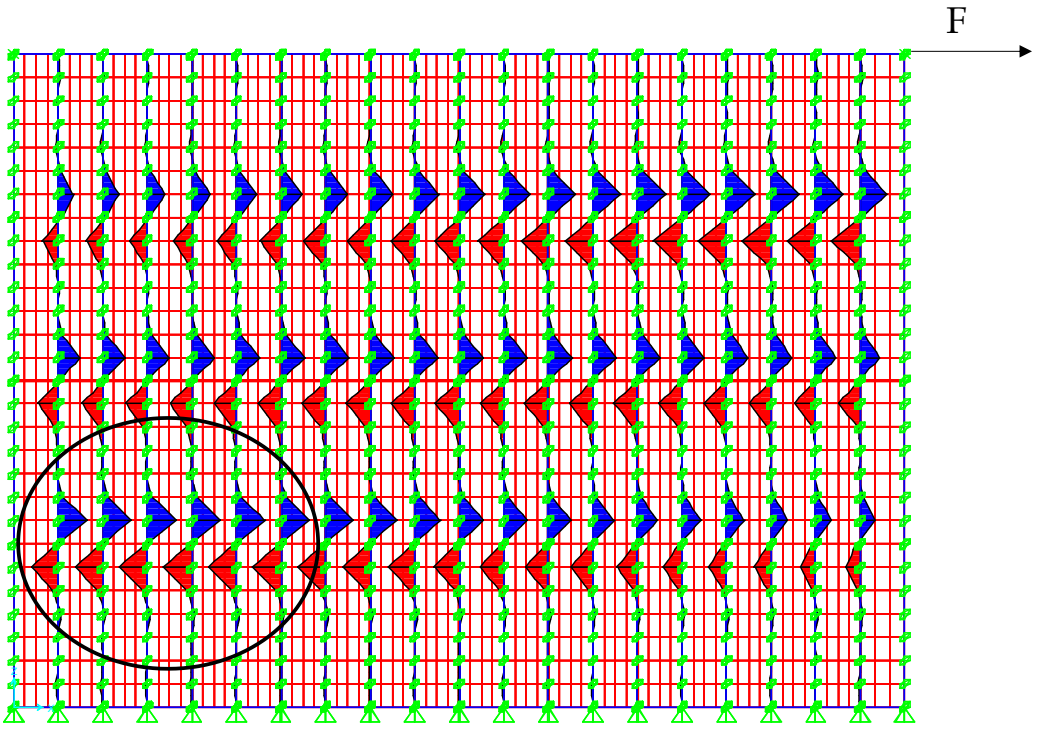

Figure 4.49 – Bending moment distribution on a generic specimen with B/H larger than 1

Chapter 5

INNOVATIVE MATERIAL FOR ANTISEISMIC PARTITIONS AND INFILLS

Nowadays, new materials are studied and introduced in civil engineering in order to improve the seismic performance of nonstructural components. The plasterboard internal partitions, presented in the previous chapters, provide a valuable example in this direction. Nevertheless, this typology is largely employed in industrial and commercial buildings. For residential applications several materials are now available to replace the classic brick, widely used for many years. For instance, cellular concrete blocks are becoming common both for internal partitions and for external infill for their light weight and appreciable mechanical properties. The material lightweight is largely considered the key issue in order to reduce the inertial forces acting on the nonstructural component during an earthquake, due to its own mass. Actually, this aspect is related to the nonstructural component out of plane behavior, since a reduced mass imply a less intense inertial force acting in the out of plane direction, which causes the partition overturn. Not always, the lightweight is associated with the capacity to accommodate the in plane deformation of the main structure. Indeed, these nonstructural components are required to exhibit in-plane ductile behavior for high deformation values. Moreover, the partitions and the infill are required to have good properties in terms of thermal and acoustic insulation, permeability to water vapor and, in some specific cases, fire resistance.

Recently, a new hybrid material based on the conjunct use of polyurethane and cement was introduced (Iannace et al., 2008) in order to obtain an innovative material able to meet the requirements of lightness, high deformability and ductility, but also of thermal and acoustic features, by combining the features of these two components.

Polyurethanes foams are widely used in in the construction industry for their thermal and acoustic insulation properties, although they are characterized by low strength and stiffness. Common method of increasing the foam stiffness consists of filling the polymeric matrix with a rigid phase: glass fiber, nylon fiber, silicon dioxide powder and aluminum powder are example of fillers. Despite the strengthening effect of the infill, several studies (Yang et al., 2004) pointed out the problem of adhesion between the polymeric matrix and the filler, resulting in a brittle overall behavior.

Cement represents the most widely used structural material but the low failure strain, the low acoustic and thermal properties and the susceptibility to frost damage make this material unsuitable for nonstructural component applications.

The combined use of a polymeric foam and the hydrated cement can represent a methodology for optimizing these two components and at the same time producing a lightweight material. The material is conceived so that the inorganic and the organic phases are co-continuous throughout the material and the phases are intimately dispersed within each other. In this way, the system is designed to meet both the advantages of the polyurethane foam and the inorganic binder.

Previous studies (Verdolotti et al., 2010, Verdolotti et al., 2008, Verdolotti et al., 2012, Verdolotti et al., 2013), evidenced the thermal and acoustic insulation properties of the material, besides the water vapor permeability and the fire resistance. All of these aspects are suitable for infill or partition system applications. Furthermore, the hybrid material shows good adhesion properties to concrete and mortar typical of inorganic binder cement.

In this chapter, the mechanical characterization of the material is presented in terms of compressive, tensile and shear strength properties, in order to investigate the possible application in the civil building field for nonstructural components purpose.

5.1 The hybrid polyurethane - cement foam

5.1.1 Samples preparation

Portland cement (CEM type IIA-S class 42,5R) was supplied by Cementir S.p.A. (Spoleto, Italy). Polyether and toluene di-isocyanate (TDI) were supplied by Bayer (Deltapur S.p.A., Bergamo, Italy) and were used as received. According to the producer's specifications, the polyether/TDI ratio was 1: 1.2 to achieve an open-cell, flexible foam. Distilled water was used to control foaming.

Samples were prepared by mixing at room temperature the cement powder to the polyol with catalysts, silicone surfactant, chain extenders and water as blowing agent. This mixture was stirred mechanically for 2 minutes and then MDI was added and mixed for 40 seconds. Mixing was performed according to ASTM C305, by a Hobart mixer (mod. N50, Hobart, Canada). According to Iannace et al., 2008, the polyurethane/cement weight ratio was fixed to 2/3. After mixing all of the components, the mixture was poured in a wood closed mold (50x50x5cm^3) and the foam was allowed to expand/cure for 20 minutes at room temperature. The samples were then removed from the mold and cured in water, for 72 hours at 60°C, to allow for the hydration of cement powder.

5.1.2 Chemical, physical and morphological properties of the hybrid foam

Several functional properties of interest in the building field, such as thermal insulating properties, acoustic insulation and absorption properties, water vapor transmission, and dimensional stability are herein reported. The hybrid foam sample are subjected to several tests in order to identify specific parameters. Verdolotti et al. (2012) details the experimental campaign and the reference test methods. Here the results of these tests are listed to have a whole overview of the polyurethane cement foam physical features.

The water vapor transmission properties were analyzed according to UNI EN 12086. The μ parameter, a non-dimensional property quantifying the relative water vapor diffusion resistance of the material, was evaluated. In Table 5.1 the μ value of the hybrid foam is compared to that of the neat polyurethane (Neat PUR). The water vapor diffusion resistance of Neat PUR is very high, making this material unsuitable for application in building. Of course, the high resistance to water transport exerted by Neat PUR is due to its hydrophobic nature and the closed-celled pore structure.

Sample	μ
Neat PUR	90
HIP_C	32

Table 5.1 - Water vapor transmission resistance of selected samples

When the hydrophilic component (cement) was added to the hydrophobic polyurethane matrix to form the hybrid foam (HIP_C), a reduction of μ of ca. 65% is observed. It is worth of note, that the value of 32 for the water vapor transmission resistance of the HIP_C sample is quite similar to the ones of intrinsically hydrophilic materials utilized in building. This relevant decrease of the water vapor transmission resistance could be ascribed to the formation of the co-continuous cement phase within the polyurethane matrix as a consequence of the hydration reaction. The co-continuity, in turn, determined the occurrence of a path, accessible to water molecules, percolating throughout the hybrid.

Thermal conductivity was measured according to ASTM C518-04. The results of the thermal conductivity tests performed on Neat PUR, and the hybrid systems are reported in Table 5.2. As it was expected, the results show typical values for insulating materials in the case of the neat polyurethane systems having the lowest densities with a decrease of the insulating performances for the hybrid foam.

Sample	λ *[W/m K]*
Neat PUR	0.028
HIP_C	00.06

Table 5.2 - Thermal insulating properties of Neat PU and the hybrid foams

This result is reasonable in view of the relative higher amount of conducting solid phase in higher density hybrids. However, the absolute values are still lower than that of the traditional lightweight concrete commonly used as insulator (i.e., 0.12 W/m K) (Sarier and Onder, 2008).

Acoustic insulation properties (transmission loss - TL) for selected samples were measured according to UNI EN ISO 11654-717. Sound absorption is the characteristic of a material to be able to convert the acoustic energy of sound waves into another form. The sound absorption coefficient, α, is the absorbed fraction of incident wave energy. Typically, open-celled foams, such as flexible polyurethane foam, are good sound absorption materials. Open-celled foams, in fact, capture and absorb the sound waves because the waves dissipate their energy through friction. In particular, it is noted [18] that the sound absorption of flexible polyurethane

foams is high in high-frequency regions, but relatively weak in low frequency (100–1,000 Hz) regions, where, unfortunately, the human sensitivity is high (Bo et al., 2007). As reported in literature, in fact, to improve the acoustic performances at low frequencies, typically, the foams are loaded with fillers in powder form. Closed-celled foams conversely, typically characterize rigid hybrid systems, as the hybrid foam here presented, and, for this reason, they do not perform well in sound absorption.

Dimensional stability of the hybrid foam is also assessed. This feature is important for use in building field, where materials have to withstand different thermal and humidity conditioning during service of several tens of years. Dimensional stability has been measured using ASTM D2126, which is specific for rigid cellular materials. The test results on the proposed hybrid foams showed a very good dimensional stability with dimensional changes, Δl (%), in the x, y, and z axes for the different conditioning conditions always below 0.3 %. It is worth of note that this value is one order of magnitude lower than expanded polystyrene foams typically utilized as insulating panels in building.

5.2 Mechanical characterization on the hybrid foam

Chemical, physical, and morphological characterization of hydrated samples, are synthetically listed in §5.1.2. Here, we focus on specific mechanical properties, namely, compression, tension, and shear, which have been performed according to ASTM International standard as detailed in §5.2.1, §5.2.2 and §5.2.3 and in Coppola et al. (2015). The standards were selected on the base of the material chemical composition and structure.

5.2.1 Compressive tests

The compressive properties of the hybrid polyurethane cement foam were evaluated by testing the material according to ASTM D1621-00 (2003) - standard test method for compressive properties of rigid cellular plastic. As reported in the test standard, each specimen should have a cross section area of $25.8 \cdot 10^3$ mm^2 as a minimum, and $23.2 \cdot 10^5$ mm^2 as maximum. According to these conditions, five cubical specimens with a 50 mm edge (Figure 5.1b) were carefully cut from a rectangular panel of the hybrid material (Figure 5.1a).

Before testing, each sample was gauged and weighted in order to know the initial thickness and have information about the volume density (Table 5.3).

A universal electromechanical machine (INSTRON mod. 43258y234, AL, USA) was used as testing system with an automatic acquisition system (see Figure 5.2a). During the test, performed in displacement control, the crosshead rate was automatically recorded and the movement was used as measure of the specimen thickness reduction. Some creaks and drop of dust characterized the compression rupture as evidenced in Figure 5.2b. The test can be considered concluded when a 13% compression of the specimen original thickness was reached, i.e. a 6.5 mm crosshead displacement.

On the base of the experimental force-displacements curves, the maximum strength for each specimen is evaluated, as well as it is also possible to evaluate the elastic modulus in compression by considering the slope of the tangent line at the zero point of the experimental stress-strain curve.

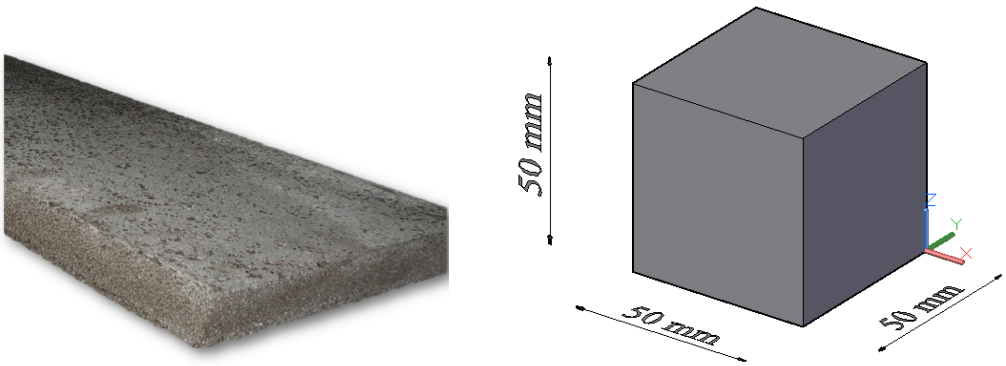

(a) (b)

Figure 5.1 – (a) Panel of the hybrid foam from which (b) cubic specimen are cut

Sample code	Volume density
[-]	*[kg/m^3]*
S1-c	278
S2-c	267
S3-c	281
S4-c	266
S5-c	265

Table 5.3 - Dimension of the cubic specimen subject to compression

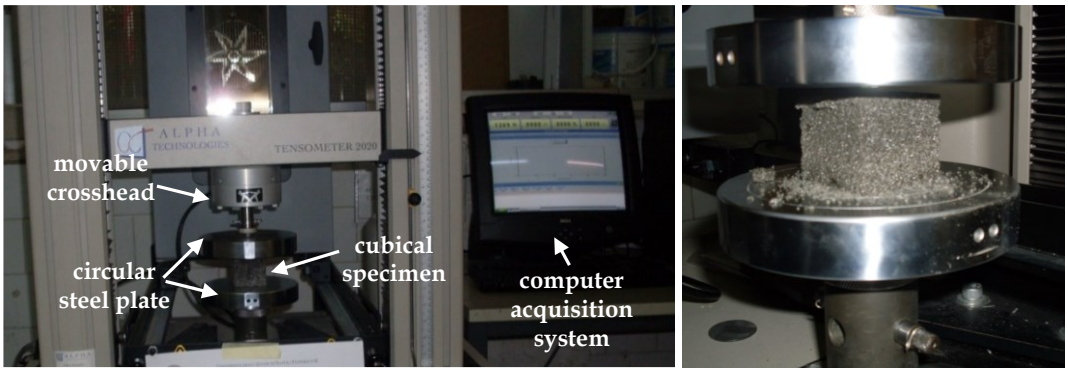

Figure 5.2 – (a) General view of the compressive test setup and (b) particular of the specimen configuration at the test end

5.2.2 Tensile tests

The ASTM-D1623-03 (2003) - standard test method for tensile and tensile adhesion properties of rigid cellular plastics - was used as reference method. According to this method, three specimens were shaped as shown in Figure 5.3. The two external conical parts of each specimen are conceived in order to connect the specimen to the testing machine; the central cylindrical portion represents the effective length to test.

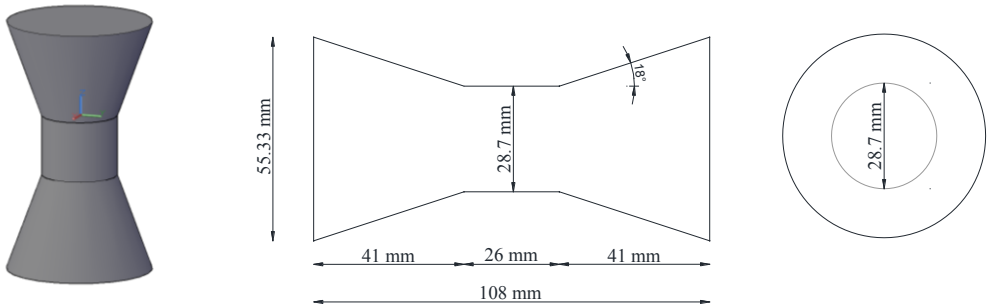

Figure 5.3 – Configuration of the specimen for tensile test

The particular tool system is conceived so that the external grip are fixed to the testing machine (Figure 5.4a), while the internal parts are used to accommodate the specimen (see Figure 5.4b) and then are inserted in the external grip for testing (Figure 5.4c). At the beginning of the test, the external grip were put close and the acquisition system is set to zero. When the test starts, the external grip were distanced with a 1.3 mm/min rate, up to the specimen failure.

The experimental stress-strain curves were obtained by dividing the recorded force by the cross sectional area of the specimen in the central portion and the recorded grip moving by the height of the central portion. The tensile elastic modulus is also evaluated, as in compression, by considering the slope of the first branch of the experimental stress-strain curve.

Sample code	**Volume density**
[-]	*[kg/m^3]*
S1-t	277
S2-t	243
S3-t	292

Table 5.4 – Volume density of the specimens subject to tensile tests

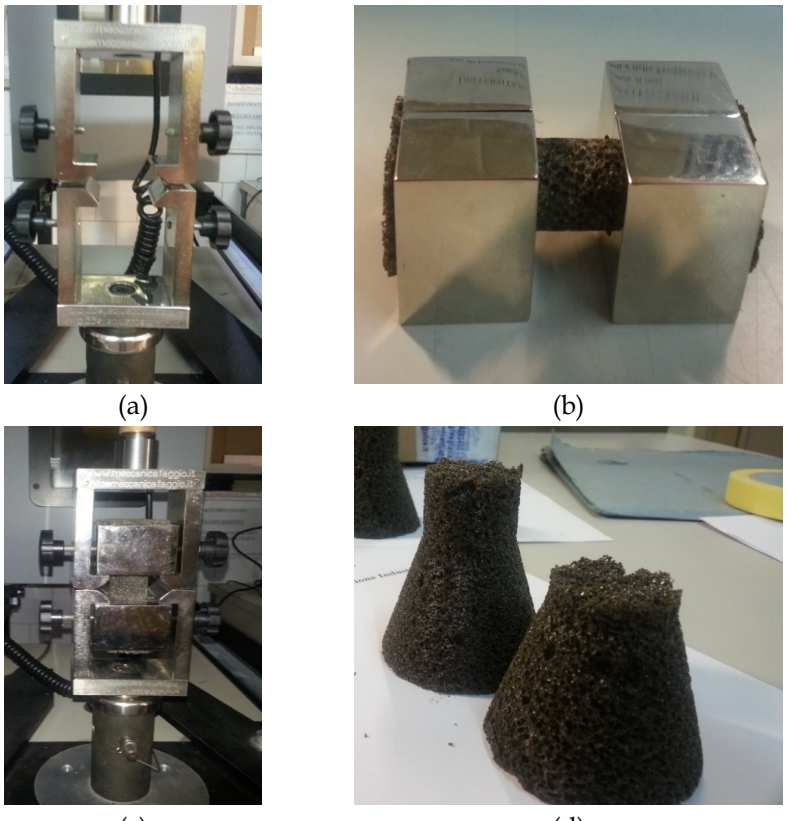

(a) (b)

(c) (d)

Figure 5.4 – (a) External grip connected to the testing machine, (b) specimen located in the internal tools, (c) complete tensile test setup and (d) failed specimen at the end of the test

5.2.3 Shear tests

The shear properties of the material are evaluated according to the ASTM-D5379 (2012) - standard test method for shear properties of composite material by V-notched beam method. Even if this method is conceived for composite materials reinforced by high-modulus fibers, the v-notch shear test was originally proposed by Iosipescu (1967) for determining the shear properties of isotropic materials such as metals. In 1983, Walrath and Adams (1983) have used it to test a wide variety of composite materials and even materials such as wood and foam. In all of these applications, the method has worked well, resulting in very reproducible results.

According to the test method, a rectangular flat strip specimen with symmetrical centrally located v-notches (Figure 5.5) is loaded in a mechanical machine by a special fixture, schematically shown in Figure 5.6.

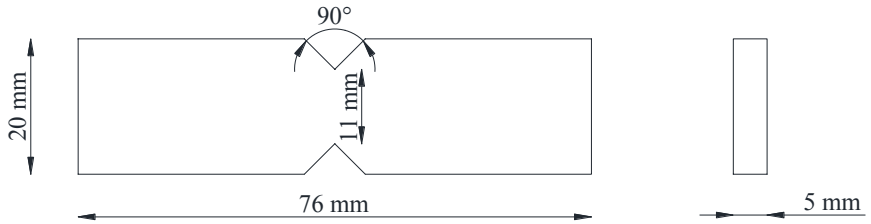

Figure 5.5 – Specimen configuration for shear tests

Three specimens were tested in order to identify the shear properties of the hybrid material. Each of them was inserted into the fixture with the v-cut located along loading axis. During the test, the relative displacement between the two fixtures halves, loaded the notched specimen. The load scheme, shown in Figure 5.7 is such that pure shear is recorded in the middle section of the specimen.

Sample code	**Volume density**
[-]	*[kg/m^3]*
S1-t	277
S2-t	243
S3-t	292

Table 5.5 - Volume density of the specimens subject to shear tests

Unlike the previous tests, in this case the grip tool movements cannot be associated to the specimens deformations, since compression forces are applied while shear properties need to be assessed. Consequently, only the shear strength can be evaluated according to the following formula:

$$\tau_{max} = \frac{F_{max}}{t \cdot l} \qquad (5.1)$$

being:

- F_{max} the peak force of each experimental curve
- t the thickness of the specimen at the v-notch;
- l the specimen with at the v-notch.

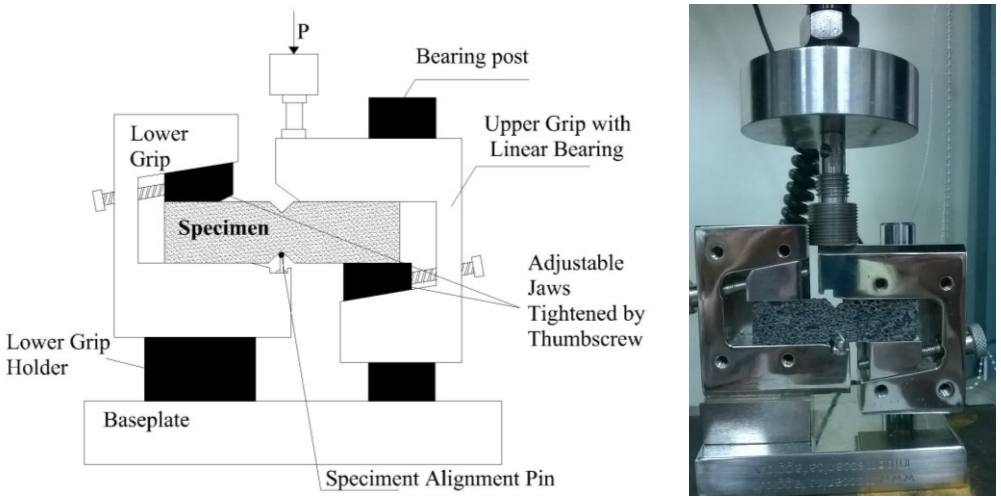

(a) (b)

Figure 5.6 – (a) Scheme of the shear test fixture with the specimen and (b) view of the complete setup during the shear test

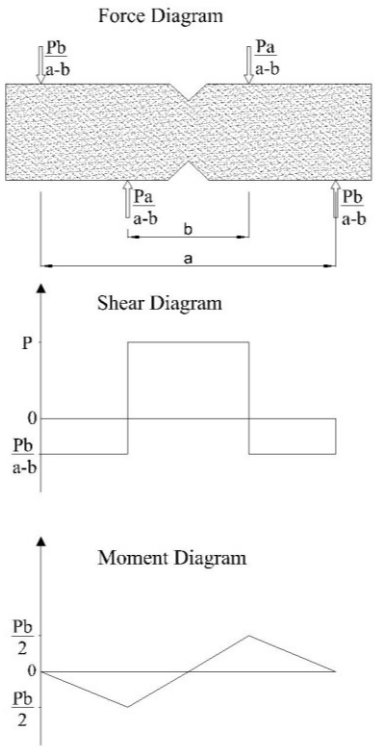

Figure 5.7 - Force, shear and moment diagrams on the specimen subject to shear test

5.2.4 Results and discussion

In this section, the results of the aforementioned tests are presented. The following tests were performed, according to ASTM standards for cellular plastic material:

- 5 compressive test on the cubical specimens, with a crosshead rate of 2.5 mm/min up to the 13% compression of the specimens original thickness;
- 3 tensile tests with a crosshead rate of 1.3 mm/min rate up to the specimens failure;
- 3 shear tests with standard head displacement rate of 2 mm/min until the specimen failure.

The Figure 5.8 shows the stress-strain curves resulting from the compressive tests; compressive strength and elasticity modulus value are listed in Table 5.6, as well. Each specimen shows an initial elastic behavior, rather linear, up to the maximum strength beyond which a steep strength reduction of 40% ca. occurs, followed by a stress increase with a pseudo-plastic behavior, i.e. the stress is almost constant while the strain increases. According to the used standard, the test was stopped at a strain of 13%, before the occurrence of the densification that is the steep

increase of the stress, typically observed at strain values of 70-80%. It should be noted from the Figure 5.9 that the maximum strength, which mean value is equal to 1.46±0.21 MPa, is reached for a 1% strain: this value is very far from the ultimate strain of the concrete (i.e.0.35 %), pointing out a highly deformable material up to the maximum strength. The stress drop observed at ca. 1% strain is due to the fragile fracture of the hybrid material forming the foam walls/struts. After the fracture of a first (weakest) horizontal section, there is a new stress buildup due to the contact of this collapsed, fractured section and the subsequent loading of the other sections, up to the next fracture. This compressive behavior should be classified as microscopically brittle and macroscopically ductile, as the overall strength remains quite constant.

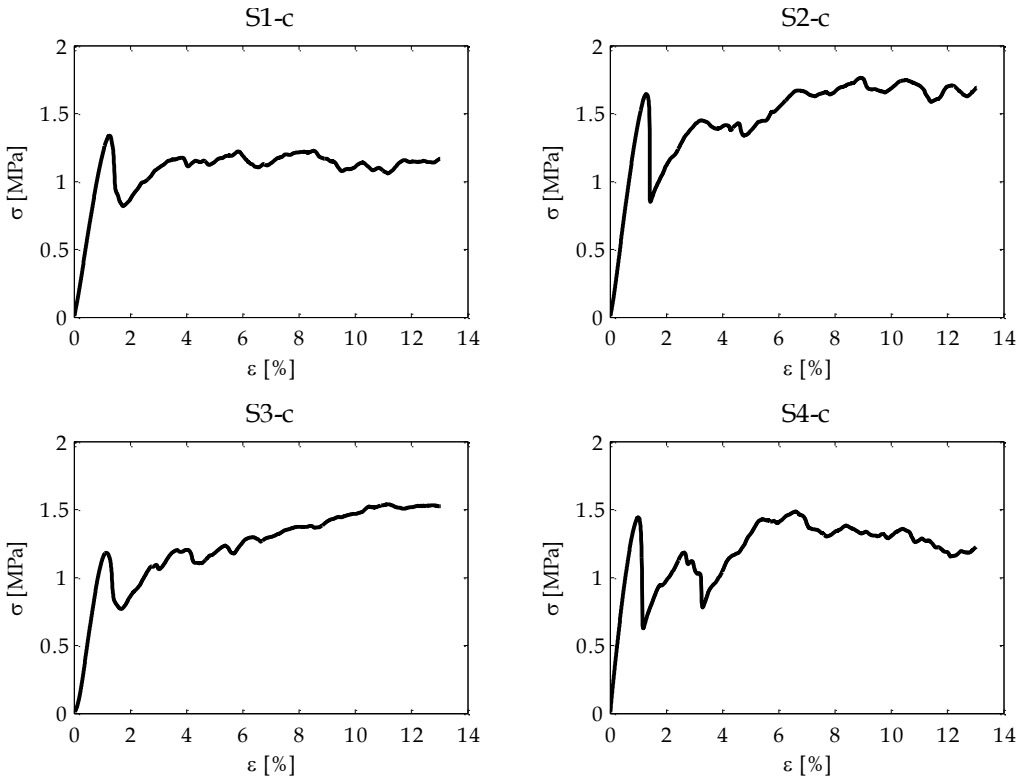

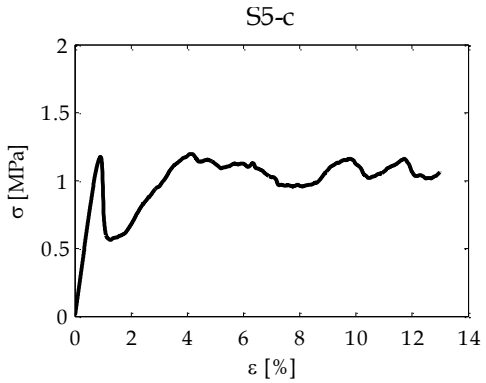

Figure 5.8 - Stress-strain curves for cubic specimen subject to compression tests

Sample code	Compressive strenght	Elasticity modulus in compression
[-]	*[MPa]*	*[MPa]*
S1-c	1.34	120.19
S2-c	1.76	144.10
S3-c	1.54	104.10
S4-c	1.46	203.20
S5-c	1.20	144.55
Mean	**1.46**	**144.23**
Standard deviation	**0.21**	**37.73**

Table 5.6 - Compressive strength and elastic modulus for each specimen including mean value and standard deviation

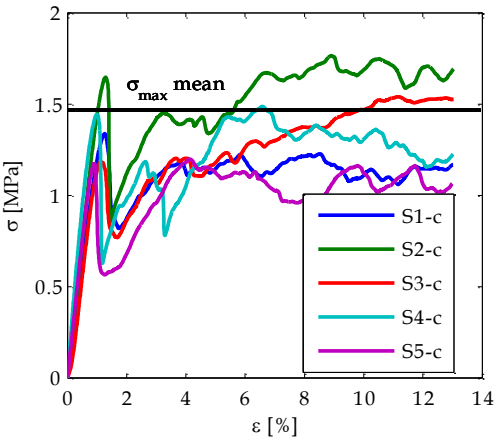

Figure 5.9 - Comparison between stress-strain curves of the compressed specimen

The results herein achieved in compression, in terms of maximum strength and elastic modulus are in accordance with previous results, as evidenced in Figure 5.10, both in terms of compressive strength and Young's modulus. Considering a linear trend both in case of density vs. compressive strength and density vs. Young's modulus in compression, the black point, from the present investigation, is consistent with the ones in Verdolotti et al. (2008) and (2012), namely the strength and the stiffness of the hybrid foam in compression quite linearly increase with the increase of foam density.

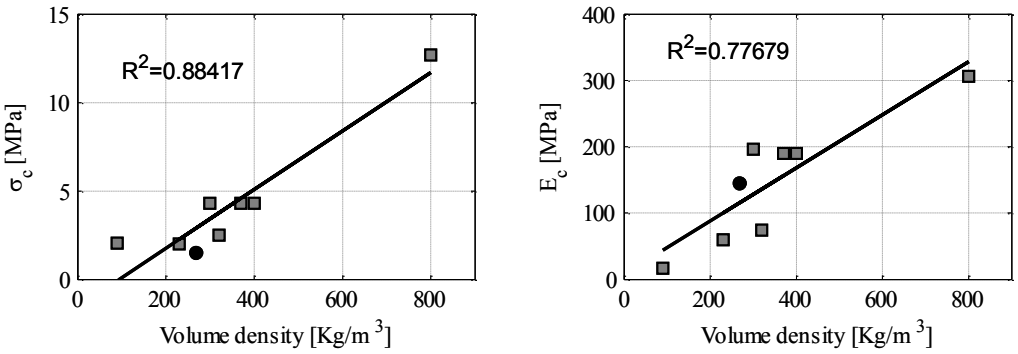

Figure 5.10 – Effect of hybrid foam density on (a) compressive strength and (b) compressive Young and fitting line with corresponding value of coefficient of determination (■ data from Verdolotti et al., 2008 and 2012; ● data from present work)

Usually, brittle materials as concrete, or cellular concrete, have no strength in tension, such as tensile test are not performed. Since the mechanical behavior of the hybrid foam is not completely known, due to the conjunct use of the polyurethane and the concrete phases, the tensile behavior is also analyzed. In Figure 5.11 the stress-strain curves point out an almost elastic-plastic behavior. Larger maximum strength (4.23±0.23 MPa) and elastic modulus (612.05±18.27 MPa) are recorded in tension, as evidenced in Table 5.7, than in compression. The presence of the polyurethane phase provides to the hybrid foam a good tensile strength and an appreciable ductility, with respect to a classic concrete, or cellular concrete.

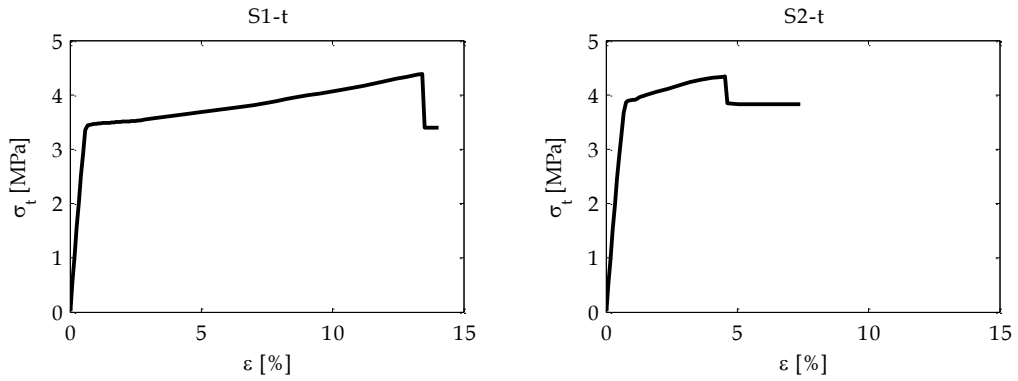

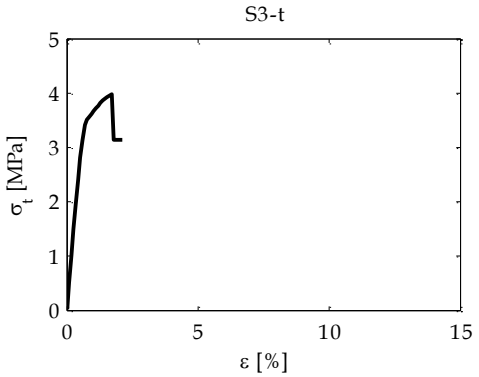

Figure 5.11 - Stress-strain curves for cubic specimen subject to tensile tests

Sample code	Tensile strenght	Elasticity modulus in tension
[-]	*[MPa]*	*[MPa]*
S1-t	4.39	632.58
S2-t	4.34	606.06
S3-t	3.98	597.24
Mean	**4.23**	**612.05**
Standard deviation	**0.23**	**18.27**

Table 5.7 – Tensile strength and elastic modulus for each specimen including mean value and standard deviation

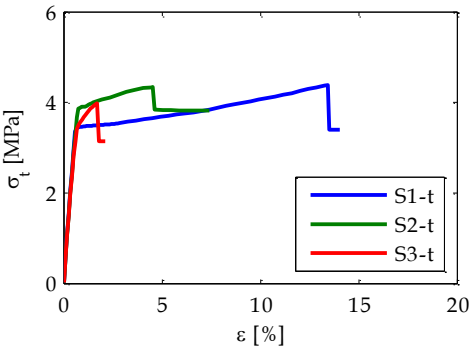

Figure 5.12 - Comparison between stress-strain curves of the tensile tests

In terms of shear behavior, the experimental force-displacement curves, shown in Figure 5.13, highlights a linear trend up to the maximum force, beyond which a brittle behavior is recognizable. The mean value of shear strength, i.e. 0.66±0.09 MPa, results in a lower resistant material if compared to compression and tension. Since it was not possible to glue the strain gauges over the specimens surface, in the v-notched portion where pure shear is recorded (see Figure 5.7), no information about the shear elastic modulus are provided by the experimental test.

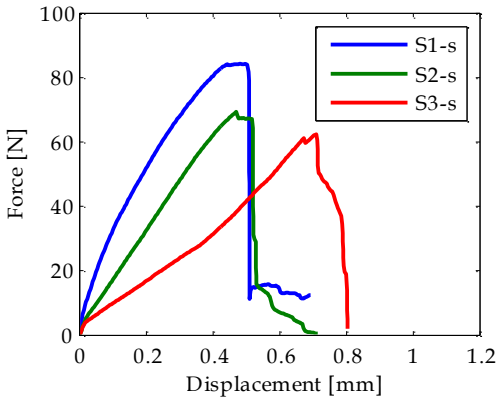

Figure 5.13 - Force vs displacement in for hybrid foam subject to shear test

Sample code	Shear strength
[-]	*[Mpa]*
S1-s	0.74
S2-s	0.67
S3-s	0.57
Mean	**0.66**
Standard deviation	**0.09**

Table 5.8 - Shear strength for each specimen including mean value and standard deviation

5.3 Hybrid foam vs. cellular concrete

The mechanical properties, in compression, tension and shear achieved by the presented tests allow making a comparison between the material here presented and other materials, nowadays widespread in the building market and generally used in the field of nonstructural components.

In Table 5.9 the comparison in term of mechanical and physical properties between the hybrid material and other two materials used for infills, i.e. brick (Poroton©) and cellular concrete (Ytong©), is made. The choice of this two materials for the comparison is not fortuitous, since the hybrid foam could be used in the same field, due to its good adhesion properties to the mortar (Verdolotti et al., 2012). This is caused by the high concentration of hydrated cement, distributed within the material and on the surface.

In comparison with Poroton and Ytong, the hybrid foam has a lower specific weight, which is a suitable aspect in seismic field due to the reduction of seismic mass and, consequently, of seismic inertial forces. The lowest Young's modulus in compression highlights a much deformable material, which could accommodate the deformation of the hosting structure during the earthquake.

The hybrid material shows a lower compression strength with respect to the classic brick and to the cellular concrete. However, as shown in Figure 5.10, a strength and stiffness increment could be obtained by increasing the density.

The recorded values of shear strength of the hybrid foam are quite similar to the ones of the brick and larger than the ones of the cellular concrete. This aspect is fascinating if an application for internal partition or external infill is thought for the hybrid material, due to the crucial role played by the shear strength.

With regard to the physical characteristics, the fire reaction Euroclass of the hybrid material (B2) highlight lower fire resistance features, due to the presence of the polyurethane phase, with respect the classic brick and the cellular concrete, which are classified as not combustible materials (A1).

The properties of sound insulation are quite comparable between the materials, even if the hybrid material has the lowest value. The rigid hybrid foam shows typically a microstructure characterized by both closed cell walls and by the presence of micro-cavity and, for this reason, it do not perform well in sound absorption with respect the open-celled foams, such as flexible polyurethane foam.

The hybrid foam shows very low values of thermal conductivity, lower than that of the traditional lightweight concrete commonly used as insulator (i.e., 0.12 W/m K). Generally, decrease of the insulating performances is observed with the increase of the density. This result is reasonable in view of the relative higher amount of conducting solid phase in higher density hybrids.

The water vapor permeability value (6E-11 kg/m s Pa), index of the material transpiration, is also consistent with the other ones. The introduction of the cement in the hybrid foam improve the permeability property of the material: as the amount of cement in the hybrid material increases, the water vapor transmission resistance decreases.

All the features herein presented highlight the potential use of the cement - polyurethane hybrid foam for protection of nonstructural components in seismic areas. Further study will allow identifying the applications in residential and industrial constructions.

Material	Volume density	Compressive strength	Compressive Young' modulus	Shear strength	Fire reaction (UNI EN 13501-1:2009)	Sound insulation (UNI ISO 140-1 and 717)	Thermal conductivity (l)	Water vapor permeability
	[kg/m^3]	*[MPa]*	*[MPa]*	*[MPa]*	*[Euroclass]*	*[dB]*	*[W/m K]*	*[kg/m s Pa]*
Brick (Poroton)	660	5	1600	0.20 ÷ 1.40	A1	45	0.13 ÷ 0.21	2E-13
Cellular concrete (Ytong)	575	2.81	2125	0.20 ÷ 0.30	A1	50	0.13	3.8E-08
Hybrid foam (Hypucem)	270	1.44	144	0.66	B2	34	0.036÷0.046	6E-11

Table 5.9 - Mechanical and physical properties comparison between classic brick (Poroton), cellular concrete (Ytong) and hybrid foam (Hypucem); data for Poroton and Ytong have been taken from Datasheet from producer

Chapter 6

SUMMARY AND FINAL REMARKS

During an earthquake, a direct risk for human life can be represented by the failure of internal partitions or external infills, the collapse of ceiling systems or suspended light fixtures, the overturn of heavy bookshelves or storage racks. Their failure can also cause the interruption of rescue operation in strategic structures, such as hospital and policy stations, exactly when their efficiency is essential, i.e. in the seismic event aftermath. The damage of the above-mentioned components, classified as nonstructural, may also result in a huge economic lost and downtime. These motivating factors justify the increasing interest in the knowledge of the seismic behavior of such nonstructural, or secondary system, and in improving their design in seismic areas.

The present thesis deals with innovative solutions for nonstructural components in seismic areas. A large part of the work, namely Chapter 2, Chapter 3 and Chapter 4, refer to in plane seismic behavior of plasterboard internal partitions, widely employed in commercial and industrial building of the European area. In the Chapter 5 an innovative material is presented for nonstructural applications in civil structures.

The in-plane behavior of plasterboard partition is firstly assessed by means of experimental tests. In the Chapter 2 the experimental campaign performed at the Laboratory of the Department of structures for engineering and architecture of the University of Naples Federico II, is presented. Quasi-static in-plane tests are carried out on ten high plasterboard partitions (height equal to 5 meters), representative of the most widespread typologies. The test setup and the specimens mounting procedure is detailed in the chapter, besides the loading test protocol and the setup

instrumentation. The experimental results are presented in terms of recorded damage related to inter-story drift achieved by the partition during the test. They point out that:

- all the partition show high initial stiffness but also an high ductile behaviour: even if they start exhibiting damage in correspondence of a low drift value, i.e. 0.2÷0.3%, they reach the collapse for inter-story drift larger than 2%;
- the inter-story drifts corresponding to the achievement of the damage limit state, or damage state 2, for all the partitions are much larger than 0.5%. It must be emphasized that this value (ϑ=0.5%) is usually used as reference value for damage limit state of buildings in seismic areas;
- the inter-story drifts related to the achievement of the damage state 3, corresponding to the life safety limit state, are very high for all the tested specimen (usually >2%), therefore larger than the limitation imposed by the Eurocode 8 (CEN, 2005) for buildings having non-structural elements fixed in a way so as not to interfere with structural deformations, i.e. drift ϑ= 1%.

In order to extend the in-plane seismic assessment of plasterboard partitions pursued by means of quasi-static tests, to different partition configurations, namely with larger widths and heights with respect the tested ones, an original modeling technique is proposed in Chapter 3. A 2-D plane model is defined in Sap2000 program, for four of the tested partitions. The elements composing the partitions, i.e. steel studs, plasterboard panel and surrounding frame, are modelled as elastic linear element. The mechanical features of the steel and the plasterboard are previously defined through experimental test. The nonlinearity is lumped in the panel-to-stud screwed connections, modelled as nonlinear link. A tri-linear force-displacement backbone curve is assigned to the screwed connections matching the experimental results of monotonic tests on such connections. The modelled partitions are subjected to nonlinear static analyses in large displacement. The analytical results evidence that:

- the stress values in the plasterboards both in tension and compression are lower than 1 MPa and, therefore, far from the plasterboard strength. This aspect justify the adoption of a linear elastic material for the boards;
- the bending moment diagram on studs reveals large demand crossing the horizontal joints between the plasterboards. Such an evidence can

justify the damage, experimentally pointed out in the steel stud over and under the horizontal joints;

The failure of the partition due to elastic global buckling is a-posteriori checked, based on the internal forces acting in the steel studs. The Direct Strength Method (DSM) is applied to assess the occurrence of different buckling failure modes, i.e. local, distortional and global failure modes, in the studs. This method allows considering the restraining effect given by both the presence of the plasterboards and the screwed connections through the presence of linear springs on the steel stud cross section. The method evidences, for all the modelled partitions, that the global instability failure mode occurs for inter-story drift ratio very close to that drifts for which the specimens start showing a global out-of-plane curvature. It can be therefore deduced that the model well catches the global buckling failure mode of the specimen. The inter-story drift which causes the local buckling in the steel stud is also well predicted. This conclusion is based on the comparison between the strain trends in the steel studs at different inter-story drift levels.

The validation of the proposed FEM modelling for plasterboard internal partitions, allows an extension of the procedure to several partition configurations. The development of a computer tool that interfaces the finite element structural program SAP2000 and the Matlab platform, has allowed to carry out a large amount of analyses in order to evaluate the influence of geometrical features on the collapse drift. Eleven plasterboard partition typologies are modelled, firstly by setting a constant width, namely equal to 5 meters, and varying the partition height from 5 meters up to a maximum value. Then, by keeping constant the maximum height, the partition width is gradually increase from 3 meter up to obtain a width-height ratio equal to two. For each partition, the analyses results show that:

- when the partition height increases, i.e. by varying the H/B ratio between 1 and 2, the collapse drift remains quite constant. For each of the analysed partition configuration a collapse drift equal to the mean value can be considered, by making an error at most equal to 20%;
- when the partition width increase, i.e. by varying the B/H ratio between 0.3 and 2, the collapse drift gradually decreases with a cubic trend. The collapse drift becomes quite constant for width-height ratio larger than 1.5.

The plasterboard internal partition typology, until now discussed, is largely employed in industrial and commercial buildings. In residential structures, several materials are nowadays available to replace the classic brick, in order to improve both the seismic performance and the energy saving needs. In Chapter 5 a new

hybrid material based on the conjunct use of polyurethane and cement is presented; it is considered an innovative material able to meet the requirements of lightness, high deformability and ductility, but also of thermal and acoustic features, usually required for internal partitions and external infills. The mechanical properties of the polyurethane-cement hybrid foam are investigated. Compressive, tensile and shear tests are conducted, according to ASTM standard methods for cellular plastic materials, in order to understand the potential use of such a material in the building field as nonstructural components. The experimental results show that:

- the compressive properties of the hybrid foam are consistent with previous compressive tests results, evidencing a compressive strength of 1.4 MPa and an elastic modulus of 144 MPa, for a 270 kg/m^3 volume density;
- the material behaves better in traction than in compression, having an tensile strength of about 4 MPa and a Young's modulus in tension of 600 MPa. Furthermore, a quite elastic-plastic behavior is recognizable from the stress-strain curve;
- a maximum shear strength of 0.6 MPa is evaluated.

These values, if compared to the corresponding properties of other two materials generally used for nonstructural component, i.e. classic brick widely employed for internal partitions and infill, and cellular concrete, which has nowadays a market expansion, evidence that the hybrid foam is a lightweight material with respect the brick and the cellular concrete. The mechanical properties values highlight a less resistant and stiff material in compression. The hybrid shear strength proves to be greater than the corresponding value for cellular concrete and very similar to the brick one.

The physical properties of hybrid foam, such as fire resistance, sound insulation, thermal conductivity and water vapor permeability, are finally compared to those of the other competitor material. The low thermal conductivity value, i.e. 0.036 W/m K shows good properties of thermal insulation, such as the low water vapor permeability value (6E-11 kg/msPa) characterizes a quite transpiring material.

These properties associated to good fire resistance and sound insulations characteristic make the hybrid foam suitable for application in building field, with particular reference to nonstructural components. The highlighted high deformability and ductility of the hybrid foam make the material fascinating for seismic protection of nonstructural components.

References

[1] Adany, S. and B. W. Schafer (2006). "Buckling mode decomposition of single-branched open cross-section members via finite strip method: Derivation." Thin-Walled Structures 44(5): 563-584.

[2] AISI-S100 (2007). North American Specification for the Design of Cold-Formed Steel Structural Member - American Iron and Steel Institute. Canada.

[3] Bertero, R. D. and V. V. Bertero (2002). "Performance-based seismic engineering: the need for a reliable conceptual comprehensive approach." Earthquake Engineering & Structural Dynamics 31(3): 627-652.

[4] Bo, L., Z. Hong and H. Guangsu (2007). "A novel impedance matching material derived from polymer micro-particles." Journal of Materials Science 42(1): 199-206.

[5] CEN (2005). Eurocode 8: design of structures for earthquake resistance - Part 1: general rules, seismic actions and rules for buildings. EN 1998-1, Brussels, Belgium.

[6] Coppola, O., E. Di Maio and G. Magliulo (2015). "Mechanical characterization of polyurethane-cement hybrid foams in compression, tension and shear." Construction and Building Materials (under review).

[7] CSI Computer & Structures Inc. (2004). SAP2000. Linear and Nonlinear Static and Dynamic Analysis of Three-Dimensional Structures, Computer & Structures, Inc. Berkeley, California.

[8] D1621-00, A. (2003). "Standard Test Method for Compressive Properties Of Rigid Cellular Plastics." Annual Book of ASTM Standard Volume 08.01 Plastics (I).

[9] D1623-03, A. (2003). "Standard Test Method for Tensile and Tensile Adhesion Properties of Rigid Cellular Plastics." Annual Book of ASTM Standard Volume 08.01 Plastics (I).

[10] D5379, A. (2012). "Standard Test Method for Shear Properties of Composite Materials by the V-Notched Beam Method." Annual Book of ASTM Standard Volume 15.03 Space Simulation; Aerospace and Aircraft; Composite Materials.

[11] Davies, R., R. Retamales, G. Mosqueda and A. Filiatrault (2011). Experimental Seismic Evaluation, Model Parameterization, and Effects of Cold-Formed Steel-Framed Gypsum Partition Walls on the Seismic Performance of an Essential

Facility. Technical Report MCEER-11-0005. University at Buffalo, State University of New York.

[12] Federal Emergency Management Agency (FEMA) (2007). Interim protocols for determining seismic performance characteristics of structural and nonstructural components through laboratory testing. Report No. FEMA 461. Washington DC, USA. .

[13] Fiorino, L., O. Iuorio and R. Landolfo (2009). "Sheathed cold-formed steel housing: A seismic design procedure." Thin-Walled Structures 47(8-9): 919-930.

[14] Folz, B. and A. Filiatrault (2004). "Seismic analysis of woodframe structures. I: Model formulation." Journal of Structural Engineering-Asce 130(9): 1353-1360.

[15] Fulop, L. A. and D. Dubina (2004). "Performance of wall-stud cold-formed shear panels under monotonic and cyclic loading Part II: Numerical modelling and performance analysis." Thin-Walled Structures 42(2): 339-349.

[16] Iannace, S., E. Di Maio, L. Verdolotti and M. Larvogna (2008). "A foamed polymer-inorganic binder hybrid material having controlled density e morphology, method for its preparation and uses thereof." World Intellectual Property Organization WO 2008/007187 A2.

[17] Ikuta, E. and M. Miyano (2011). Study of Damage to the Human Body Caused by Earthquakes: Development of a Mannequin for Thoracic Compression Experiments and Cyber Mannequin Using the Finite Element Method. Human Casualties in Earthquakes. R. Spence, E. So and C. Scawthorn, Springer Netherlands. 29: 275-289.

[18] Iosipescu, N. (1967). "New accurate procedure for single shear testing of metals." Journal of Materials 2(3): 537-566.

[19] Kanvinde, A. M. and G. G. Deierlein (2006). "Analytical models for the seismic performance of gypsum drywall partitions." Earthquake Spectra 22(2): 391-411.

[20] Magliulo, G., M. Ercolino, C. Petrone, O. Coppola and G. Manfredi (2014). "Emilia Earthquake: the Seismic Performance of Precast RC Buildings." Earthquake Spectra 30(2): 891-912.

[21] Magliulo, G., C. Petrone, V. Capozzi, G. Maddaloni, P. Lopez and G. Manfredi (2014). "Seismic performance evaluation of plasterboard partitions via shake table tests." Bulletin of Earthquake Engineering 12(4): 1657-1677.

[22] Magliulo, G., C. Petrone, V. Capozzi, G. Maddaloni, P. Lopez, R. Talamonti and G. Manfredi (2012). "Shake Table Tests on Infill Plasterboard Partitions." The Open Construction and Building Technology Journal 6((Suppl 1-M10)): 155-163.

[23] McKenna, F. and G. L. Fenves (2013). OpenSees Manual http://opensees.berkeley.edu, Pacific Earthquake Engineering Research Center, Berkeley, California.

[24] Petrone, C., G. Magliulo, P. Lopez and G. Manfredi (2014). "Seismic fragility evaluation of plasterboard partitions via in-plane quasi-static tests." Earthquake Engineering & Structural Dynamics (under review).

[25] Price, H. J., A. De Sortis and M. Schotanus (2012). "Performance of the San Salvatore Regional Hospital in the 2009 L'Aquila Earthquake." Earthquake Spectra 28(1): 239-256.

[26] Retamales, R., R. Davies, G. Mosqueda and A. Filiatrault (2013). "Experimental Seismic Fragility of Cold-Formed Steel Framed Gypsum Partition Walls." Journal of Structural Engineering 139(8): 1285-1293.

[27] Sarier, N. and E. Onder (2008). "Thermal insulation capability of PEG-containing polyurethane foams." Thermochimica Acta 475(1-2): 15-21.

[28] Schafer, B. W. (2012). "CUFSM 4.05 -Elastic Buckling Analysis of Thin-walled Members with general end boundary conditions."

[29] Schafer, B. W. (2013). Sheathing Braced Design of Wall Studs - Final report. Johns Hopkins University, Baltimore, MD, US.

[30] Schafer, B. W., L. C. M. Vieira, R. H. Sangree and Y. Guan (2009). "Rotational Restraint And Distortional Buckling In Cold-Formed Steel Framing Systems." Revista Sul-Americana de Engenharia Estrutural, Passo Fundo 7(1): 71-90.

[31] Taghavi, S. and E. Miranda (2003). Response assessment of nonstructural building elements, PEER report 2003/05. College of Engineering, University of California Berkeley, USA. .

[32] Tasligedik, A. S., S. Pampanin and A. Palermo (2015). "Low damage seismic solutions for non-structural drywall partitions." Bulletin of Earthquake Engineering 13: 1029-1050.

[33] Telue, Y. and M. Mahendran (2004). "Behaviour and design of cold-formed steel wall frames lined with plasterboard on both sides." Engineering Structures 26(5): 567-579.

[34] Verdolotti, L., E. Di Maio, G. Forte, M. Lavorgna and S. Iannace (2010). "Hydration-induced reinforcement of polyurethane-cement foams: solvent resistance and mechanical properties." Journal of Materials Science 45(12): 3388-3391.

[35] Verdolotti, L., E. Di Maio, M. Larvogna, S. Iannace and L. Nicolais (2008). "Polyurethane–Cement-Based Foams: Characterization and Potential Uses." Journal of Applied Polymer Science 107 1-8.

[36] Verdolotti, L., E. Di Maio, M. Lavorgna and S. Iannace (2012). "Hydration-induced reinforcement of rigid polyurethane-cement foams: mechanical and functional properties." Journal of Materials Science 47(19): 6948-6957.

[37] Verdolotti, L., M. Lavorgna, E. Di Maio and S. Iannace (2013). "Hydration-induced reinforcement of rigid polyurethane-cement foams: The effect of the co-continuous morphology on the thermal-oxidative stability." Polymer Degradation and Stability 98(1): 64-72.

[38] Vieira, L. C. M. and B. W. Schafer (2010). Behavior and Design of Axially Compressed Sheathed Wall Studs Twentieth International Specialty Conference on Cold-Formed Steel Structures Saint Louis, Missouri, USA,.

[39] Vieira, L. C. M. and B. W. Schafer (2012). "Lateral stiffness and strength of sheathing braced cold-formed steel stud walls." Engineering Structures 37: 205-213.

[40] Vieira, L. C. M. and B. W. Schafer (2013). "Behavior and Design of Sheathed Cold-Formed Steel Stud Walls under Compression." Journal of Structural Engineering-Asce 139(5): 772-786.

[41] Villaverde, R. (1997). "Seismic design of secondary structures: State of the art." Journal of Structural Engineering-Asce 123(8): 1011-1019.

[42] Walrath, D. E. and D. F. Adams (1983). "The Iosipescu Shear Test as Applied to Composite Materials." Experimental Mechanics 23(I): 105-110.

[43] Wood, R. L. and T. Hutchinson (2012). A numerical model for capturing the in-plane seismic response of interior metal stud partition walls. Technical report MCEER-12-0007. University of California, San Diego.

[44] Yang, Z. G., B. Zhao, S. L. Qin, Z. F. Hu, Z. K. Jin and J. H. Wang (2004). "Study on the mechanical properties of hybrid reinforced rigid polyurethane composite foam." Journal of Applied Polymer Science 92(3): 1493-1500.

Appendix

The appendix includes, for each tested partition:

- fem numerical model of the testes partition, including stud number, in SAP2000;
- bending moment diagrams on steel studs;
- compressive and tensile stress trend on plasterboard panels.

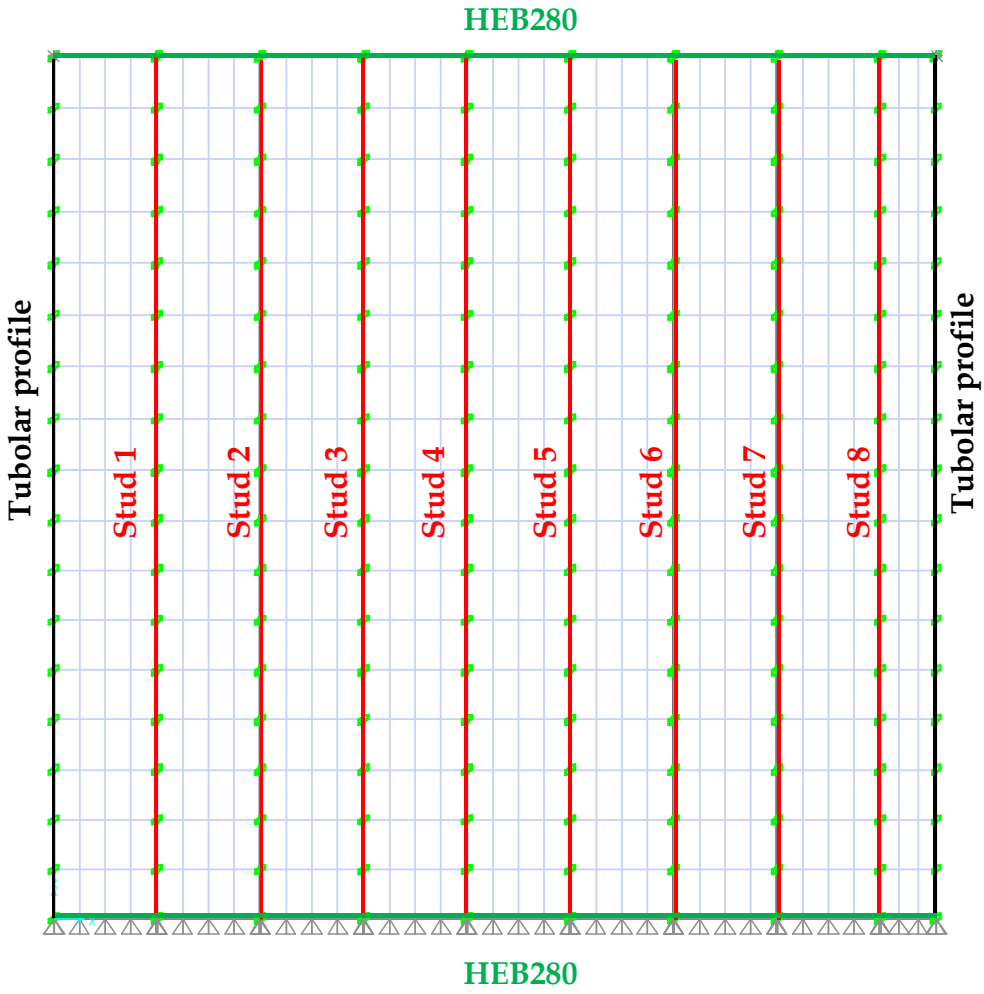

Figure A. 1 - Fem model in Sap2000 of the partition P-1

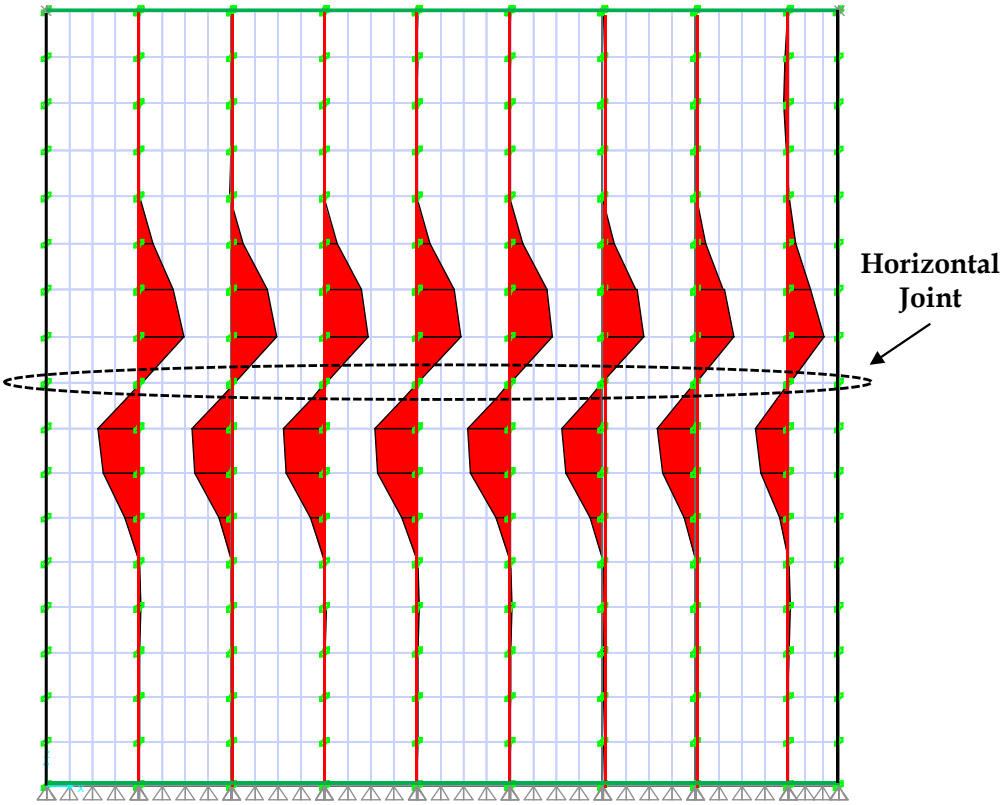

Figure A. 2 – Bending moment diagrams on studs of the partition P-1

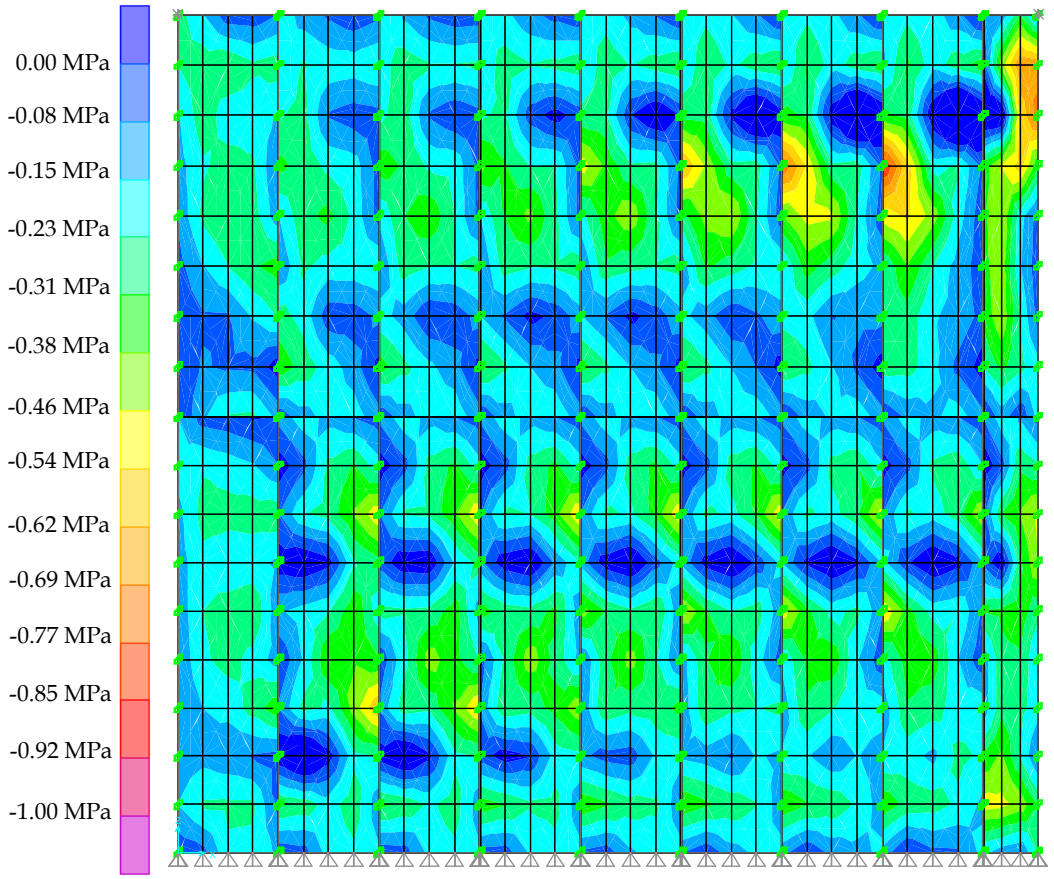

Figure A. 3 - Compressive stress trend in plasterboard panel of partition P-1

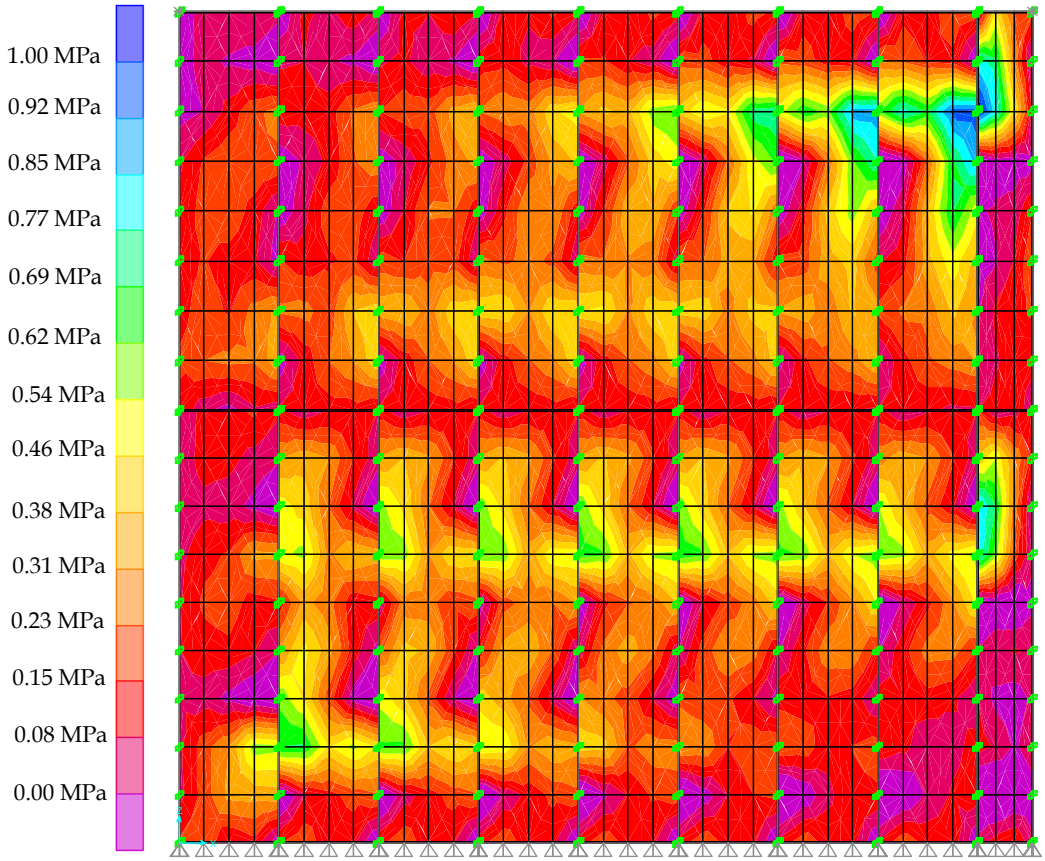

Figure A. 4 - Tensile stress trend in plasterboard panel of partition P-1

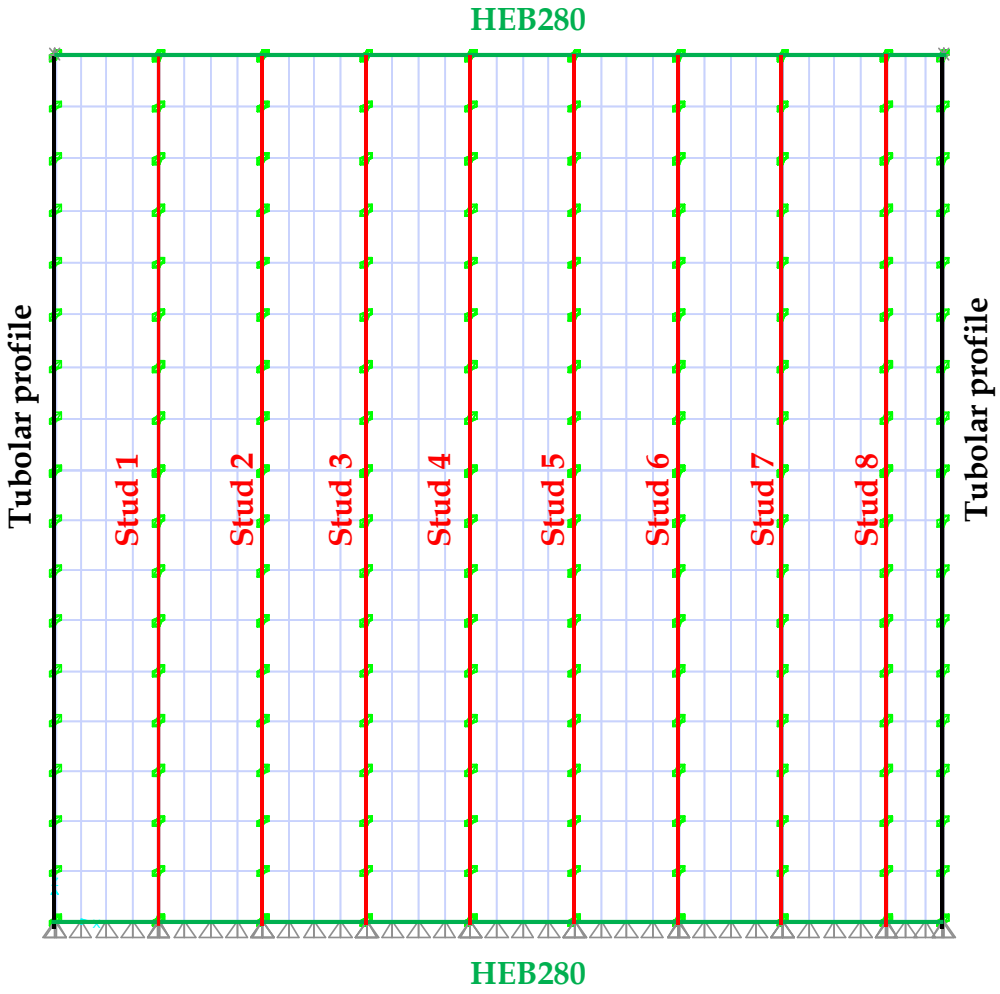

Figure A. 5 - Fem model in Sap2000 of the partition P-2

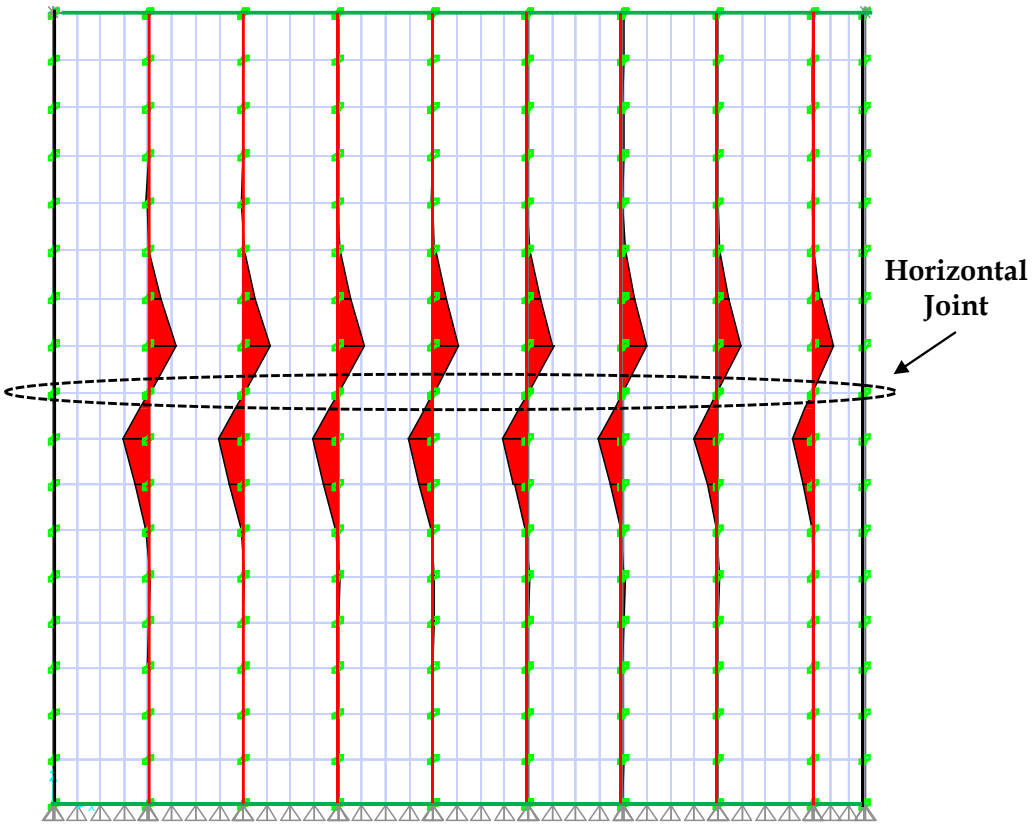

Figure A. 6 - Bending moment diagrams on studs of the partition P-2

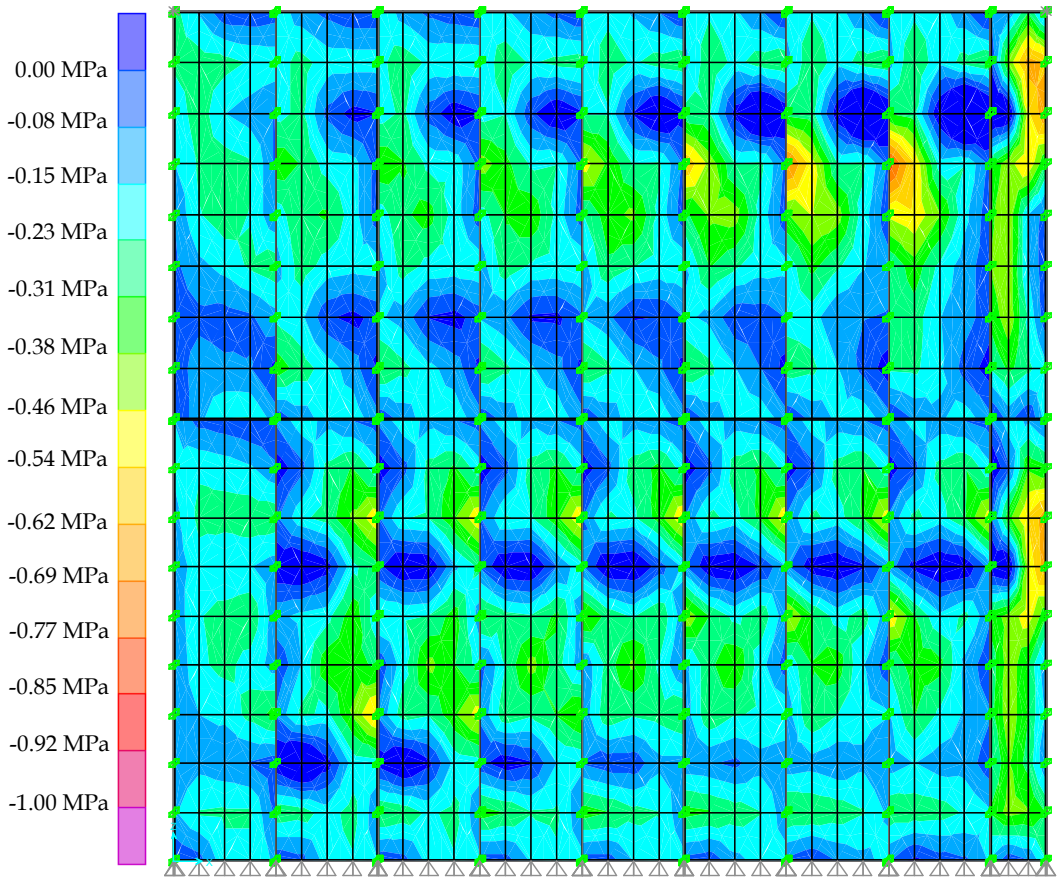

Figure A. 7 - Compressive stress trend in plasterboard panel of partition P-2

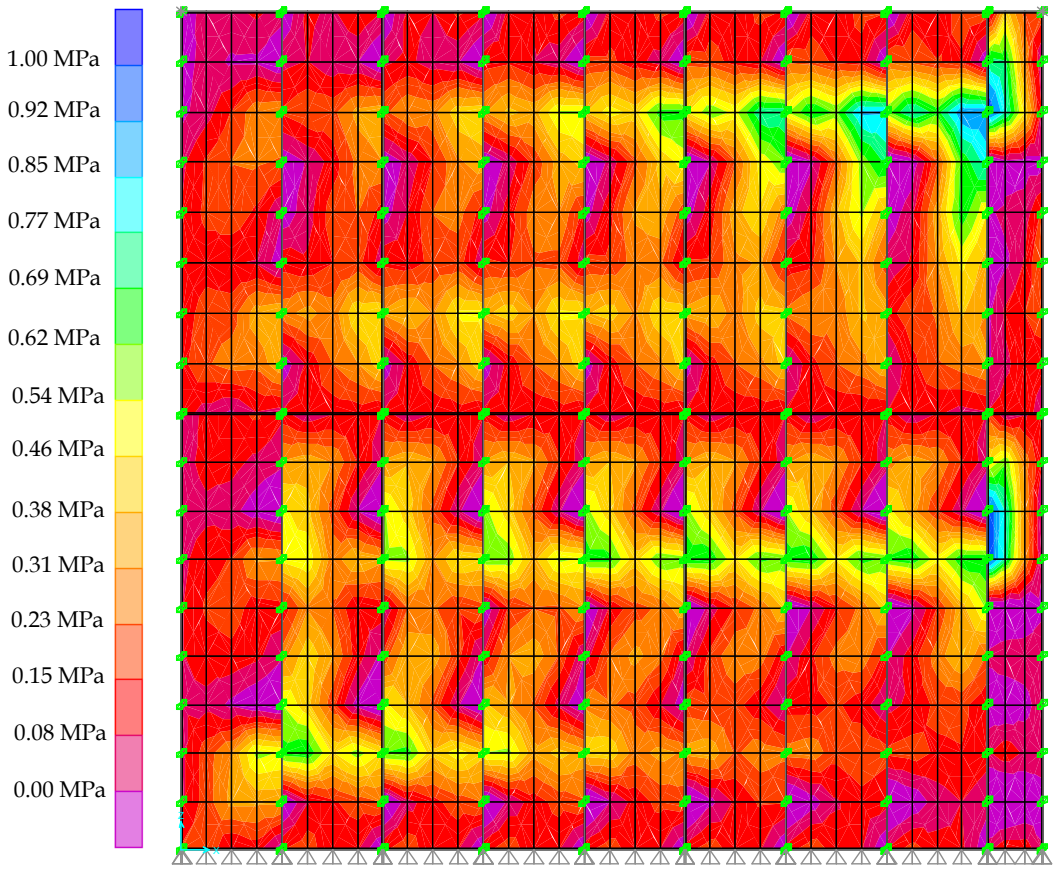

Figure A. 8 - Tensile stress trend in plasterboard panel of partition P-2

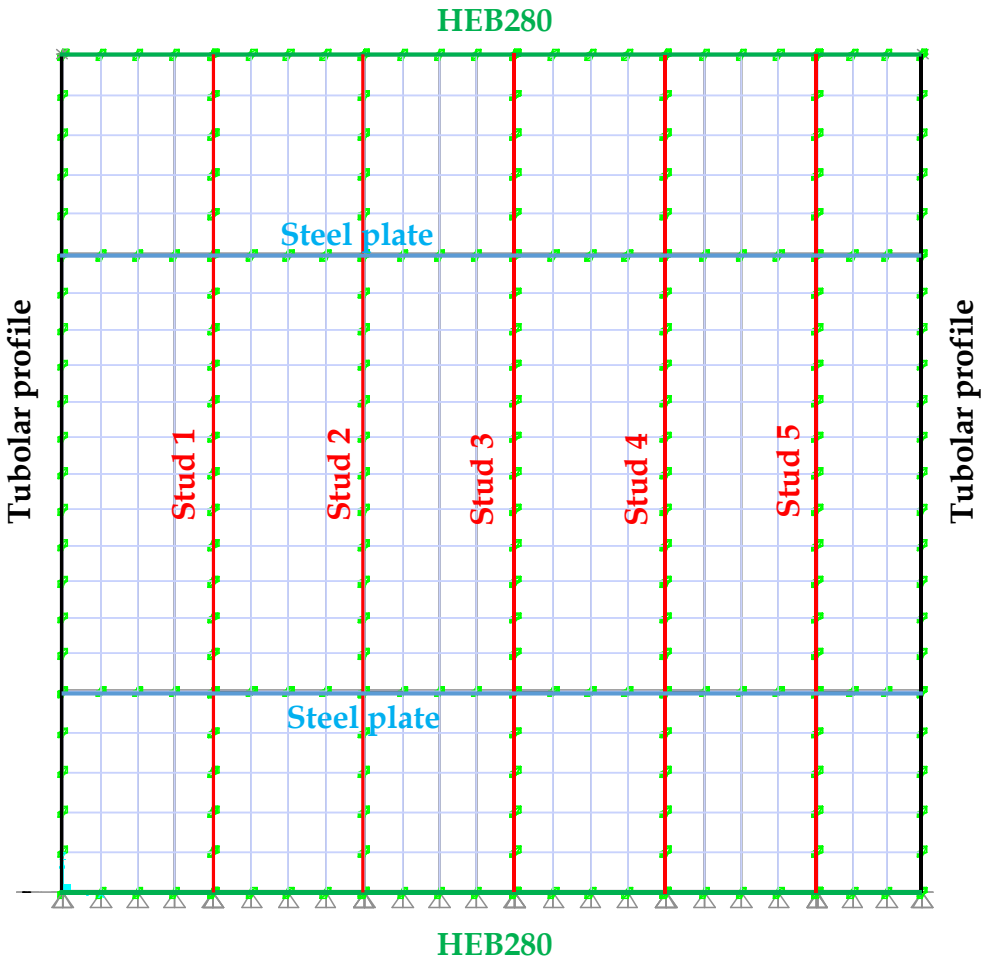

Figure A. 9 - Fem model in Sap2000 of the partition P-3

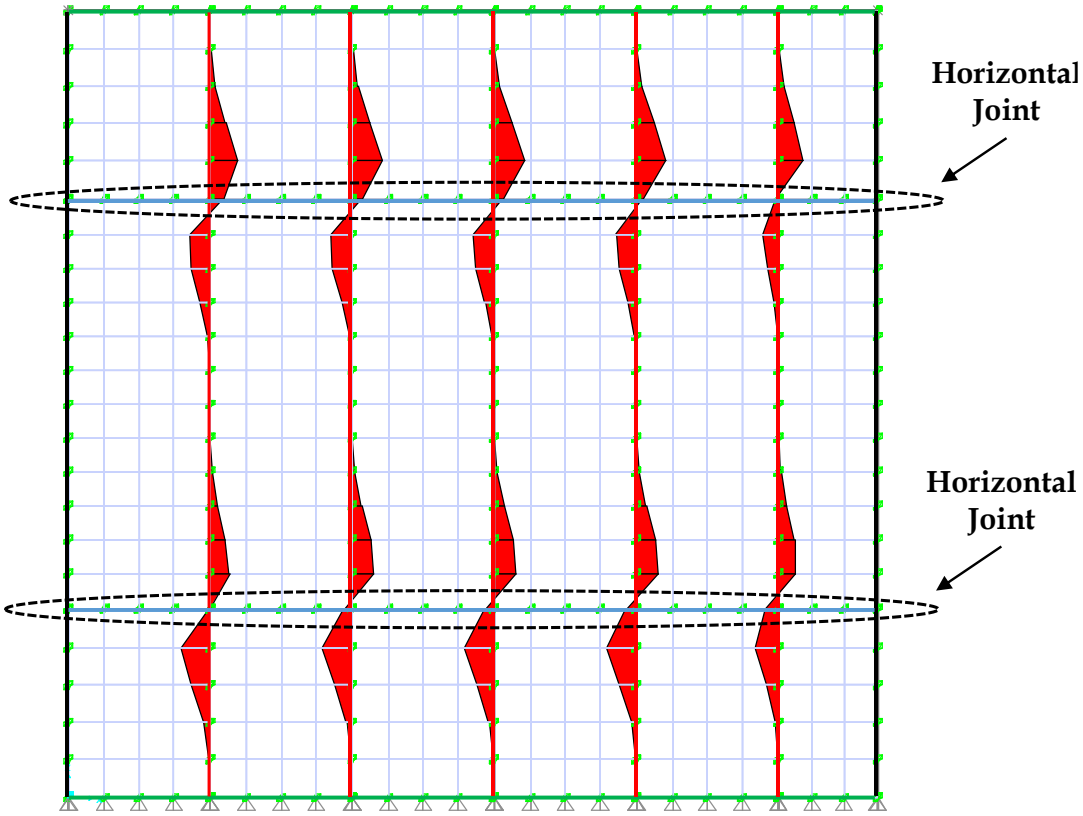

Figure A. 10 - Bending moment diagrams on studs of the partition P-3

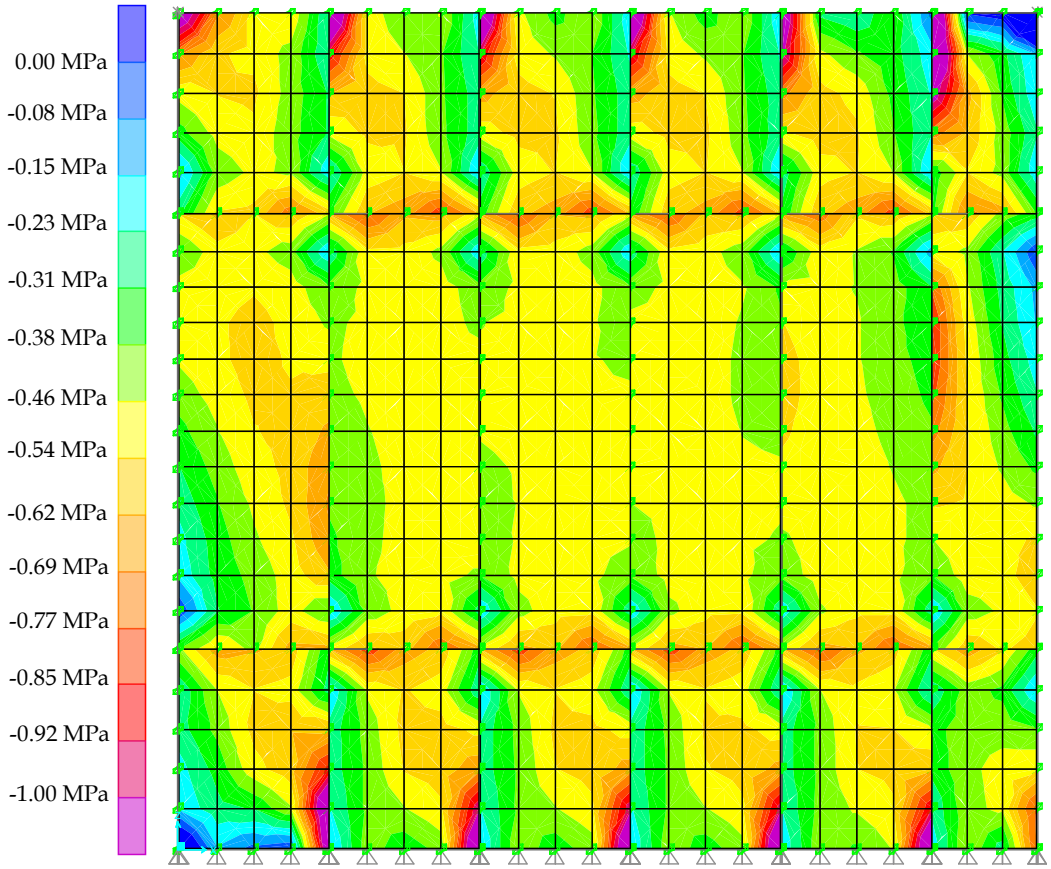

Figure A. 11 - Compressive stress trend in plasterboard panel of partition P-3

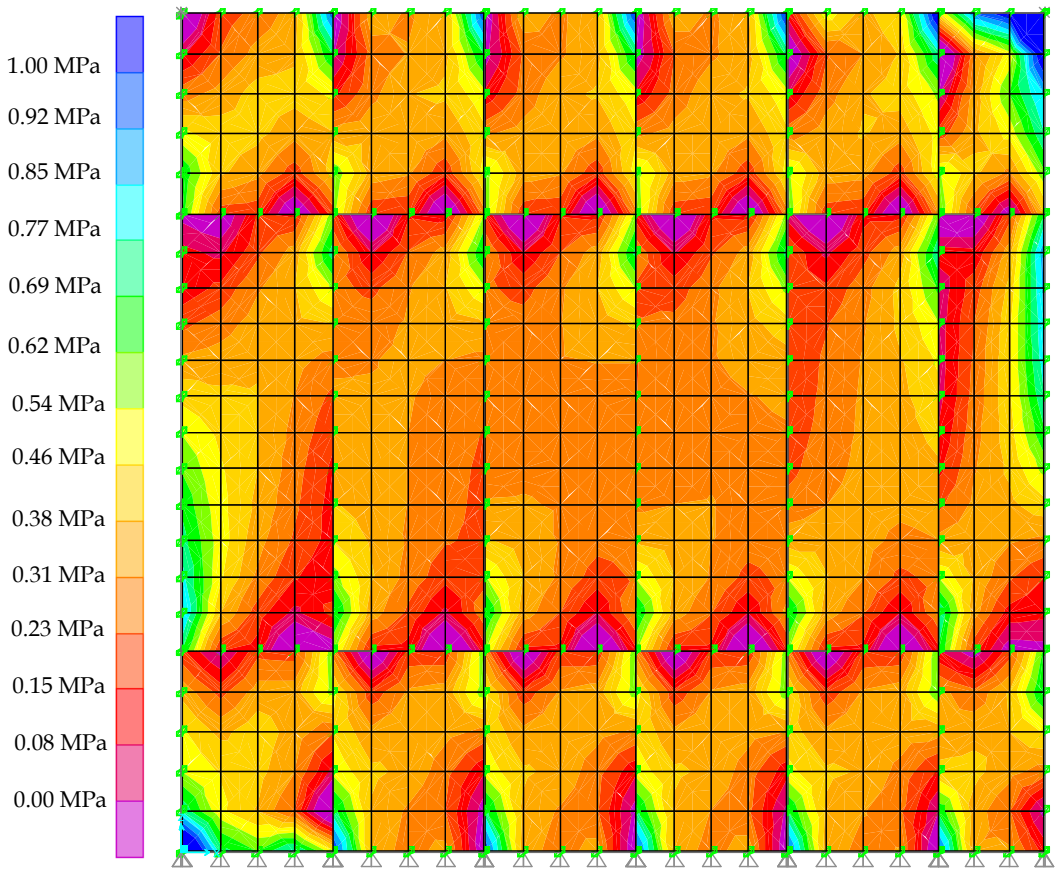

Figure A. 12 - Tensile stress trend in plasterboard panel of partition P-3

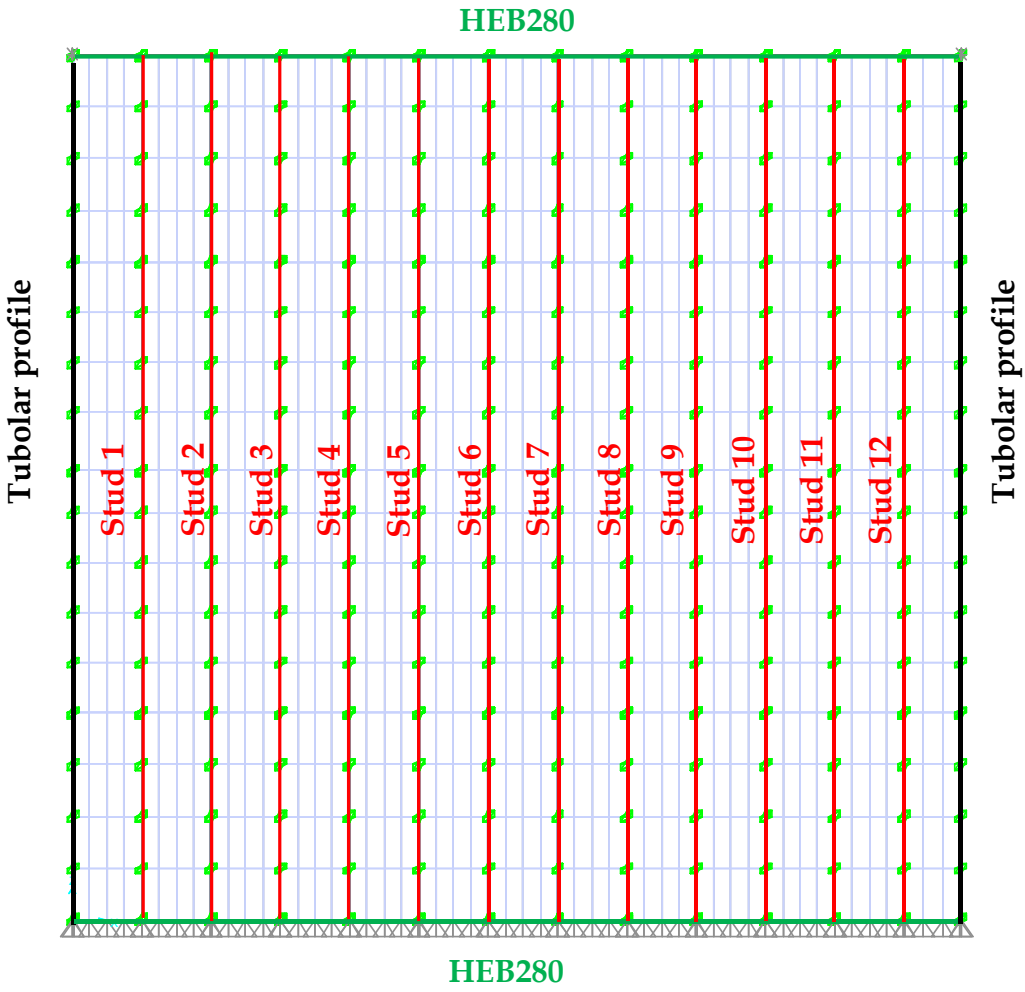

Figure A. 13 - Fem model in Sap2000 of the partition P-4

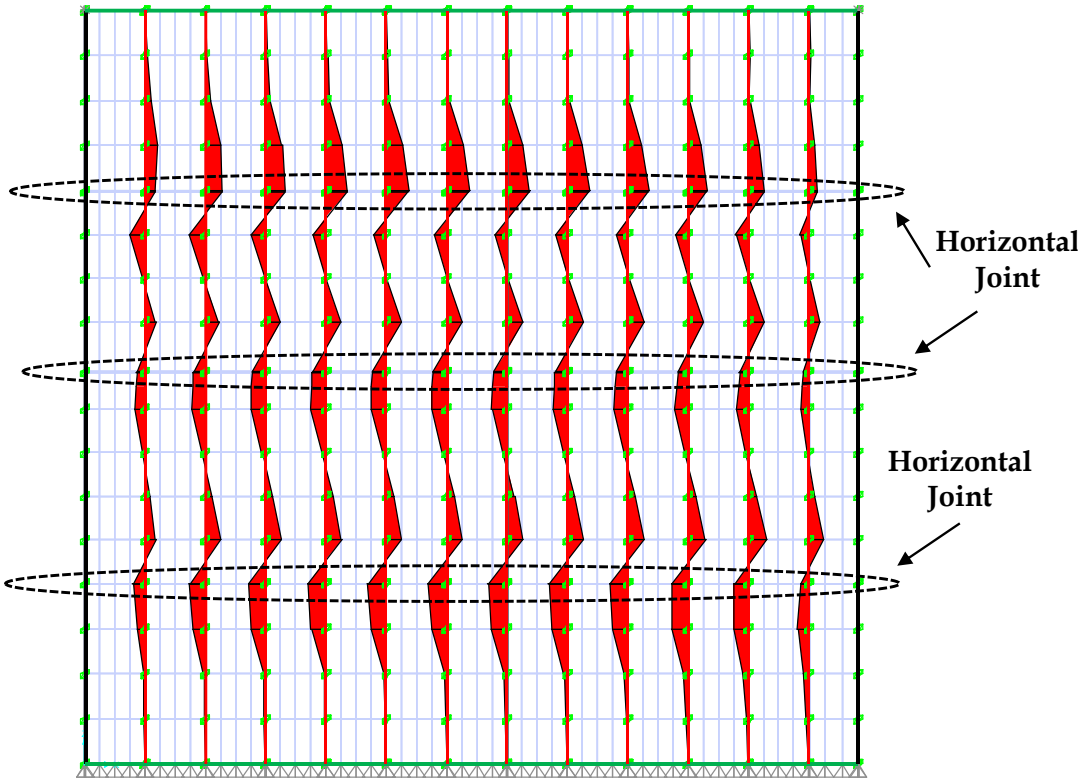

Figure A. 14 - Bending moment diagrams on studs of the partition P-4

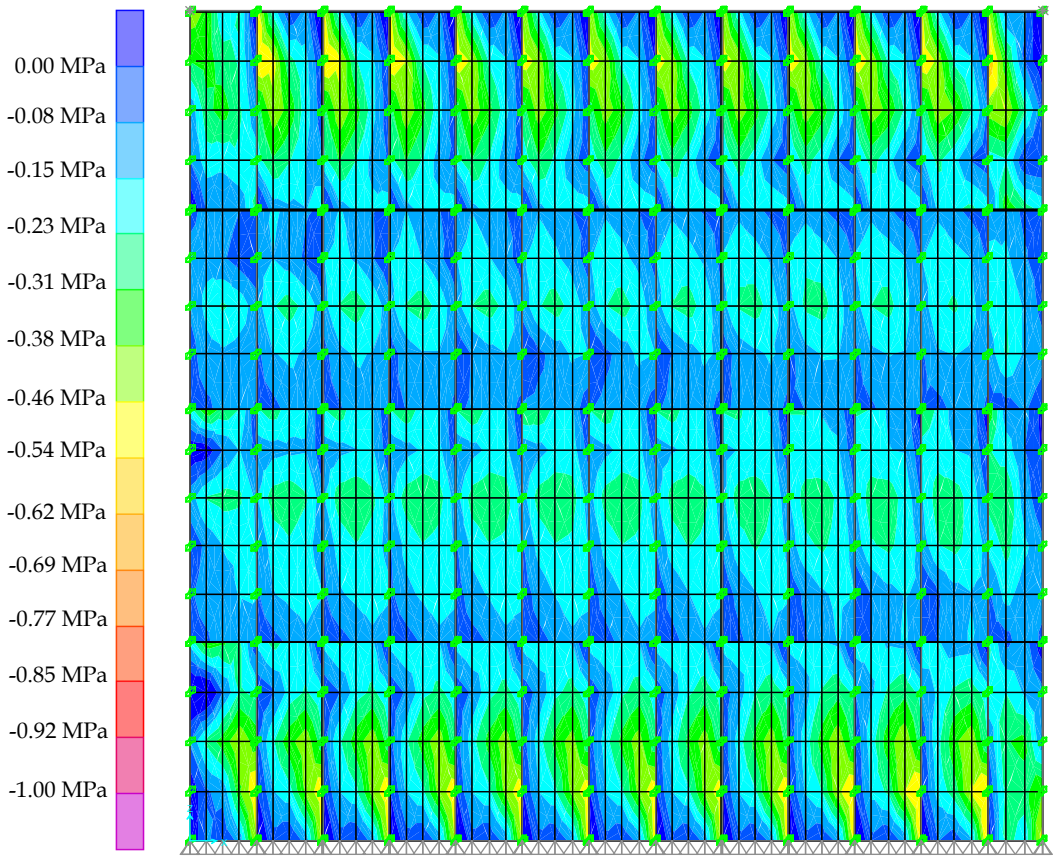

Figure A. 15 - Compressive stress trend in plasterboard panel of partition P-4

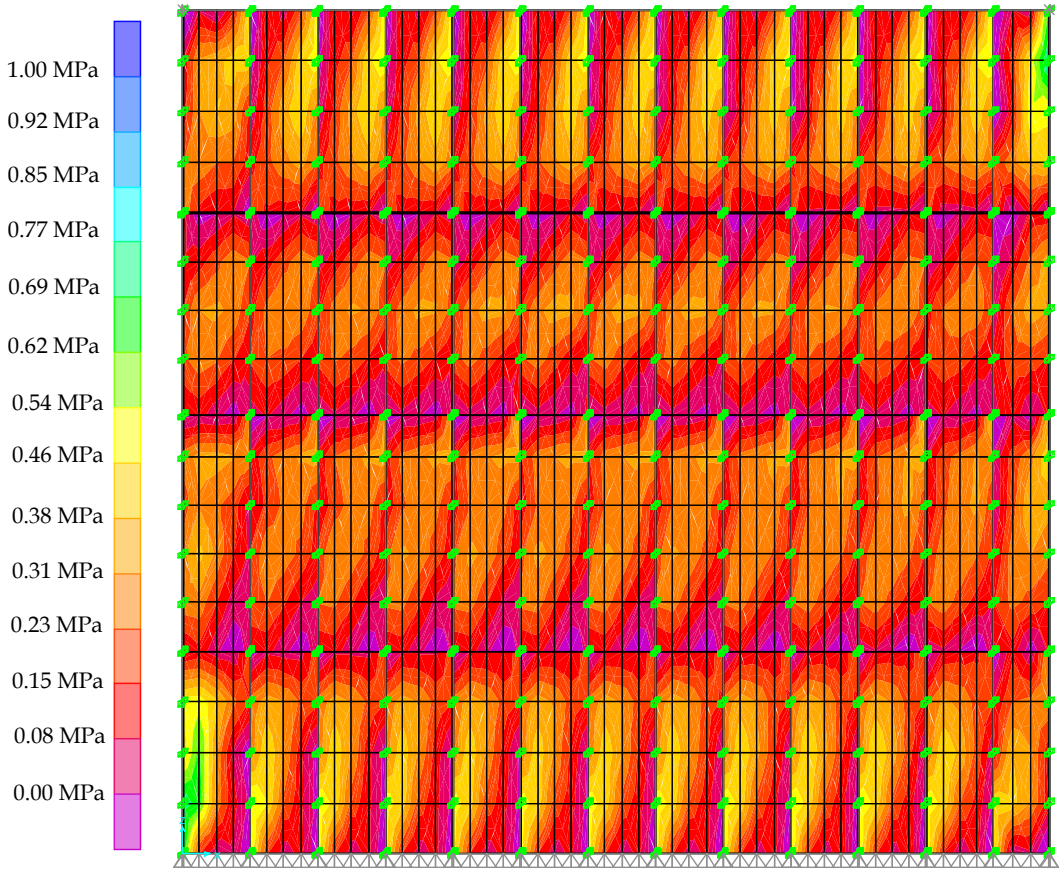

Figure A. 16 - Tensile stress trend in plasterboard panel of partition P-4